Predictive Dynamic Simulation of Human Movement Following Hip and Knee Replacement

by

Behzad Danaei

A thesis
presented to the University of Waterloo
in fulfillment of the
thesis requirement for the degree of
Doctor of Philosophy
in
Systems Design Engineering

Waterloo, Ontario, Canada, 2023

Examining Committee Membership

The following served on the Examining Committee for this thesis. The decision of the Examining Committee is by majority vote.

External Examiner:	Paulo Flores, Professor Dept. of Mechanical Engineering, University of Minho
Supervisor:	John McPhee, Professor Dept. of Systems Design Engineering, University of Waterloo
Internal Member:	Nasser Lashgarian Azad, Associate Professor Dept. of Systems Design Engineering, University of Waterloo
Internal Member:	Katja Mombaur, Professor Dept. of Systems Design Engineering, University of Waterloo
Internal-External Member:	Stacey Acker, Associate Professor Dept. of Kinesiology and Health Sciences University of Waterloo

Author's Declaration

I hereby declare that I am the sole author of this thesis. This is a true copy of the thesis, including any required final revisions, as accepted by my examiners.

I understand that my thesis may be made electronically available to the public.

Abstract

Total joint arthroplasty is a surgical intervention that involves the removal of arthritic or damaged components of a joint and their replacement with an artificial joint. The ultimate goal is to restore the joint's functionality to that of a healthy joint. The most commonly performed types of total joint arthroplasty are Total Hip Arthroplasty (THA) and Total Knee Arthroplasty (TKA). Despite technological advancements in these surgeries, there are several post-operative complications associated with improper positioning of the implants. In Canada, approximately 8.5% of the 50,000 THA cases and 6.8% of the 60,000 TKA cases require revision surgeries. These issues are partially attributed to the limited consideration of patient-specific characteristics in the pre-operative planning of THA and TKA. The relationship between the anatomical features unique to each patient and the optimal positioning of the implants is not yet fully understood. This problem underscores the need to develop engineering technologies that can prevent revision surgeries and enhance the quality of life for patients undergoing THA and TKA.

The objective of this research is to utilize subject-specific musculoskeletal models and predictive simulations to achieve optimal implant positioning, thereby reducing the risk of implant failure or patient dissatisfaction following THA and TKA. In this thesis, we define mathematical indices that encompass the key factors contributing to implant failure or patient dissatisfaction (such as impingement and edge-loading) and use them to quantify the effectiveness of a given implant positioning. Through predictive musculoskeletal simulations of common daily activities like sit-to-stand, we examine how patient-specific conditions influence the optimal placement of hip and knee implants for THA and TKA.

To the best of the author's knowledge, this research represents the first study to employ optimal control-based fully-predictive simulations in order to conduct "what-if" analyses and investigate the impact of patient-specific characteristics on the optimal positioning of implants. The methods and techniques employed in this study can also be applied to explore the effects of various other pathological disorders, not covered in this particular study, on the optimal implant positioning.

Acknowledgements

I express immense gratitude to Prof. John Mcphee, my supervisor, for his remarkable patience, generosity, and invaluable guidance throughout my PhD journey. He consistently demonstrated unwavering support by providing necessary resources and expert advice promptly and willingly. His extensive knowledge and expertise played a crucial role in helping me overcome intricate challenges, and I sincerely appreciate his insightful suggestions. I couldn't have asked for a better advisor for my research. I am continually amazed by his patience, as he never displayed any signs of frustration, even when my performance fell short. I feel immense pride in being his student and am grateful for the opportunity to have worked under his mentorship.

Additionally, I owe a debt of gratitude to my parents for their unwavering love and support throughout my life and academic pursuits. Their constant encouragement and belief in my abilities have been the driving force behind my success. They have always prioritized my education, ensuring that I have all the necessary resources and opportunities to reach my full potential.

Furthermore, I am appreciative of my friends and colleagues at the Motion Research Group (the MoRG). Their collective wisdom and camaraderie have been a great source of support.

Lastly, I would like to extend my utmost gratitude to Parya Khoshroo for her friendship, support, and encouragement. Without her, I would not have achieved the accomplishments I have throughout my PhD studies.

Dedication

To my beloved uncle and aunt, Majid and Homa, whose love and support have been constant companions in my life.

Table of Contents

List of Figures

List of Tables

Chapter 1

Introduction

1.1 Total Hip Arthroplasty (THA)

Total Hip Arthroplasty (THA) is a surgical procedure that involves replacing the damaged surfaces of a hip joint with artificial implants (refer to Fig. 1.1). The structure of the human hip resembles a ball-and-socket joint, where the femur's head acts as the ball and the pelvic bone's spherical cavity acts as the socket. During THA, the femur's head and neck are removed and substituted with an artificial component known as the femoral component. Similarly, the damaged socket portion of the pelvis is replaced by attaching an artificial socket, referred to as the acetabular component or "cup". The estimated prevalence of THA is 87 cases per 100,000 individuals globally, and this figure is expected to increase by 40% by the year 2030 [1].

In Canada, between 2014 and 2015, over 50,000 hip replacement surgeries took place, and approximately 8.5% of these cases required additional revision surgeries due to various issues such as complete dislocations (failure), disparities in leg length, and implant loosening [3]. Among the complaints following Total Hip Arthroplasty (THA), hip dislocation is recognized as the most significant cause [4]. Hip dislocation occurs when the femur's head is displaced from the cup.

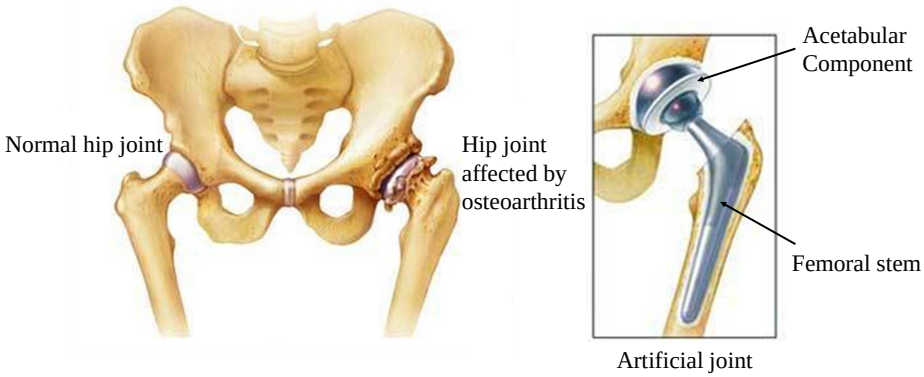

Figure 1.1: Total hip arthroplasty (The figure is adapted from Mayo Foundation For Medical Education And Research [2]).

Two primary factors contribute to hip dislocation [5]: firstly, if the contact force within the hip joint shifts beyond the cup surface, the cup loses its ability to keep the head securely in place, a condition known as edge-loading. Secondly, when there is contact between the femoral neck and the cup, called impingement, it can cause the femur to lever out of the cup. Currently, there is a lack of mechanistic models in the literature that explain the relationship between implant positioning, design parameters, individual-specific information, and edge-loading or impingement during the dynamic movements of daily activities.

Proper orientation of the cup is reported as the most significant factor to reduce the risk of dislocation [4]. The widely adopted guideline for the cup orientation is the *Lewinnek safe zone* [6]. However, this kinematic metric has been shown to have minimal effect on reducing the risk of dislocation [7, 8], which depends on subject-specific factors such as pelvic tilt and spine flexibility.

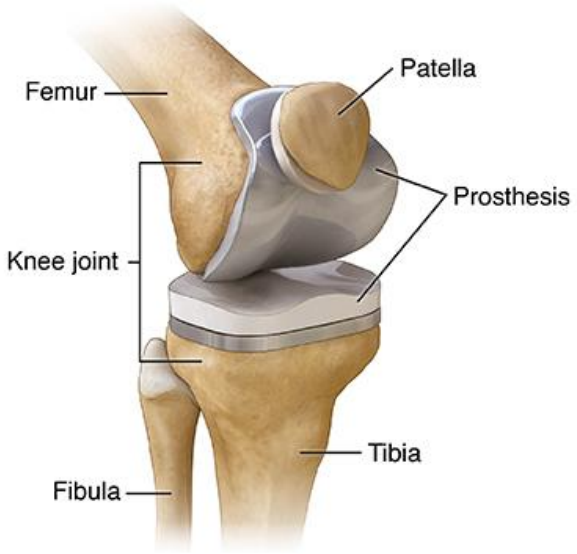

Figure 1.2: Total knee arthroplasty [9].

1.2 Total Knee Arthroplasty (TKA)

Total Knee Arthroplasty (also known as total knee replacement) is a surgical procedure in which the articulating surfaces of a damaged knee joint (e.g. due to severe osteoarthritis) are replaced with artificial implants (see Fig. 1.2). The human knee can be considered as a complex mechanical system, where the tibia has both translational and rotational motion on the distal end of the femur. In TKA, the joining ends of tibia and femur are removed and are replaced with artificial parts. Between 2014-2015 in Canada, there were over 60,000 knee replacement surgeries, which shows a 20% increase compared to 5 years before [3].

Approximately 20% of patients report dissatisfaction following primary TKA [10], and 6.8% required revision surgeries [3]. However, in the literature, it is still unclear which factors contribute the most to patient dissatisfaction [10]. Based on a study by Gunaratne et al [10], "patient expectations, higher function before surgery, stage of arthritic disease, complications, poor resolution of pain, and lower improvement in knee function" are the

main reasons of dissatisfaction. Among Canadian patients, the most common reasons for dissatisfaction were aseptic loosening of the implants (28.7%), infection (23.4%) and knee instability (15.9%) [3]. Even with advances in knee implant technologies, the rate of dissatisfaction (about 1 in 5) has remained the same over the past decades. The reason is that the mechanics of the knee following TKA is not fully understood [11].

1.3 Research Aims and Objectives

To address the surgical failures mentioned above, which result in the need for revisions or patient dissatisfaction, it is essential to explore new engineering technologies that can mitigate complications following THA and TKA, thereby reducing the need for revision surgeries and enhancing patients' quality of life.

The objective of this research is to devise novel techniques for determining the optimal position and orientation of THA and TKA implants. By employing subject-specific musculoskeletal models and dynamic simulations, this research will examine various movements such as sit-to-stand, aiming to ascertain the optimal implant configuration that minimizes the risk of dislocation or patient dissatisfaction following THA and TKA procedures.

The first critical step towards determining the optimal position of implants is to identify and quantify the key factors that significantly influence the outcomes of THA and TKA surgeries. Consequently, part of this research will focus on achieving this primary objective as it plays a pivotal role in the overall study. Moreover, to comprehensively analyze the impact of diverse patient-specific conditions on THA and TKA outcomes, the integration of predictive simulations becomes imperative. Therefore, an equally essential goal of this research is to develop predictive simulations that account for various patient conditions.

The outcomes of this study will contribute to enhanced patient satisfaction and reduced post-surgical complications, leading to cost savings in healthcare systems both within Canada and internationally.

1.4 Original Contributions

The main contributions of this research can be summarized as follows:

Chapter 3

- Quantifying the mathematical assessment of implant impingement and edge-loading simultaneously to evaluate the risk of dislocation.
- Eliminating the need for force plate measurement for double-stance inverse dynamic analysis by estimating ground reaction forces.
- Introducing different criteria for optimizing cup alignment to consider both impingement and edge-loading.
- Achieving optimal cup alignment through a full body musculoskeletal model based on subject-specific motion capture data.
- Investigating the impact of pelvic tilt on the optimal alignment of the acetabular cup.

Chapter 4

- Utilizing fully predictive simulations for the first time to synthesize sit-to-stand and stooping down movements for various patient conditions and assessing their effects on optimal cup alignment.
- Discovering new insights into the relationships between patient conditions, such as hip and knee joint pain, and the risk of hip dislocation, which were previously unreported.
- Demonstrating the potential of the proposed method to investigate additional patient conditions, including muscle impairment and other pathological conditions not covered in this thesis.

Chapter 5

- Developing a 12 Degree-of-Freedom volumetric contact-based model of the knee implant, including the patella, capable of predicting kinematics of the knee joint under different muscle forces and loads and comparing the model results to experimental measurements.

- Introducing a Single Degree-of-Freedom Equivalent Kinematic (SEK) model of the knee implant to reduce computational time in full musculoskeletal simulations. Unlike conventional knee models that rely on ideal revolute joints, this model incorporates secondary kinematics without adding computational burden.

- Identifying and quantifying three dimensionless indices as factors influencing the outcome of TKA: 1) balancing medial and lateral load distributions, 2) ligament balancing, and 3) varus/valgus alignment. These indices aid in optimal implant positioning.

- Assessing the sensitivity of these indices to changes in implant positioning, providing insights into the effects of different positioning changes on ligament laxity, medial and lateral load distribution, and varus/valgus angle throughout the knee joint's range of motion.

- Proposing an optimization framework for optimal knee implant placement based on full musculoskeletal simulations, considering the three aforementioned indices.

1.5 Structure of the Thesis

In Chapter 2, we delve into the literature review, focusing on simulating musculoskeletal systems, particularly the sit-to-stand motion. We also examine recent studies on hip and knee joint modeling and optimizing implant positioning after THA and TKA. The chapter

concludes by addressing the existing gaps in predictive simulations and optimal implant placement.

Chapter 3 presents a method based on inverse dynamics for achieving optimal alignment of the acetabular cup. This approach utilizes motion capture data obtained from a subject and introduces two indices, Angular Impingement and Edge-loading Distance (AID and AED respectively), to quantify the distance from implant impingement and edge-loading. The impact of pelvic tilt on cup alignment is also explored.

Chapter 4 aims to overcome the limitations of the method proposed in Chapter 3, which relies on experimental motion capture data. Predictive simulations are employed to synthesize sit-to-stand and stooping down movements under various patient conditions, enabling investigation of how these conditions affect optimal cup alignment.

In Chapter 5, we introduce two knee implant models. The first model is a comprehensive 12-degree-of-freedom (DoF) representation that incorporates the volumetric contact between femoral and tibial implants, as well as the patellofemoral contact. The second model employs a Single-DoF Equivalent Kinematic (SEK) approach for the knee joint. A co-simulations framework is proposed to leverage both knee models in our simulation. The knee model is calibrated and validated using patient-specific data, such as secondary knee kinematics and ground reaction forces. Additionally, three quantitative indices are introduced to evaluate the optimality of implant positioning based on three criteria: balancing medial and lateral load distributions, ligament balancing, and varus/valgus alignment. The sensitivity of these indices to changes in implant positioning is assessed, and the knee implant placement is optimized by minimizing the deviation of the indices from their desired values during predicted sit-to-stand motion.

Chapter 6 serves as the final chapter of the thesis, summarizing and discussing the main findings, conclusions, and research limitations. Furthermore, it presents ideas for enhancing musculoskeletal modeling and predictive simulations to achieve optimal implant placement following THA and TKA in future studies.

Chapter 2

Literature Review

The way humans move is a result of complex interactions between muscles, ligaments, and bones, as well as the environment around them. However, measuring the forces of muscle, ligament, and joint contact within the body is challenging without invasive procedures. However, through research conducted on individuals using instrumented prostheses, it has become feasible to acquire real-time measurements of internal joint loads, leading to the creation of databases containing recorded in vivo joint forces. The OrthoLoad project [12] and the Grand Challenge Competition to Predict in Vivo Knee Loads [13] are examples of initiatives that have provided valuable experimental material to the biomechanics community, helping them improve their models through validation.

Although these datasets offer valuable insights, they cannot be directly utilized to forecast surgical outcomes for new patients. Consequently, there is a growing interest in developing computational models capable of predicting dynamic and objective information specific to individual patients. These models aim to assist in generating quantitative and personalized recommendations for optimal treatment, potentially overcoming the limitations of current practices that rely on subjective, static, and qualitative assessments [14–16].

The first part of this chapter will cover the typical techniques utilized to model and simulate musculoskeletal systems, with a particular emphasis on sit-to-stand and lifting

movements. Following that, we will examine previous research on modeling the hip and knee after undergoing total hip arthroplasty (THA) and total knee arthroplasty (TKA). Lastly, we will provide a brief summary of the gaps in the literature that this thesis intends to address.

2.1 Computational Musculoskeletal Simulations

The analysis of musculoskeletal systems using mathematical models and computer simulations is called computational musculoskeletal simulations. These simulations usually involve models of bones, muscles, joints, and soft tissues and can simulate various activities, including simple daily movements like walking or reaching and more complicated ones such as sports or surgical procedures [17, 18]. These models enable researchers to obtain a better understanding of the biomechanical factors that form the basis of human movement, such as muscle activation patterns, joint forces, and energy expenditure. By analyzing the intricate interactions between the musculoskeletal system and the environment, researchers can develop novel interventions to enhance human health and performance.

There are two primary classifications of musculoskeletal simulations [18]. The first category is experiment-driven or semi-predictive simulations, which necessitate experimental data such as kinematic data or measured external forces like ground reaction forces. The second category is fully-predictive simulations, which don't require any experimental data and can synthesize motion through optimal control techniques. In fully-predictive simulations, motion is predicted based on an assumed task-dependent optimality criterion, such as minimum energy, minimum stress, or minimum fatigue [16, 19]. This thesis uses both approaches, and thus, in this section, we will provide an overview of past research in both categories before offering a more comprehensive review of sit-to-stand and stooping motion simulations which are the two main motions studied in this thesis to investigate the hip and knee joint.

2.1.1 Experiment-driven Musculoskeletal Simulations

Inverse Dynamic Approach

The inverse dynamic method is one of the primary experiment-driven techniques employed in musculoskeletal simulations [20,21]. This method utilizes the measured motion as input to the simulation, and the resulting forces, such as muscle forces or joint reactions, that are responsible for the motion are calculated as outputs. The input data typically includes body segment positions and orientations, as well as external forces, such as foot-ground interactions, while the output data includes muscle forces and joint reactions [20]. This technique depends on obtaining the accelerations of the body segments, which can be acquired through differentiation of the position data, in cases where accelerations are not directly available.

An essential challenge in the inverse dynamics approach is the mathematical indeterminacy related to the muscle recruitment problem. Specifically, the number of equations is less than the unknown muscle forces, which corresponds to the number of degrees of freedom (DoF) of the model. Consequently, there are infinite solutions for muscle forces that satisfy the equations of motion in such an indeterminate system [22]. To tackle this problem, one approach is to decrease the number of muscles to match the DoF of the system. However, this strategy leads to a simplified representation of musculotendon dynamics and may result in inaccurate estimates of joint reaction forces. An alternative method is to address muscle redundancy through an optimization problem, which selects an optimal solution among all the possible solutions [23]. One method of optimization commonly utilized in the inverse approach to tackle muscle redundancy issues is known as static optimization. In static optimization, an optimization problem is independently solved at each time instant, with a cost-function dependent on muscle forces minimized according to some assumed optimality criteria (such as minimum sum of squared muscle forces) [24]. The principle behind minimizing the cost function is based on the notion that the central nervous system aims to minimize some type of muscle force-related metric when it recruits motor units in muscles. The use of different cost-functions may result in distinct

patterns of muscle forces [25]. Also, in the static optimization method, it is not possible to define the cost-function based on the time history of the simulation, such as metabolic energy. This limitation may cause sudden fluctuations in control inputs [18]. Moreover, due to numerical constraints, static optimization can only handle simplified Hill-type muscle models [26], which may produce unphysiological outcomes. One of the significant advantages of the inverse approach is its computational efficiency compared to other methods because it does not require numerical integration of the equations of motion over time.

Forward Dynamic Approach

Forward dynamics is another experiment-driven method used in simulating musculoskeletal systems. It works by taking the muscle forces, along with other external forces like ground reaction force, as inputs and generates the kinematics of the system as an output. Considering that muscle forces cannot be measured directly, they are usually calculated based on muscle excitations, which can be obtained from electromyography [18]. Forward dynamics can also be utilized in a control system framework for tracking known motion data [27]. Several methods based on this approach have been developed, such as computed muscle control (CMC), which is a feedback control method that uses a PID controller, static optimization, and forward dynamics models to track experimental motion data by adjusting the muscle forces to minimize the error between experimental and feed-forward models [28–30]. However, using foot-ground contact forces in CMC can lead to inconsistencies between estimated motion and experimental data, and the explicit integration techniques used in CMC may result in poor convergence [18].

In general, although experiment-driven approaches are useful in estimating unmeasurable quantities such as muscle forces or joint contact forces, they are not suitable for predicting new motions and exploring hypothetical scenarios.

2.1.2 Predictive Musculoskeletal Simulations

Predictive simulations differ from experiment-driven methods in that they do not rely on experimental measurements and instead predict motion based on the assumption that human movement is optimal in terms of energy expenditure, performance, effort, or a combination of factors [31]. One advantage of predictive simulations is the ability to perform "what-if" analyses of various scenarios [16, 32–34], such as different implant positioning, and optimize outcomes, such as achieving maximum joint stability, before carrying out the intervention. However, predictive modeling faces challenges due to the lack of input data, such as kinematics and ground reaction forces, which make the results highly sensitive to the assumptions made to define optimality [35]. Defining a suitable cost-function is challenging, and it requires selecting an appropriate function based on the individual's condition. For example, the cost-function used for an elderly adult may differ significantly from the cost-function used for a young athlete doing the same activity, such as sit-to-stand. Common cost-functions aim to minimize joint torque, muscle activation, generated power, reaction force, and jerk.

The rest of this section focuses specifically on sit-to-stand motion and stooping down/lifting movements, which are used in this thesis to study the biomechanics of the hip and knee joint following THA and TKA. A comprehensive review of predictive simulations for human movement can be found in [16].

2.1.3 Previous Work on Sit-to-stand Simulations

The sit-to-stand motion is the action of shifting the body's center of mass from a seated position to a standing position while maintaining stability [36]. This movement has been studied for its biomechanics and applied in various fields, including the design of assistant robots [37, 38], movement disorders [39], and the development of exoskeletons for rehabilitation in robotics-based rehabilitation [40–42].

In this thesis, we will mainly focus on studying the mechanics of the hip and knee

joints during the sit-to-stand motion because it is a prevalent movement in daily life (the average person stands up from a chair approximately 40-50 times per day [43]), and it places significant demands on the knees (the joint contact force during sit-to-stand peaks at 200% of body weight), which can stress implants to their limits. Moreover, the knee undergoes the most extensive range of motion during sit-to-stand compared to other daily activities, which is important to note because a reduced range of motion is one of the leading causes of dissatisfaction after TKA. Additionally, the sit-to-stand motion has been recognized as a daily activity that may cause hip dislocation in patients who have undergone THA [44].

When modeling the sit-to-stand motion, the human body is commonly assumed to be symmetrical and confined to the sagittal plane. This assumption has led to the creation of multilink systems with varying numbers of components. The simplest of these systems is the three-link model, which consists of links for the shanks, thighs, and HAT (head, arms, and trunk), connected by joints at the hip, knee, and ankle [31, 45]. Occasionally, a foot link is included, but this does not affect the degrees of freedom. The three-link model is the most commonly used method for predicting sit-to-stand motion and was first introduced in a study by Hemami et al [46]. This model has since been used in various research works in both experiment-driven and predictive frameworks. However, it has been demonstrated that including arms is crucial for certain conditions, such as in the case of older adults [47]. Therefore, more complex models have been developed, such as the six- and seven-link systems, which incorporate upper and lower arms and the torso in addition to the thighs, shanks, and feet [38, 47, 48]. These models are typically utilized to account for the impact of lumbar and torso joints and arms on sit-to-stand motion.

In some studies, the conventional assumption of symmetrical motion in the sagittal plane when performing sit-to-stand actions is not considered, and instead, three-dimensional simulations are utilized. These models are generally utilized to examine sit-to-stand movements that are not symmetrical. The first instance of a three-dimensional model being used for this purpose can be found in a study by Kuzelicki et al. [49], in which they utilized a five-link 3D model (with one link representing each shank and thigh, and one link representing the HAT) in a experiment-driven simulation. The inverse dy-

namics approach was employed, wherein the motion was optimized by representing each joint angle as B-splines with five control points for each degrees-of-freedom (DoF). Later, eight-link [50] and nine-link [51] 3D models were also developed for analyzing sit-to-stand movements in three dimensions.

Researchers have explored various cost-functions in predictive simulations. Some cost terms are based on kinetic metrics like torque, force, and energy expenditure, while others are kinematic-based and focus on minimizing factors such as jerk and joint angular velocity. Typically, a combination of these factors is used in a cost-function to achieve accurate predictions. For instance, Kuzelicki et al. [49] used a multi-objective cost-function that combined minimum effort, minimum jerk, and minimum difference between left and right GRF to obtain sit-to-stand (STS) motion in a five-link torque-driven three-dimensional model. In another study, Yamasaki et al. [52] used dynamic optimization to examine the trajectory of the center of mass during STS movement of a three-link sagittal torque-driven model using a minimum jerk model. Similarly, Sadeghi et al. [37] decomposed STS motion into three successive phases and used a combination of minimum torque change, minimization of torques, and kinetic energy minimization. In Geravand et al.'s study [48], a combination of minimum effort, minimum torque change, minimum jerk, and human balance was used to predict STS motion of a four-link sagittal model. Ozsoy et al. [51] used a multi-objective cost-function of dynamic effort and left-right GRF difference to predict STS motion of a nine-link torque-driven spatial model, which showed symmetric left and right joint angles and forces. In another study by Mombaur et al. [38], sit-to-stand motion was predicted for a 7-DoF torque-driven sagittal model in the presence of an assistive device using a two-phase optimal control problem with a multi-objective cost-function of joint torques, mechanical work, angular velocity of the head, and smoothness of external force profiles. In a separate study, Norman-Gerum and McPhee. [31] used an inverse dynamic-based predictive simulation of STS with a three-link model and Bezier curves. They found that a compliant buttocks-chair model improved model accuracy due to large deformations during STS. After obtaining optimal joint torques through inverse dynamic modeling, hip and knee joint torques were mapped to 10 muscles that actuate the

lower limbs using static optimization with a simplified muscle model that lacked muscle dynamics. In a study by Bobbert et al. [45], constraints were imposed on the isometric knee extensor forces and tibiofemoral compression force to investigate the effect of muscle weakness and pain at the knee joint on predicted sit-to-stand motion using a three-link model with no arms.

A thorough analysis of the literature reveals that previous research on predicting sit-to-stand motion has mainly focused on healthy adults, and only a limited amount of investigation has been done to predict such motion for individuals with impaired or unhealthy conditions. Moreover, most of the earlier studies have utilized torque-driven or simplified muscle models, which could result in imprecise estimations of joint reaction force, an essential factor in analyzing joint biomechanics. Millard et al. [47] highlighted the significance of incorporating the nonlinear properties of muscles and the role of arms when predicting sit-to-stand motion for older adults. These two aspects are additional limitations of most prior research in this area.

2.1.4 Previous Work on Stooping Down/Lifting Simulations

In addition to sit-to-stand movements, stooping down and lifting are also frequent activities in daily human life that may increase the risk of hip dislocation following THA [44, 53]. Predictive methods have shown promise in generating realistic lifting motions and reducing reliance on motion data [54–56]. Objective functions frequently used for lifting prediction include the ratio of muscular utilization [19, 57–61], stability [62], and smoothness of load motion [63, 64].

Many previous studies have incorporated subject-specific motion data obtained through experiments into their models to improve prediction accuracy. For instance, Xiang et al. [66] utilized motion capture data to limit the predicted joint angles, while Zaman et al. [67] used experimental joint angles for predicting lifting at the beginning, middle, and end stages. Similarly, some other studies have used initial or final postures that match those observed in experiments [55, 65, 68]. Although these constraints based on

experiments aid in improving prediction accuracy, they are only valid for specific subjects and lifting conditions. The constraints for one person's posture cannot be generalized to other individuals. These models become less effective in predicting new motion when new motion data is not available.

Similar to sit-to-stand, the majority of studies regarding predictive simulation of lifting have focused on able-bodied individuals. Nevertheless, evidence suggests that the flexibility of the hips and lower back could be significant factors in determining the lifting motion pattern [19].

2.2 Hip Biomechanics

Hip joint biomechanics for daily activities have been studied using computer simulations in the past. Musculoskeletal models have been employed to calculate the reaction forces occurring within the hip joint for basic tasks like walking and transitioning from sitting to standing. These calculated forces have been compared to measured data obtained from instrumented hip implants. The predicted reaction forces from both scaled generic models [69–72] and subject-specific models [73] were reasonably accurate, with average differences of 0.69 times body weight (BW) for the initial peak in subject-specific models compared to 1.04 BW for the generic model. It has been observed that various factors, such as hip geometry and the musculoskeletal model employed, influence the results. Incorporating details like muscle wrapping and subject-specific information has been shown to enhance the accuracy of the model's predictions by approximately 30% [73].

Proper cup orientation is reported as the most significant factor to reduce the risk of dislocation [4]. The widely adopted guideline for the cup orientation is the *Lewinnek safe zone* [6]. However, this metric has been shown to have minimal correlation with the risk of hip dislocation [7, 8], which depends on subject-specific factors such as pelvic tilt and spine flexibility — factors that are ignored by the Lewinnek guidelines. Therefore, there is a need for the development of new subject-specific technologies that can reduce the risk of

complications after THA to prevent revision surgeries and improve the quality of life for patients.

Previous modelling research to study the underlying mechanisms of hip dislocation has been limited in scope, and focused mainly on sit-to-stand motions. The reason is two-fold: standing up from a chair is a common activity that one performs 40-50 times per day [74], and hip dislocations following THA often occur during sit-to-stand [44, 53]. Finite element analysis (FEA) is a widely recognized method used to analyze edge-loading and impingement in THA. It has been employed to investigate various factors affecting THA outcomes, including the alignment of the acetabular component and implant design. [75–83]. Additionally, in a recent study [84], FEA was employed to determine the contact pressure in an artificial hip. However, the study had certain limitations, as it only considered a single static pose (seated) and applied a representative static force to the joint. The study revealed that an anterior tilt of the pelvis led to edge loading of the cup, potentially resulting in edge wear and an elevated risk of dislocation.

To understand how the pelvic tilt and contact pressure change in the entire range of a motion, a dynamic simulation needs to be carried out. In one of the few papers on the subject, Pierrepont et al. [85] used a quasi-static analysis to calculate the trajectory of the contact force inside the cup surface, interpolating between static X-ray images of flexed seating and standing. However, true sit-to-stand is a dynamic movement [31], and joint loads can be higher than those predicted by quasi-static analysis.

Various methods have been introduced to account for the variation in pelvic tilt when determining the optimal orientations of impingement-free cups in functional cup alignment [86–97]. Functional cup alignment techniques enable the investigation of the impact of implant component placement, such as femoral antetorsion or combined anteversion [93, 96, 97], as well as prosthesis-specific parameters like the head/neck ratio [92, 93] and cup and neck design [92], on the range of motion of the hip joint without impingement.

However, these kinematic approaches only consider the relative motion of the femur with respect to pelvis to predict impingement; the effects of full-body motion and its dynamics

are neglected. The problem with kinematic-based optimal cup orientation determination is that hip dislocation is not only dependent on impingement, but also on kinetic factors such as hip contact forces and edge-loading [98]. Hence, a modelling platform to predict pelvis and femur motion and forces in a full-body dynamic analysis, in a variety of daily activities, is required.

Several studies have included other sources of hip dislocation such as bony coverage [99], bony impingement [100], edge-loading [98] and wear [93, 101] to determine the optimal cup orientation. However, since they are based on FEA or force plate measurements, they might not be suitable for clinical applications as they are time-consuming, complex, or expensive.

2.3 Knee Biomechanics

Both experimental and theoretical methods have been employed to examine the mechanics of the knee after TKA. Mathematical approaches, especially musculoskeletal models, are particularly intriguing due to their ability to make predictions. For example, a musculoskeletal model can be used to predict alterations in knee loads and movements resulting from modifications in implant design, alignment, or patient anatomy [102, 103]. This section will provide an overview of recent research on knee modeling, specifically focusing on TKA, from various perspectives including contact models, musculoskeletal simulations, and optimizing implant positioning to enhance TKA outcomes.

2.3.1 Contact Modeling of Knee Implants

Over time, researchers have utilized different approaches to simulate contact interactions within the field of multibody analysis [104]. In the context of TKA, understanding the contact interactions between the articulating surfaces and predicting ligament forces and secondary motions of the knee joint is crucial for improving surgical outcomes. Regarding

knee contact modeling, these methods can be broadly classified into three primary types: finite-element models [105], elastic-foundation models [30,106], and surrogate contact models [107].

Finite-element (FE) models have been widely utilized for computational dynamic analyses of TKA [105, 108, 109]. These models simulate the knee joint by discretizing it into small elements, allowing for detailed analysis of the contact interactions. FE models consider the complex behavior of materials and account for non-linearities, making them suitable for capturing intricate knee joint mechanics. However, FE models require significant computational resources and time to complete simulations. Hence, despite their accuracy, FE models may not be ideal for conducting repeated dynamic analyses and optimization studies [107, 110].

To address the computational burden of FE models, researchers have explored the use of elastic-foundation (EF) models and surrogate contact models (SCM). EF models estimate contact forces by considering the interpenetration between the contacting bodies using a layer of discrete springs over a rigid base [106]. These models offer a significant advantage of reducing computational time compared to FE models, allowing dynamic simulations of joint mechanics to be completed within minutes rather than hours. EF models have shown good agreement in terms of kinematics with more computationally intensive deformable FE models and provide good estimations of contact area and pressure distribution [111], with differences smaller than 10%.

An advancement in EF-based contact modeling occurred when Gonthier et al. introduced the volumetric contact model [112]. This model represents the contact surface as a continuous collection of springs. When the contact geometry is simplified to basic shapes like spheres or planes, analytical equations can describe the contact forces, resulting in a computationally efficient model compared to FE or discrete EF models. An illustrative example of the volumetric contact method's application is found in Brown's model [113]. Brown was the first to adopt the volumetric contact method and to develop a proof-of-concept passive knee model based on Abdel-Rahman et al.'s model [114]. In Brown's

model, tibiofemoral contact was represented as rigid contact between spheres and planes, incorporating 12 linear ligament elements. The model operated faster than real-time and produced similar normal contact forces to Abdel-Rahman's EF-based knee model. It is important to note, however, that Brown's model did not incorporate the muscles surrounding the knee joint and the patella.

Surrogate contact models have emerged as another rapid alternative to FE models, aiming to reduce the computational load of musculoskeletal simulations while preserving a satisfactory level of accuracy. These models essentially establish a fitted non-linear relationship between the pose of the contacting surfaces and the resulting contact forces and moments (nonlinear bushing). Typically, this relationship is obtained based on reference contact models, such as FE contact models. By utilizing surrogate contact models, a significant reduction in computation time can be achieved.

One approach proposed by Eskinazi and Fregly involves using an artificial neural network (ANN)-based surrogate model to accelerate an FE deformable contact model of TKA [107]. This surrogate model has shown promise in reducing computational time while maintaining accuracy. Adaptive surrogate modeling techniques have also been demonstrated by Halloran et al. [115], who accelerated the optimization of jump height in a combined musculoskeletal and FE model of the foot .

Surrogate contact models have been utilized for analyzing various aspects of TKA, including cartilage stresses [116] and tibiofemoral contact interactions and wear [117, 118]. However, these models have two important limitations. The first limitation is that a new surrogate contact model needs to be generated whenever there are changes in the geometries or material properties of the contacting bodies [107]. The second limitation is that surrogate models must be trained using extensive experimental data or dynamic simulations from another computationally expensive contact model, such as FE analysis. Therefore, the accuracy of the surrogate models relies on the reliability and precision of the reference models or data.

2.3.2 Musculoskeletal Modeling

The recent literature includes several works that focus on predicting the mechanics of the knee joint and assessing the accuracy of musculoskeletal models through experimental data. Thelen et al. [30] introduced a modeling technique for co-simulation of a body-level model and a joint-level model for gait. Their approach utilized forward dynamics coupled with CMC to predict muscle activation and tibiofemoral forces using an EF model of TKA. Similarly, Guess et al. [119] employed a comparable method to investigate the mechanics of the knee joint during walking using an EF-based 12-DOF knee model to estimate TF forces.

Hast el al. [120] developed a "dual-joint" model for the knee joint. This model employed an ideal revolute joint model and utilized inverse dynamics analysis to estimate muscle forces. Subsequently, a forward dynamics analysis of a 12-DOF knee model based on the EF approach was employed to predict contact forces.

Andersen et al. [121] introduced an enhanced inverse dynamics-like approach called Force-Dependent Kinematics (FDK), which simultaneously computes internal forces and joint kinematics. They achieved this by assuming that the secondary knee DOFs, which involve movements other than flexion-extension, are not influenced by the overall model dynamics and can be solved assuming quasi-static equilibrium among ligament, muscle, and contact forces, as well as external loads.

From the literature review, it becomes evident that the majority of previous studies have primarily focused on gait simulations when conducting and validating research [122–127]. However, it should be noted that activities requiring higher knee bend such as sit-to-stand exert substantial stress on knee implants and necessitate a greater range of motion compared to walking [128–130]. Surprisingly, there has been a dearth of research on predicting and validating models for deep knee bend activities [131–135].

Furthermore, among the studies that have examined deep knee bend activities, only a handful have validated their findings against experimental data. One notable study

conducted by Mizu-uchi et al. [131] achieved reasonably accurate predictions (with an error of approximately 9% for peak tibiofemoral contact forces) of tibiofemoral contact force using subject-specific models of two patients during squatting. Their approach involved inverse dynamics computation to obtain joint torques and changes in muscle lengths, which were subsequently utilized in forward dynamics analysis to compute tibiofemoral and patellofemoral contact forces. One significant limitation of their model was the absence of efforts to reduce muscle redundancy, as muscle forces were solely computed based on muscle lengths.

2.3.3 Optimal Knee Implant Positioning

The primary objective of TKA is to alleviate pain and facilitate the return of patients to their normal daily routines. Despite being one of the most effective procedures in orthopedic surgery, approximately 25% of individuals who undergo TKA continue to experience symptoms after the surgery [136]. Dissatisfaction among patients following TKA has been attributed to factors such as knee joint instability, implant loosening, and implant failure [10].

The positioning of the implant in TKA is recognized as a critical surgical decision that significantly impacts the functional outcome of the knee after surgery [137]. Proper placement of the femoral and tibial components plays a crucial role in achieving optimal tensioning of the surrounding soft tissues and maintaining balance and stability throughout the range of knee flexion. Conversely, incorrect positioning of the implants can result in abnormal tensions in the ligaments and uneven loading on the implants, leading to deviations in joint movement and potential complications associated with implant wear and loosening [138].

Despite the progress made in navigation and robotic systems for joint replacement surgery, which improve the accuracy of implant placement compared to manual methods [139, 140], the quest for a systematic method to achieve the ideal positioning of knee

implants in TKA tailored to individual patient requirements, and ultimately achieve post-surgical satisfaction, remains a challenge that has yet to be fully addressed [10,141,142]. In this section, we will examine the most significant previous studies regarding the acquisition of patient-specific optimal knee implant positioning.

Over the past few years, there has been an increasing emphasis on achieving precise alignment in TKA to improve patient satisfaction [143] and numerous approaches have been proposed to achieve optimal positioning and balance of the knee joint after surgery [144]. In the past, mechanical alignment (MA) has been the conventional method used for placing implants, utilizing standard surgical instruments and imaging techniques. MA focuses on aligning the femoral and tibial components perpendicular to the mechanical axis of each bone, thereby aligning their mechanical axes [145]. However, this approach may not be optimal for patients with pre-existing varus alignment [146]. Kinematic alignment (KA) has been suggested by some researchers as an alternative approach. KA aims to recreate the obliquity of the joint line and the natural tibiofemoral kinematics of the knee [147]. However, studies have shown that kinematically aligned knees with pre-existing deformities can result in imbalances in soft tissue tension, leading to uneven mediolateral flexion gaps [148]. In more recent developments, the functional alignment technique has emerged as a hybrid approach that combines elements of both mechanical and kinematic alignment [149]. Several investigations have indicated that the KA method may lead to increased range of motion and higher levels of post-operative satisfaction in TKA when compared to MA [150]. However, other studies have reported similar outcomes for both techniques [151]. Therefore, a definitive consensus regarding the superior alignment method is still lacking.

After conducting a literature search, we discovered a limited number of studies investigating various aspects of implant positioning's impact on ligament laxity and load distribution between the medial and lateral sides of the knee joint [152–158]. However, we were unable to find a comprehensive study of the optimal implant positioning based on multiple criteria. A recent study by Tzanetis et al. [159] proposed a method to find the optimal positioning of knee implants by minimizing the differences between pre-existing kinematics and ligament strains and those observed after surgery. Nevertheless, this study

had a few limitations. Firstly, restoring the pre-diseased kinematics and ligament strains may not be optimal, particularly for patients with pre-existing misaligned knee joints. Secondly, important factors such as varus/valgus alignment and load distribution balance were not taken into account. Lastly, the simulations performed in the study were quasi-static and relied on a simple motion-driven knee flexion angle. In another recent study by Bartsoen et al. [160], a probabilistic planning process was developed to optimize the positioning of implant components in order to achieve a ligament-balanced TKA. Their method considered subject-specific uncertainties in terms of ligament material properties and attachment sites, as well as surgical precision typically employed in clinical practice. However, their optimization scheme only accounted for ligament balance, neglecting other factors. Thus, a comprehensive optimization approach that considers various factors related to TKA outcomes is still absent in the existing literature.

2.4 Conclusion

In this chapter, we began by presenting a comprehensive analysis and summary of the current approaches utilized in computational musculoskeletal modeling. These approaches aim to understand the complex dynamics of the musculoskeletal system and simulate its behavior under different conditions. We categorized these approaches into two primary frameworks: experiment-driven simulations and fully-predictive simulations.

experiment-driven simulations involve the use of experimental data, such as motion capture or force plate measurements, to drive the simulation. These simulations rely on capturing the kinematics and kinetics of human movement and using them as inputs to the model. While experiment-driven simulations provide valuable insights into the biomechanics of human motion, they have limitations in terms of generalizability and the ability to explore hypothetical scenarios.

On the other hand, fully-predictive simulations aim to simulate the musculoskeletal system without relying on experimentally measured movements [16]. These simulations

use mathematical models and optimal control techniques to predict the behavior of the system based on anatomical and physiological parameters. They offer the advantage of exploring "what-if" scenarios, allowing researchers to evaluate the effects of various factors such as implant positioning and subject-specific characteristics on the outcomes of joint replacement surgeries.

Within the context of joint replacement surgeries, such as THA and TKA, predictive simulations hold significant potential. By simulating different patient conditions and implant positions, researchers can optimize the implant positioning tailored to individual patients [15]. However, despite the advantages of fully-predictive simulations, we found that no previous study has utilized these powerful techniques for the analysis of THA and TKA.

This gap in the literature highlights the need for further research to explore the use of fully-predictive simulations in the context of joint replacement surgeries. Such simulations can help investigate the effect of different patient conditions, such as variations in muscle strength, ligament laxity, and chronic joint pain on the optimal positioning of the implants. By considering a broader range of patient-specific factors, these simulations could improve surgical planning and ultimately enhance the outcomes of THA and TKA procedures.

Furthermore, we identified another key gap in the methods used for optimizing implant positioning. While several studies have explored the impact of individual factors, such as joint impingement or ligament laxity, there is a lack of comprehensive optimization methods that consider multiple factors simultaneously. THA and TKA performance depend on a wide range of factors, including joint stability, range of motion, balanced load distribution, and implant wear. Developing an optimization method that properly quantifies these factors and considers them concurrently could lead to more effective and personalized implant positioning strategies.

Lastly, we found that most of the analyse on knee joint biomechanics has been limited to gait-related activities. While studying walking patterns is important, it is crucial to consider other functional activities that impose different demands on the knee joint. Ac-

tivities such as sit-to-stand and deep knee bend exert substantial stress on knee implants and necessitate a greater range of motion compared to walking. However, there has been limited research on predicting and validating models for these specific activities. Addressing this gap would provide valuable insights into the performance of knee implants under various functional tasks, enabling better design and optimization of TKA procedures.

In summary, this chapter has highlighted several key gaps in the current research on computational musculoskeletal modeling, specifically in the context of THA and TKA. By leveraging fully-predictive simulations, developing comprehensive optimization methods, and exploring a wider range of functional activities, researchers can advance our understanding of joint biomechanics and improve the outcomes of joint replacement surgeries.

Chapter 3

Optimizing Acetabular Cup Orientation Following THA using Motion Capture and Inverse Dynamics

3.1 Introduction

In this thesis, two methods have been employed to determine the optimal placement of the acetabular cup in total hip arthroplasty. The first of these methods, called the inverse dynamic approach, is outlined in this chapter. It entails utilizing motion capture data to compute the hip contact force and the relative orientation of the femur and pelvis via a musculoskeletal model. The risk of impingement and edge-loading are then assessed for various cup alignments using two quantitative indices, and an optimal cup alignment is estimated using three optimization criteria that balance the risks of impingement and edge-loading. This method eliminates the need for force plate measurements, making it more practical and cost-efficient.

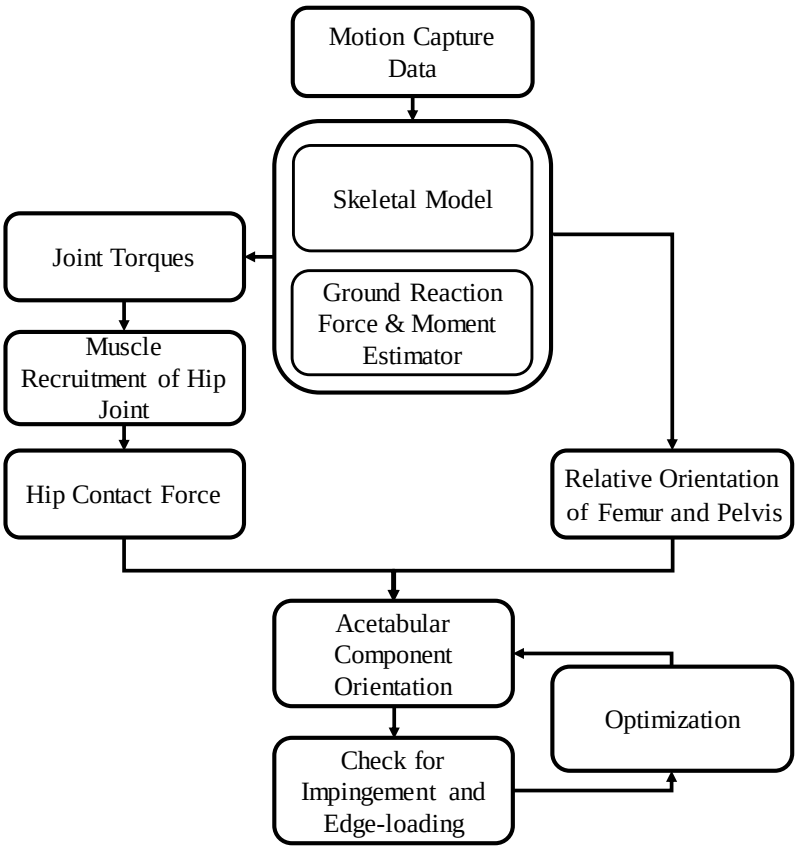

Figure 3.1: The framework of the proposed methodology for obtaining the optimal acetabular cup orientation for THA.

The main components of the inverse dynamics approach proposed in this research are shown in Fig. 3.1. First, by using motion capture (MoCap) data obtained from the patient, the hip contact force and the orientation of the femur with respect to the pelvis was calculated at each instant by the use of a musculoskeletal model. In this method, ground reaction forces and moments (GRF&Ms) was estimated instead of using force plate data. Then, the safest orientation of the acetabular cup was calculated by concurrently minimizing the risk of impingement and edge-loading. Each component shown in Fig. 3.1 has been explained in more detail in the following sections.

The remaining sections of this chapter are structured as follows: In Section 3.2 the motion capture data used in this chapter is presented. Section 3.3 provides an introduction to the musculoskeletal model used in this study, encompassing the skeleton model, the approach employed for estimating GRF&Ms,the muscles surrounding the hip joint that were modeled and model validation. Section 3.4 defines implant impingement and edge-loading and introduces two qualitative indices that are used throughout this thesis to assess the distance to impingement and edge-loading for various movements. In Section 3.5, three different optimization criteria for acetabular cup alignment are defined and used to optimize the cup orientation. The findings of the optimal cup orientation for various daily activities and the impact of pelvic tilt on the optimal cup placement are presented in Section 3.6. Finally, Section 4.6 concludes this chapter with remarks and comments on the findings.

3.2 Motion Capture Data

The motion input to the model for demonstrating the proposed method was obtained by utilizing the processed joint angles from Carnegie Mellon University's Graphics Lab MoCap database [161]. The first and second numerical derivatives of the joint angles were computed to derive the angular velocity and acceleration of the joints. Three activities of daily living — walking, sit-to-stand, and picking an object up from the ground (without bending the knees) — were selected as case studies. The reason for selecting these activities was two-fold: they are common activities that one performs throughout a day [74], and sit-to-stand and standing while bending at the waist are identified as daily living activities prone to hip dislocation after THA [44, 53]. For the sit-to-stand, data from subject #13 was used and the motion was analyzed from the seat-off phase to upright stance. For the gait, data from subject #2 was used and only the single support phase where the foot of the affected leg is on the ground was considered. And for picking an object up from the ground, data from subject #115 was used.

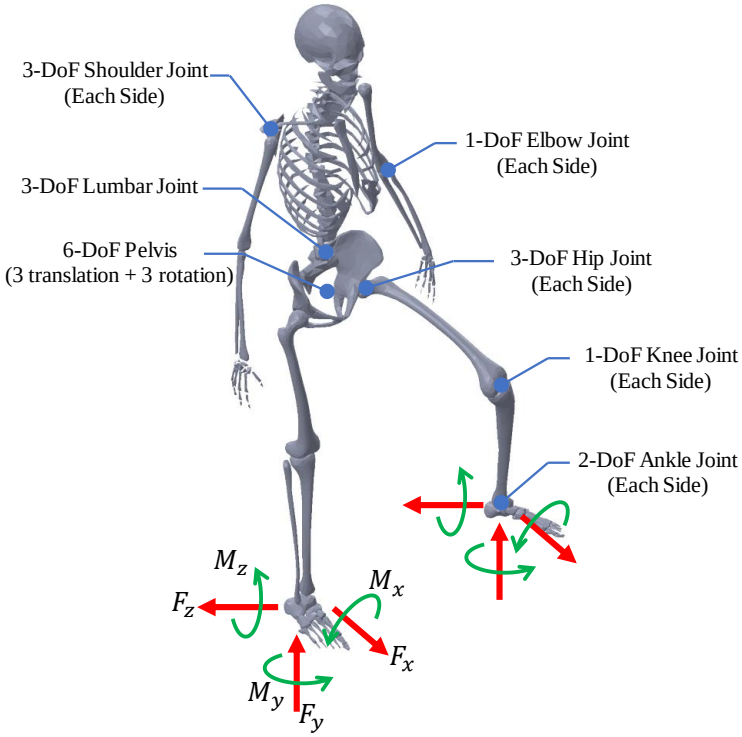

Figure 3.2: Visualization of the skeletal model used in this research. The red and green arrows respectively represent the ground reaction forces and moments on each foot.

3.3 Musculoskeletal Modeling

3.3.1 Skeletal Model

The human skeletal model developed in this research is shown in Fig. 3.2. The model consists of 12 segments: the trunk, which includes the head, and for each leg a thigh, a shank and a foot. Also included for each of the upper limbs is an arm and a forearm, which includes the hand. There are 29 degrees of freedom (DOF), including 2×2 DOF at the ankle joints (universal joint), 2×1 DOF at the knee joints (revolute joint), 2×3 DOF at the hip joints (spherical joint), 6 DOF at the pelvis, 3 DOF between pelvis and trunk (spherical joint), 2×3 DOF at the shoulder joints (spherical joint) and 2×1 DOF

at the elbow joints (revolute joint). The skeletal model was assumed to be actuated by joint torques except for the 6 DOF pelvis joint connecting the pelvis frame to the ground frame. Also, the resultant of ground reaction forces was included as an external force and moment, i.e., GRF&Ms, on each foot. The dynamic model of the human skeleton can be obtained in the following form [162]:

$$\boldsymbol{\mathcal{M}}(\mathbf{q})\,\ddot{\mathbf{q}} + \boldsymbol{\mathcal{C}}(\mathbf{q},\dot{\mathbf{q}})\,\dot{\mathbf{q}} + \boldsymbol{\mathcal{G}}(\mathbf{q}) = \boldsymbol{\mathcal{Q}}(\mathbf{q}) \begin{bmatrix} \boldsymbol{\mathcal{F}}_G \\ \boldsymbol{\tau} \end{bmatrix} \tag{3.1}$$

where $\mathbf{q}_{29\times1}$ contains the generalized coordinates and $\boldsymbol{\mathcal{M}}(\mathbf{q})$ is the mass matrix, $\boldsymbol{\mathcal{C}}(\mathbf{q},\dot{\mathbf{q}})$ contains the Coriolis forces, and $\boldsymbol{\mathcal{G}}(\mathbf{q})$ includes the gravity forces. Also, $\boldsymbol{\tau}_{23\times1}$ is the vector of joint torques and $\boldsymbol{\mathcal{F}}_G$ contains the GRF&Ms exerted on both feet:

$$\boldsymbol{\mathcal{F}}_G = \begin{bmatrix} \begin{bmatrix} F_x & F_y & F_z & M_x & M_y & M_z \end{bmatrix}^T_{\text{Right}} \\ \\ \begin{bmatrix} F_x & F_y & F_z & M_x & M_y & M_z \end{bmatrix}^T_{\text{Left}} \end{bmatrix}_{12\times1} \tag{3.2}$$

Furthermore $\boldsymbol{\mathcal{Q}}(\mathbf{q})$ can be written as:

$$\boldsymbol{\mathcal{Q}}(\mathbf{q}) = \begin{bmatrix} \mathbf{J}_G(\mathbf{q})^T_{29\times12} & \begin{bmatrix} \mathbf{0}_{6\times23} \\ \mathbf{1}_{23\times23} \end{bmatrix} \end{bmatrix}_{29\times35} \tag{3.3}$$

where $\mathbf{J}_G$ is the Jacobian that maps the GRF&Ms into the joint space, which can be written as:

$$\mathbf{J}_G(\mathbf{q}) = \begin{bmatrix} \mathbf{J}_{RightFoot}(\mathbf{q}) \\ \mathbf{J}_{LeftFoot}(\mathbf{q}) \end{bmatrix}_{12\times29} \tag{3.4}$$

where $\mathbf{J}_{Foot}$ is the Jacobian matrix that maps the rate of change of the generalized coordinates into the twist of the foot (i.e., linear and angular velocity, respectively written as $\mathbf{v}_{Foot}$ and $\boldsymbol{\omega}_{Foot}$):

$$\begin{bmatrix} \mathbf{v}_{Foot} \\ \boldsymbol{\omega}_{Foot} \end{bmatrix}_{6\times1} = [\mathbf{J}_{Foot}(\mathbf{q})]_{6\times29}\dot{\mathbf{q}}_{29\times1} \tag{3.5}$$

When performing inverse dynamic analysis, it is assumed that the motion of the body (i.e., $\mathbf{q}$, $\dot{\mathbf{q}}$ and $\ddot{\mathbf{q}}$) is known and the objective is to obtain the joint torques, $\boldsymbol{\tau}$.

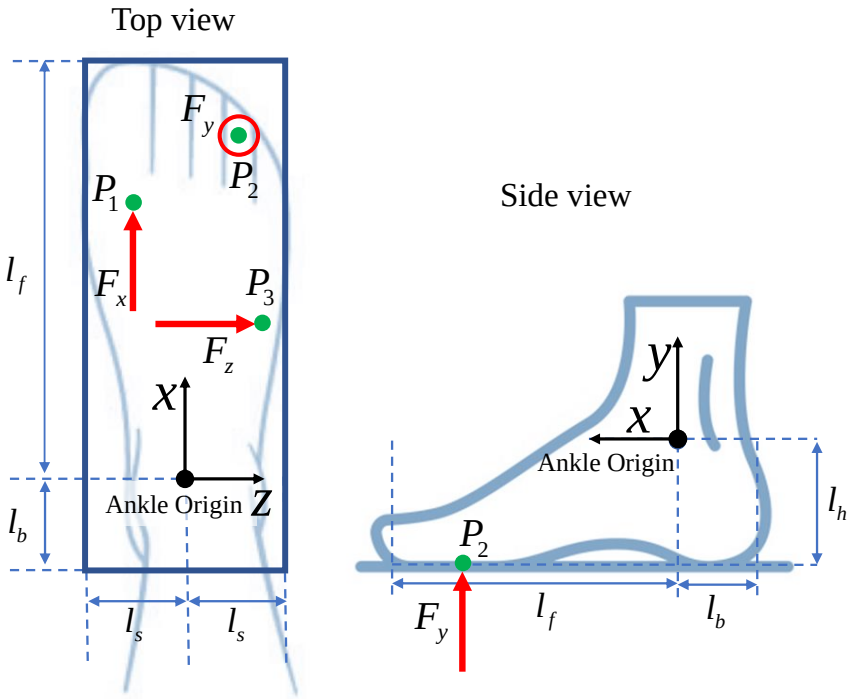

Figure 3.3: The resultant of ground reaction forces and their point of application.

3.3.2 Ground reaction force and moment estimation

During single foot support, the GRF&Ms can be obtained directly from Eq. (3.1) by setting the GRF&M on the airborne foot equal to zero and solving Eq. (3.1) for the remaining GRF&M and τ. However, when both feet are in contact with the ground, the total number of unknowns ($\boldsymbol{\mathcal{F}}_G$ includes 12 unknowns and τ includes 23 unknowns) exceeds the number of scalar equations (which are 29), resulting in dynamic indeterminacy. Typically, to circumvent this problem, force plate measurements are used to eliminate the 12 unknowns of GRF&Ms. However, in recent years, methods to estimate the GRF&Ms from kinematics and dynamic properties without using force plate measurements [163–166] have emerged, which have shown comparable accuracy to force plate measurements during activities of daily living [163], sports-related movements [164] and inertial motion capture-based gait analysis [166].

For the case of the double-support phase, a simplified version of the method proposed by [164] was implemented to estimate the GRF&Ms. The comparison made in [164] between the estimated and experimental data showed a good agreement across all movements for vertical GRFs (Pearsons correlation coefficient (r) ranging from 0.97 to 0.99, median 0.99), joint flexion moments (r ranging from 0.79 to 0.98, median 0.93), and resultant joint reaction forces (r ranging from 0.78 to 0.99, median 0.97). For the purpose of the current research, the following simplifying assumptions were made:

1. The critical stages in a movement in terms of hip joint dislocation are not during the transition phase between single stance to double stance and vice versa. This simplifying assumption allows us to avoid dealing with the stance transition phase of the movements.

2. A single wrench (a force and a moment) on each foot is sufficient to model the contact dynamics. This assumption rules out the possibility of some part of a foot to slide while other parts of the same foot are fixed to the ground.

As shown in Fig. 3.3, the position of the resultant of the ground reaction force distribution in x-, y-, and z-directions are respectively assumed to be at $P_1\left(x_1, -l_h, z_1\right)$, $P_2\left(x_2, -l_h, z_2\right)$ and $P_3\left(x_3, -l_h, z_3\right)$ described in the ankle local coordinate frame. Hence, one can obtain the moment of the forces about the center of the ankle as:

$$\begin{bmatrix} M_x \\ M_y \\ M_z \end{bmatrix} = \begin{bmatrix} -z_2 F_y - l_h F_z \\ z_1 F_x - x_3 F_z \\ x_2 F_y + l_h F_x \end{bmatrix} \tag{3.6}$$

Considering that the reaction forces should be inside the supporting area of the foot which, as shown in Fig. 3.3, is assumed to be a rectangle of length $l_f + l_b$ and width of $2l_b$, one can obtain the following constraints for the moments in Eq. (3.6) as:

$$\left|M_x + l_h F_z\right| \leq F_y l_s \tag{3.7}$$

$$\left|M_y - \frac{1}{2}\left(l_b - l_f\right) F_z\right| \leq \left|F_x\right| l_s + \frac{1}{2}\left(l_b + l_f\right)\left|F_z\right| \tag{3.8}$$

$$\left| M_z - l_h F_x - \frac{1}{2}\left(l_f - l_b\right) F_y \right| \leq \frac{1}{2}\left(l_b + l_f\right) |F_y| \tag{3.9}$$

Furthermore, considering that the normal force should always be positive and assuming no slipping on the ground, one can write:

$$0 \leq F_y \tag{3.10}$$

$$\sqrt{{F_x}^2 + {F_z}^2} \leq \mu_s F_y \tag{3.11}$$

where μ_s is the static coefficient of friction between foot and the ground. Using the inequalities provided in Eqs. (3.7) to (3.11) written for both feet along with the joint torque limits $\boldsymbol{\tau}_{\min} \leq \boldsymbol{\tau} \leq \boldsymbol{\tau}_{\max}$, the GRF&Ms for both feet and joint torques can be obtained by adapting the method used in [164] to solve the following second-order quadratic optimization problem subjected to the dynamic model, given in Eq. (3.1):

$$\min_{\boldsymbol{\tau}, \boldsymbol{\mathcal{F}}_G} \quad J\left(\boldsymbol{\tau}, \boldsymbol{\mathcal{F}}_G\right) = {\boldsymbol{\mathcal{F}}_G}^T \mathbf{S} \boldsymbol{\mathcal{F}}_G + \sum_{i=1}^{23} \left(\frac{\tau_i}{\tau_{i,\max}} \right)^2 \tag{3.12}$$

The contribution of GRF&Ms, $\boldsymbol{\mathcal{F}}_G$, and joint torques, $\boldsymbol{\tau}$, to human dynamics can be adjusted by a positive semidefinite matrix of weighting factors, denoted as $\mathbf{S}$. To illustrate this point, as shown in Fig. 3.4, a simplified case of static wide-stance was studied. The results showed that depending on the values of $\mathbf{S}$ used, different outcomes could be obtained. In case (a), where the value of $\mathbf{S}$ was very large ($|\mathbf{S}| \to \infty$), the model minimized GRF at the cost of high hip joint torque. In contrast, in case (b) where $\mathbf{S} = \mathbf{0}$, smaller joint torques resulted in a more relaxed body. Therefore, assigning relatively lower weights to GRF&Ms in comparison to joint torques has the potential to result in more realistic outcomes.

3.3.3 Hip Contact Force

The precise estimation of contact forces in the hip joint is required in this study. Therefore, as shown in Fig. 3.5, 21 muscle-tendon units are utilized to actuate the hip joint.

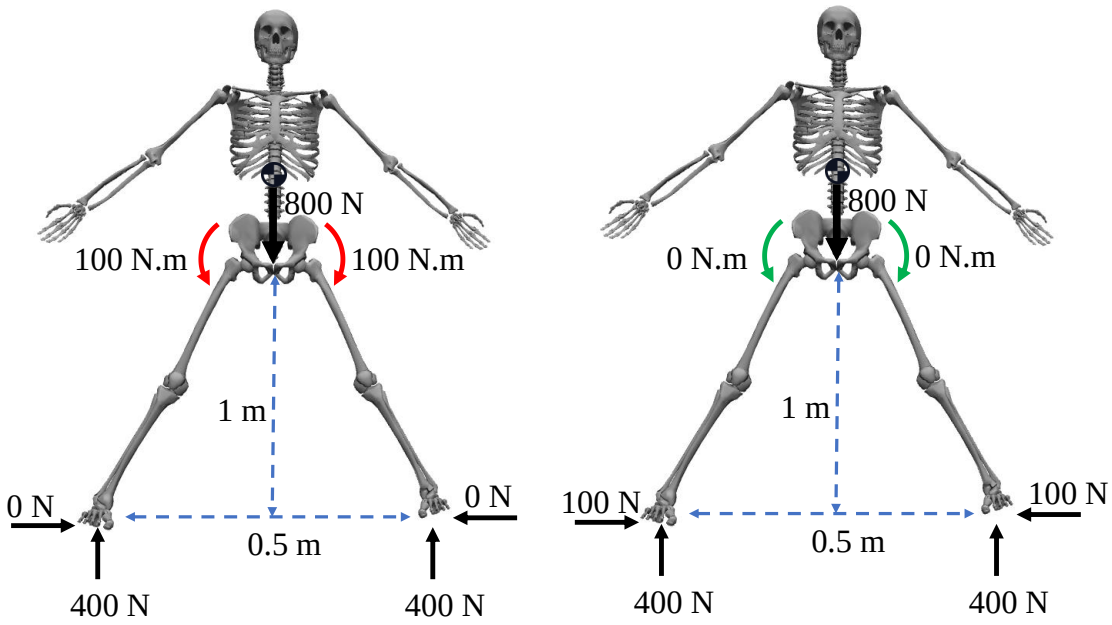

(a) No lateral ground reaction force. Hip joint must be active.

(b) Sufficient lateral ground reaction force. Hip joint is relaxed.

Figure 3.4: A simplified case study to illustrate the effect of the value of $\mathbf{S}$ on the outcome of the optimization in Eq. (3.12). (a) The optimization weight for ground reaction force is much higher than the weights for joint torques , i.e., $\|\mathbf{S}\| \to \infty$. (b) The weights for joint torques is much higher than the weights for ground reaction force, i.e., $\mathbf{S} = \mathbf{0}$.

These muscles include: adductor magnus ischial (addmagIsch), adductor magnus middle (addmagMid), adductor magnus proximal (addmagProx), biceps femoris long head (bflh), gluteus maximus (glmax), gluteus medius (glmed, 3 bundles), gluteus minimus (glmin, 3 bundles), gracilis (grac), iliacus, piriformis (piri), psoas, rectus femoris (recfem), sartorius (sart), tensor fasciae latae (tfl), semimembranosus (semimem), semitendinosus (semiten).

The characteristics of the muscles, including their origin/insertion points and wrapping geometries, were obtained from a recently calibrated musculoskeletal models [167, 168]. These models were specifically designed to accommodate high ranges of hip and knee flexion. As the inverse dynamic approach was used in this chapter, a simple muscle model

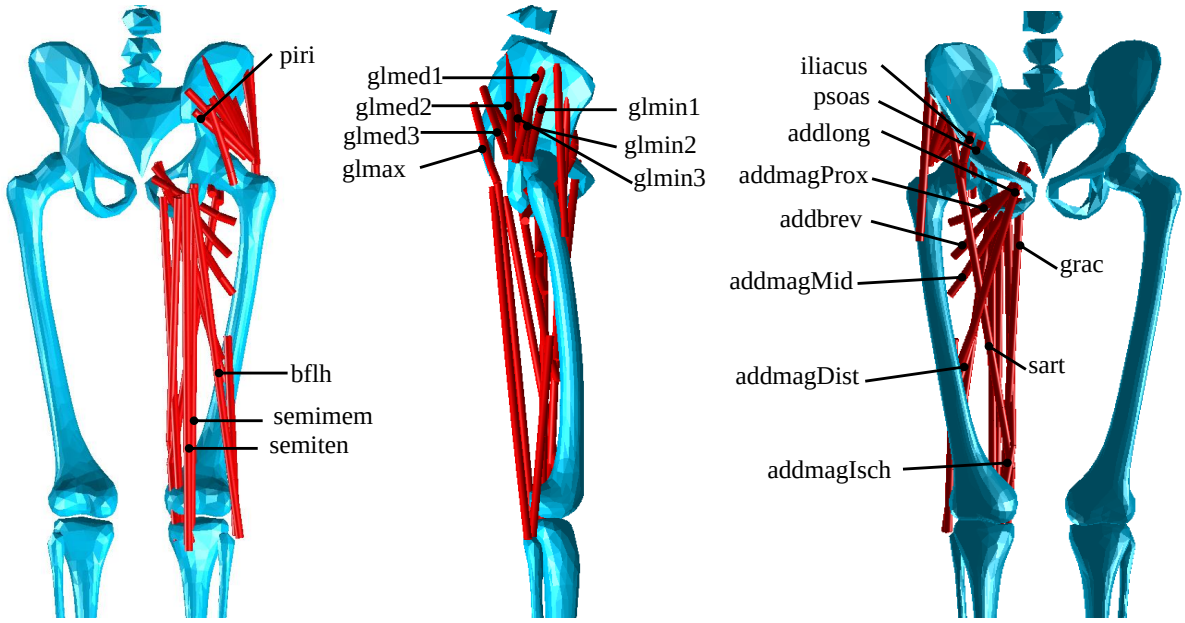

Figure 3.5: Muscles surrendering the hip joint.

without contraction/activation dynamics was employed to model the muscle elements. To obtain the muscle forces, the muscle recruitment problem was solved through static optimization, minimizing the sum of the cubed muscle forces normalized by the strength of the muscle. The optimization problem also incorporates constraints in the form of an equilibrium equation, which balances the moments of muscle forces and joint torque, as well as non-negativity restrictions that limit the muscles to only generate tension. This results in the following formulation of the optimization problem:

$$\min_{\mathbf{f}} G(\mathbf{f}) = \sum_{i=1}^{21} \left(\frac{f_i}{F_i} \right)^3 \tag{3.13}$$

subjected to:

$$\mathbf{\Psi}_{3\times 21}\mathbf{f} = \boldsymbol{\tau}_{Hip} \tag{3.14}$$

$$0 \leq f_i \quad \text{for } i = 1, \cdots, 21 \tag{3.15}$$

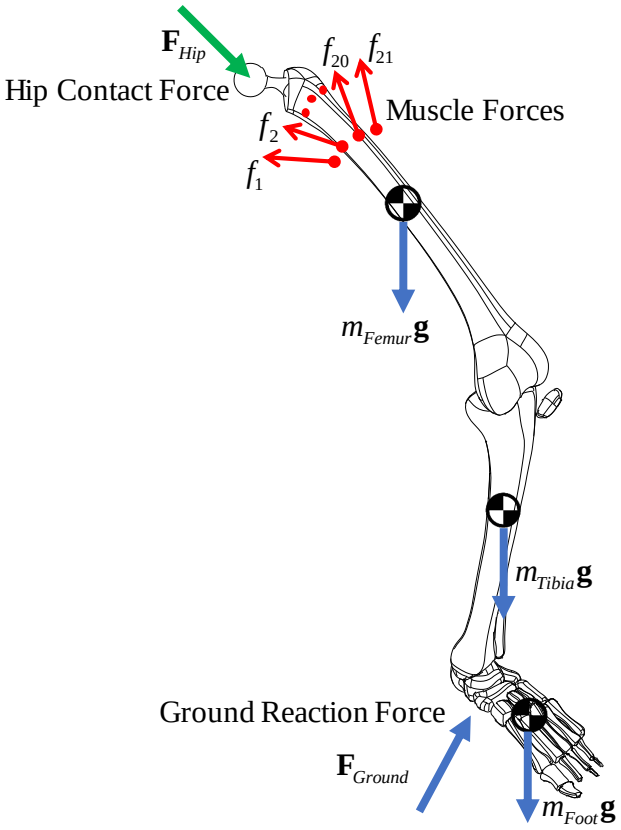

Figure 3.6: Free body diagram of a leg.

where $\mathbf{f} = \begin{bmatrix} f_1 & \cdots & f_{21} \end{bmatrix}^T$ is the column matrix containing the muscle forces, F_i is the maximum isometric force of ith muscle (i.e., maximum isometric force), and $\mathbf{\Psi}$ is the matrix of muscle moment arms mapping the muscle forces into the hip joint torque. Once the muscle forces are obtained, the hip joint reaction force can be obtained from the force equilibrium equation acting on the leg as shown in Fig. 3.6, which yields:

$$\mathbf{F}_{Hip} = \sum_{\Delta=\text{Femur,Tibia,Foot}} m_\Delta(\mathbf{a}_\Delta - \mathbf{g}) - \sum_{i=1}^{21} f_i \hat{\mathbf{u}}_i - \mathbf{F}_{Ground} \tag{3.16}$$

where mass is denoted by m, $\mathbf{g}$ is the gravitational acceleration, $\hat{\mathbf{u}}_i$ is the unit vector along the ith muscle and $\mathbf{a}$ is the acceleration of the mass center.

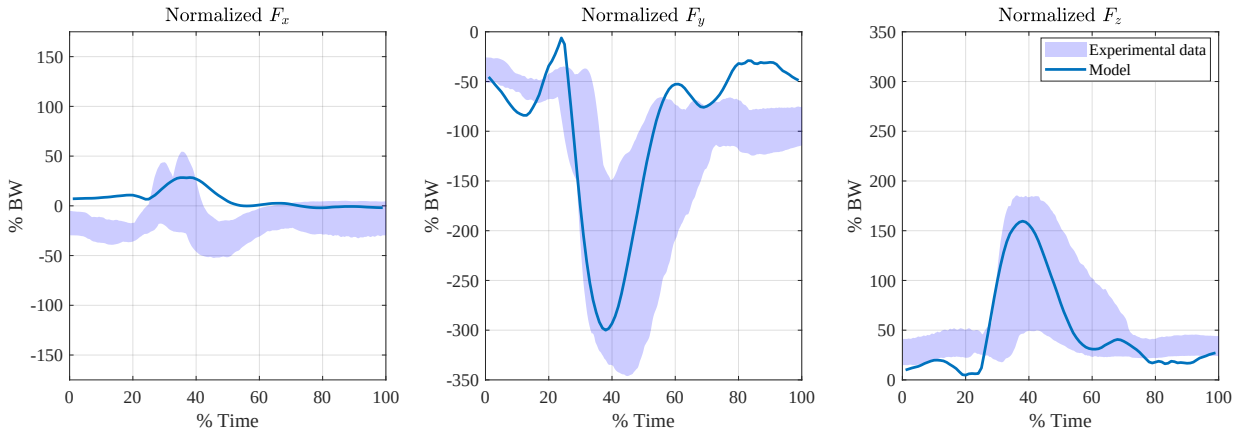

Figure 3.7: Comparison between hip joint contact forces normalized to body weight (BW) obtained from the model and experimental in vivo data from OrthoLoad dataset for 9 patients during sit-to-stand movement. The shaded region is the envelope of the 9 experimental dataset.

3.3.4 Model Validation

To ensure the precision of the model's estimation of hip joint contact force, the hip reaction force derived from the model was matched up against experimental data. Specifically, the double-stance 3D dynamic model's simulation results for the sit-to-stand (s2s) motion were compared to in vivo measurements obtained from the OrthoLoad database [169]. This comparison was carried out for the period starting from the seat-off phase to the stance phase. The OrthoLoad database consists of forces acting on the femoral stem's head for nine individuals who underwent THA, including two females and eight males. The participants had a mean age of 57.1 5.4 years, mean body weight of 91.3 12.5 kg, and mean body height of 1.72 0.06 m.

Unfortunately, the OrthoLoad dataset did not contain MoCap data. Consequently, the joint angles processed from the Carnegie Mellon University's Graphics Lab MoCap dataset for the sit-to-stand motion were employed as the input for the model. The simulation utilized the inertial parameters derived from OpenSim [170] Gait2392 and Arm26 models,

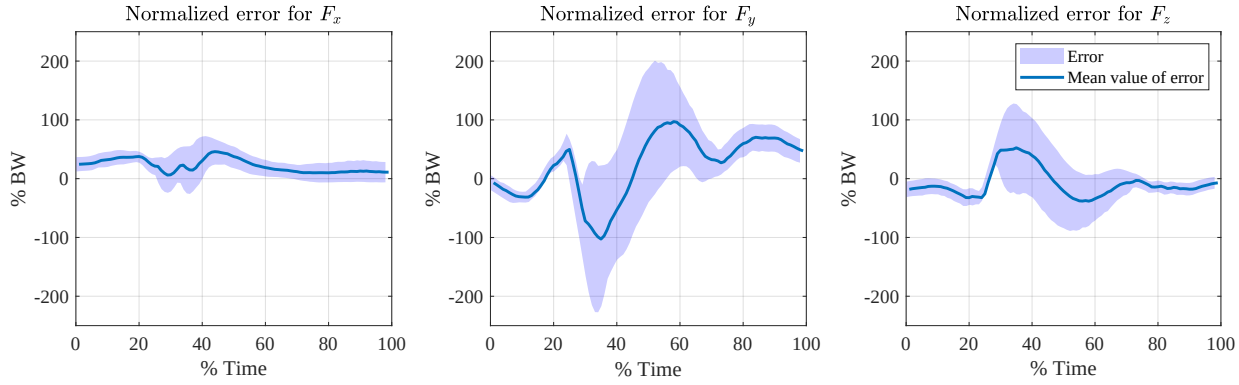

Figure 3.8: Normalized error between the model and the in vivo experimental data from OrthoLoad dataset for 9 patients shown in Fig. 3.7. The shaded region is the envelope of the error between the model and the 9 experimental dataset.

which were scaled to match the average height and weight of the nine patients in the OrthoLoad dataset. Although there exists a discrepancy between the s2s MoCap data and the s2s motion executed by the subjects in the OrthoLoad experiments, we believe that the hip contact force produced by the model should follow the same trend as the experimental data. The findings of this comparison are illustrated in Figure 3.7. In order to minimize the impact of the subjects' weights, the forces were normalized to the body weight (BW) of each subject.

The values shown in Fig. 3.7 are in the local coordinate frame of the femur defined by the International Society of Biomechanics (ISB) as shown in Fig. 3.11. The rotation matrix describing the orientation of the OrthoLoad frame relative to the ISB local frame on the femur is:

$$ {}^{ISB}\mathbf{R}_{OrthoLoad} = \begin{bmatrix} 0 & 1 & 0 \\ 0 & 0 & 1 \\ 1 & 0 & 0 \end{bmatrix} \tag{3.17} $$

Figure 3.8 illustrates the discrepancy between the model and experimental data. The shaded region represents the error envelope between the model and each experimental dataset obtained from the nine patients, while the solid line denotes the average error

value. It can be observed that in most cases, the error interval encompasses both positive and negative values. This suggests that the model overestimates the hip reaction forces for some subjects and underestimates them for others. If the motion capture data of the patients in the OrthoLoad dataset had been available, the prediction errors would have been more informative. Another source of error that must be acknowledged is the soft tissue artifact's influence on the joint angle measurements obtained through skin marker-based motion capture [171, 172]. Soft tissue artifacts can cause hip contact force variations of up to 1.8 times the body weight and up to 30-50% for certain muscle forces [173]. Nonetheless, the fact that the model-predicted reaction forces mostly align with the experimental data in Figure 3.7, or equivalently, the shaded error bar in Figure 3.8 encompasses zero for the majority of the trajectory, can be regarded as a positive outcome for this test.

3.4 Implant Impingement and Edge-loading

As previously mentioned, implant impingement and edge-loading are the two main factors for artificial hip joint dislocation. These two phenomena are illustrated in Fig. 3.9 and Fig. 3.10. Similar to the definition proposed in [174], the distance from impingement for a given pose of the artificial hip joint can be defined as the minimum angle between the stem on the femoral component and the edge of the acetabular cup. This angular distance, which we call Angular Impingement Distance (AID), can be calculated as:

$$\theta_{AID} = \frac{\pi}{2} + \alpha - \sin^{-1}\left(\frac{d_{Neck}}{d_{Head}}\right) - \phi_{Stem} \tag{3.18}$$

where referring to Fig. 3.9, α is the constant cup opening angle, d_{Neck} and d_{Head} are respectively the diameter of the neck and head of the femoral component, and ϕ_{Stem} is the time-varying angle between the stem and the cup axis of symmetry, represented by $\hat{\mathbf{n}}$. A positive value of AID, i.e., $\theta_{AID} > 0$, implies that impingement has not occurred whereas a negative value of AID corresponds to implant impingement.

Similarly, the distance from edge-loading for a given hip joint contact force can also be defined as the minimum angular distance of the direction of the contact force to the edge

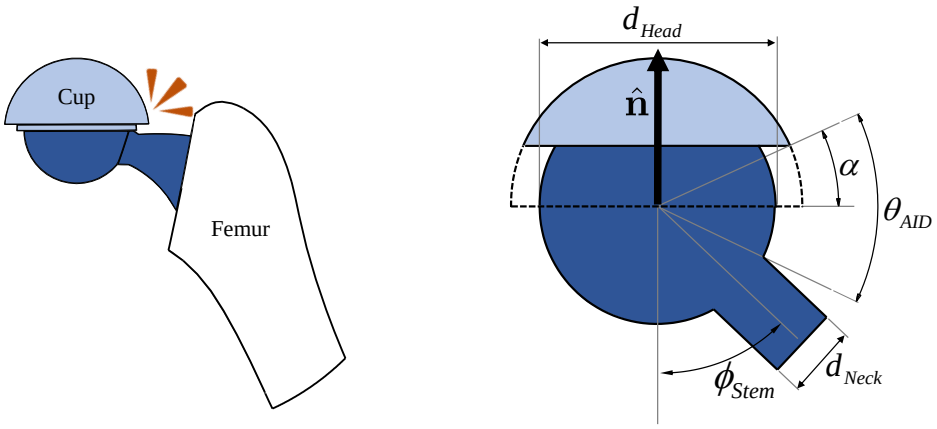

(a) Femoral neck is in contact with the acetabular cup. (b) Kinematic parameters.

Figure 3.9: Implant impingement.

of the cup, which can be obtained as:

$$\theta_{AED} = \frac{\pi}{2} - \alpha - \phi_{Force} \tag{3.19}$$

where θ_{AED} is called the Angular Edge-loading Distance (AED) and ϕ_{Force}, illustrated in Fig. 3.10, is the time-varying angle between the contact force and the cup axis of symmetry, i.e., $\hat{\mathbf{n}}$. A positive value of AED, i.e., $\theta_{AED} > 0$, indicates that the edge-loading has not occurred while a negative value of AED denotes edge-loading. Looking at Eq. (3.18) and Eq. (3.19) it is worthy to note that increasing the value of α respectively increases and decreases the range of motion in terms of impingement and edge-loading.

3.5 Acetabular Cup Orientation Optimization

For a given cup orientation and human body motion, ϕ_{Stem} and ϕ_{Force} can be calculated using the kinematic and dynamic models. Subsequently, θ_{AID} and θ_{AED} can be obtained from Eq. (3.18) and Eq. (3.19) at each instant. Considering that the greater the value of θ_{AID} and θ_{AED} are, the further the hip implant is from impingement and edge-loading,

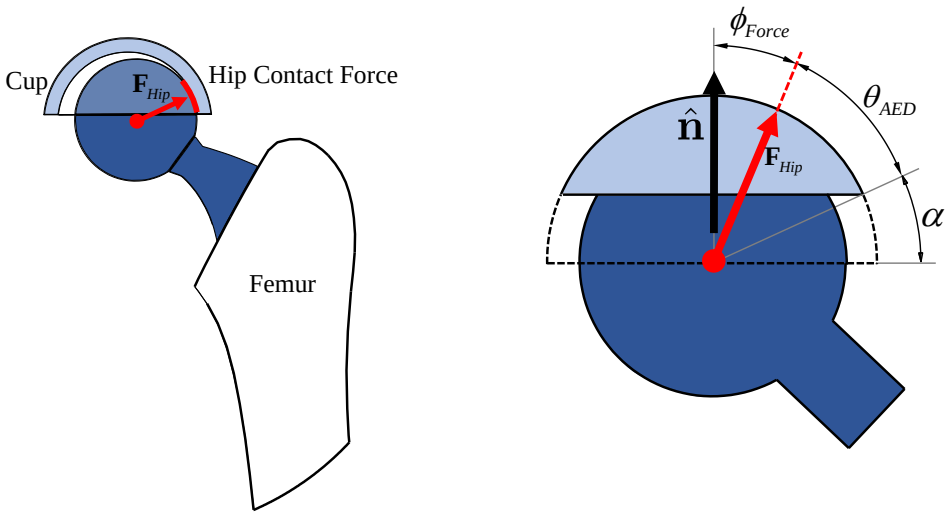

(a) Hip contact force is close to the edge of the cup. (b) Kinematic parameters.

Figure 3.10: Implant edge-loading.

the following optimization criteria are proposed and evaluated for obtaining the optimal acetabular cup orientation:

Optimization #1: Maximizing the distance from impingement and edge-loading for a given set of human movements:

$$\underset{\beta_{Ant},\beta_{Inc}}{\arg\max} \quad \left\{ \min_{0\le t\le t_f} \left\{ \theta_{AID}\left(\beta_{Ant},\beta_{Inc},t\right), \theta_{AED}\left(\beta_{Ant},\beta_{Inc},t\right) \right\} \right\} \tag{3.20}$$

where β_{Ant} and β_{Inc} are respectively the radiographic anteversion and inclination angles of the cup, as defined in [175] (Fig. 3.11), and t_f denotes the final time of the motion.

Optimization #2: Maximizing the distance from impingement for a given set of movements while keeping the distance from edge-loading above a certain threshold:

$$\begin{aligned} &\underset{\beta_{Ant},\beta_{Inc}}{\arg\max} \quad \left\{ \min_{0\le t\le t_f} \theta_{AID}\left(\beta_{Ant},\beta_{Inc},t\right) \right\} \\ &\text{subjected to:} \\ &\theta_{AED}\left(\beta_{Ant},\beta_{Inc},t\right) \ge \tilde{\theta}_{AED} \qquad \text{for } 0 \le t \le t_f \end{aligned} \tag{3.21}$$

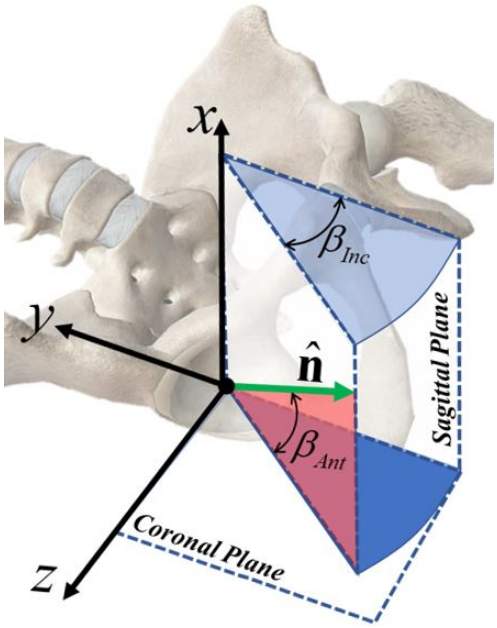

Figure 3.11: Radiographic anteversion (β_{Ant}) and inclination (β_{Inc}) [175]. The International Society of Biomechanics (ISB) standard is used to define the pelvis local coordinate frame [176].

where $\tilde{\theta}_{AED}$ is the minimum acceptable value for AED.

Optimization #3: Maximizing the distance from edge-loading for a given set of movements while keeping the distance from impingement above a certain threshold:

$$\begin{aligned} &\underset{\beta_{Ant},\beta_{Inc}}{\arg\max} \quad \left\{ \min_{0\le t\le t_f} \theta_{AED}\left(\beta_{Ant},\beta_{Inc},t\right) \right\} \\ &\text{subjected to:} \\ &\theta_{AID}\left(\beta_{Ant},\beta_{Inc},t\right) \ge \tilde{\theta}_{AED} \quad \text{for } 0 \le t \le t_f \end{aligned} \tag{3.22}$$

where $\tilde{\theta}_{AID}$ is the minimum acceptable value for AID.

3.6 Results and Discussion

3.6.1 Value of AID and AED for different daily activities

The values of AID and AED for three daily activities (sit-to-stand, walking, and picking up a box from the ground) were calculated for a wide range of acetabular cup orientations. The developed model was coded in MATLAB. The implant geometry and femoral component position used in the simulations, summarized in Table 3.1, were adapted from Widmer et al. [96]. The results are shown as contour plots in Fig. 3.12. The first plot in each row (from the left side) depicts the minimum value of AID throughout the corresponding motion in terms of radiographic anteversion and inclination of the cup. The optimal cup orientation in terms of impingement corresponds to the highest AID. When AID < 0 it means that there is at least one instant where impingement has occurred. The second plot shows the minimum distance from edge-loading, or AED, throughout the motion for a given cup orientation. Using this plot, one can determine the optimum cup orientation to minimize the risk of edge-loading by locating the maximum value of AED on the plot. Referring to Fig. 3.12 it can be observed that optimal orientation of the cup in terms of impingement could be quite different from the optimal orientation of the cup for edge-loading. In fact, in most cases, the optimal orientation of the cup in terms of one criterion gives a negative value for the other one. In order to take both impingement and edge-loading into account, the minimum value of AID and AED are obtained at each cup orientation and presented in the third plot of each motion. Positive values in this plot indicate that the cup orientation is free of both impingement and edge-loading.

One can use Fig. 3.12 to evaluate the effect of cup orientation on AID and AED for the corresponding daily activity. However, it is desirable to do the same analysis for a combination of different daily activities to make sure the selected cup orientation is suitable for all. To achieve this, the daily activities are merged into a single complex motion by MoCap data concatenation and the same plots are obtained and shown in Fig. 3.13. Using this figure, one can select a cup orientation considering the limitations imposed by all three

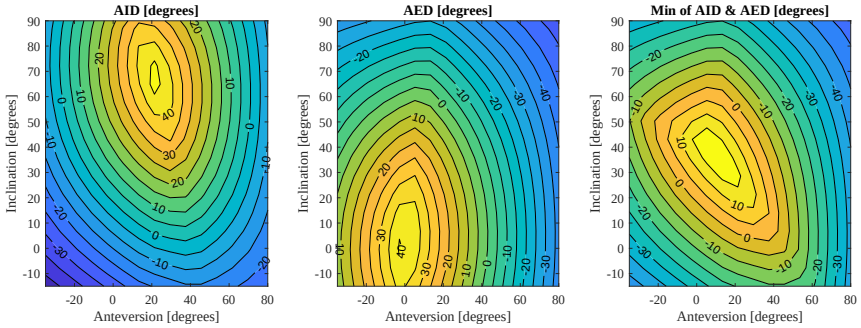

(a) sit-to-stand.

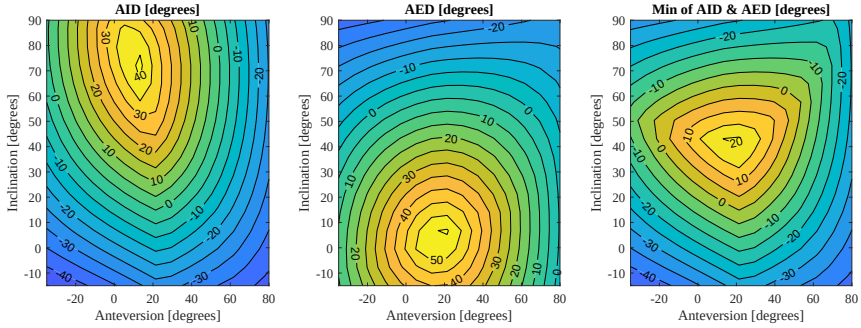

(b) walking

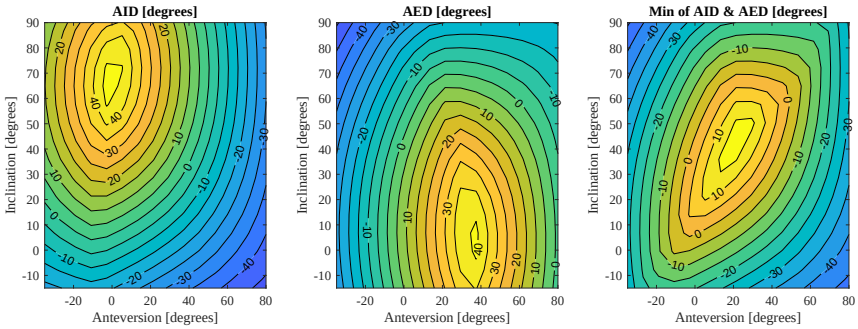

(c) picking an object from the ground.

Figure 3.12: The value of AID and AED during three different daily activities. Starting from the left hand side, the first and the second contour plots respectively depict the value of angular impingement and the angular edge-loading distance as a function of cup alignment angles. The third plot shows the minimum value of AID and AED.

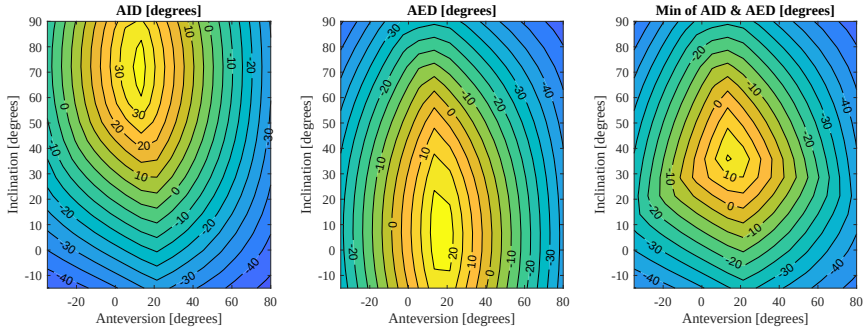

Figure 3.13: The value of AID and AED for the combination of all three daily activities obtained by concatenating the MoCap data for the three motions. Starting from the left hand side, the first and the second contour plots respectively depict the value of angular impingement and the angular edge-loading distance as a function of cup alignment angles. The third plot shows the minimum value of AID and AED.

movements.

3.6.2 Optimal cup orientation

The optimal orientation of the cup using the three optimal cost-functions described in Section 3.5 are given in Table 3.2. For optimization #2 and #3 the minimum acceptable value for AED and AID were chosen as $\tilde{\theta}_{AID} = \tilde{\theta}_{AED} = 10°$. Referring to the results for optimization #1 in Table 3.2, as it is expected from the nature of the cost-function, for the optimized cup orientation, the value of AID and AED are equal. In other words, one can interpret that optimization #1 allocates equal weights to the implant impingement and edge-loading. The optimal value obtained from optimization #1 can be graphically identified by locating the maximum value on the third column plots of Figs. 3.12 and 3.13.

Comparing the results of optimization #2 with optimization #1, one can observe that the second optimization achieves higher AID at the expense of lower AED. Also, the optimal value of inclination angle is higher in the second optimization, which complements the results obtained in Figs. 3.12 and 3.13, illustrating that high values of AID have larger

Table 3.1: Implant parameters used in the simulation studies [96].

Parameter	Value
Head diameter (d_{Head})	28 mm
Neck diameter (d_{Neck})	12 mm
Cup opening (α)	180°
Neck-shaft angle	130°
Stem flexion	3°
Stem adduction	5°

inclination angles compared to the high values of AED. The opposite argument made for optimization #2 can be made for optimization #3: in this optimization, more emphasis is on reducing the risk of edge-loading and the inclination angle is lower compared to optimization #1, which results in a better support for the hip contact force. Clearly, one could change the relative importance of impingement and edge-loading by readjusting the value of $\tilde{\theta}_{AED}$ and $\tilde{\theta}_{AID}$.

The optimal orientation of the cup obtained from the three optimizations for the combined daily activities are shown in Fig. 3.14. The result of the first optimization (▲) is well within the Lewinnek safe zone, while the orientations from the second (●) and third optimization (■) are on the edge of the safe zone. Therefore, the Lewinnek safe zone may not always be optimal, or even safe [90, 91, 174, 177, 178].

At this point, two natural questions that arise are: "which optimization will yield the best result?" and "what is the best value of $\tilde{\theta}_{AED}$ and $\tilde{\theta}_{AID}$ for the second and third optimization?". We believe the answer to these questions depend on the surgeon's assessment off the patient's condition. For example, if the surgeon recognizes a higher possibility of impingement compared to edge-loading for a specific patient, optimization #2 can be used with small values of $\tilde{\theta}_{AED}$ to create a higher margin of safety for impingement. On the other hand, if the surgeon is equally concerned about the risk of impingement and edge-loading,

Table 3.2: Optimal orientation of the cup for different daily activities.

Optimization	Daily Activity	Optimal Cup Orientation (deg)		Distance to Impingement & Edge Loading (deg)	
		Anteversion	Inclination	AID	AED
Opt #1	Sit-to-stand	7	39	19	19
	Walking	19	42	22	22
	Bending over	25	48	20	20
	Combined	16	36	18	18
Opt #2	Sit-to-stand	16	75	31	10
	Walking	19	51	33	10
	Bending over	13	48	30	10
	Combined	13	48	27	10
Opt #3	Sit-to-stand	4	30	10	31
	Walking	19	27	10	37
	Bending over	28	36	10	30
	Combined	16	30	10	23

optimization #1 might be the most appropriate method. Hence, the results obtained in this section are only examples of what this method can produce, and the obtained values should not be considered as strict guidelines.

3.6.3 Effect of pelvis tilt on the optimal cup orientation

In this section, the effect of pelvic tilt (PT) on the optimal orientation of the cup is studied. The PT of the daily activities used in the previous sections were artificially changed by an angle ranging from -20° to 20° (without changing the orientation of the other body parts) and the optimal orientation of the cup was recalculated for the combined daily activities. The optimal orientation of the cup for different PTs is depicted in Fig. 3.15. Posterior and

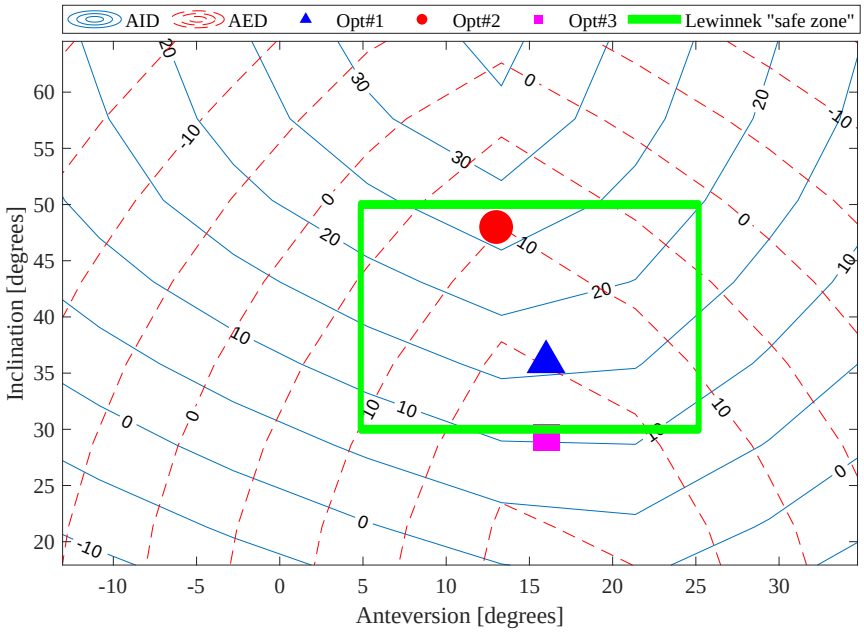

Figure 3.14: Optimal cup orientation considering all three daily activities.

anterior PTs are respectively shown by negative and positive values. As it is evident from Fig. 3.15, optimal anteversion and inclination angles become larger as the pelvis is tilted forward, and vice versa. From Fig. 3.15, the average increase of optimal anteversion and inclination angle for every 1 degree increase in pelvic tilt is about 0.72 and 0.19 degrees respectively. These values are inline with the results obtained in other studies, as shown in Table 3.3.

It is worth noting that the optimal cup orientations for large PT angles are not covered by the Lewinnek safe zone. This indicates the importance of considering the subject-specific pelvic tilt during the pre-operative planning stage of THA, an issue identified and reported in other studies [90, 91, 174, 177, 178].

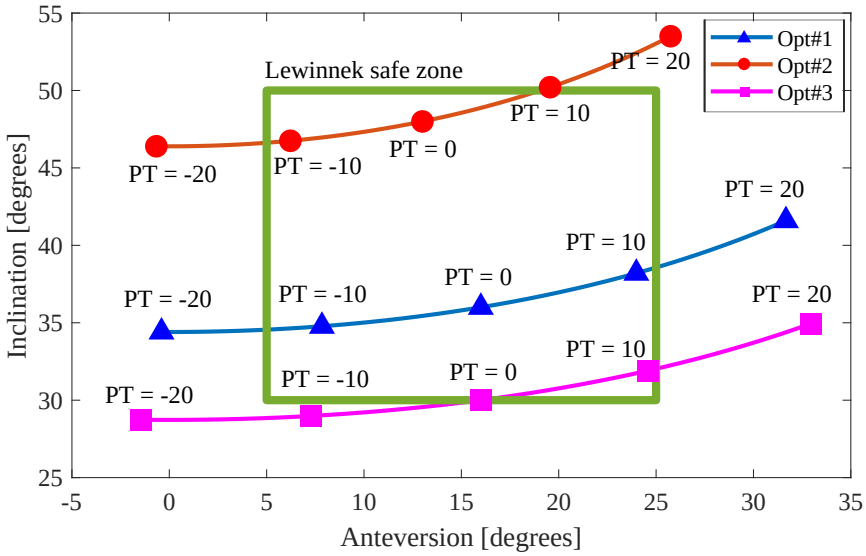

Figure 3.15: Optimal cup orientation for different pelvic tilts (PTs). Positive PT = Anterior PT. Negative PT = Posterior PT.

3.7 Conclusion

This chapter introduced a patient-specific approach for determining the optimal orientation of the acetabular cup for THA, based on an inverse dynamic model. By utilizing motion data obtained from the patient, the method allows for pre-operative planning to assess the potential for impingement and edge-loading with various cup orientations. Moreover, incorporating this method into a surgical navigation system could enable surgeons to adjust the cup orientation based on the actual stem alignment during the surgery. Compared to other methods in the literature, the proposed approach offers the following key advantages:

1. **It requires fewer clinical measurements**: By estimating the ground reaction forces, the need for force-plate measurements is eliminated, which makes this method easier to use and more affordable. Especially, integrating this method with a low-cost motion capture system [180, 181], this method can be implemented in clinical routines.

Table 3.3: Change in the optimal cup alignment for every 1° change in the pelvic tilt.

	Anteversion	Inclination
Current study	0.72°	0.19°
Hsu et al. [174]	0.54°	0.29°
Lembeck et al. [91]	0.7°	unknown
Babisch et al. [90]	0.8°	0.3°
Thelen el al. [179]	0.53°	unkhown

2. **Low computational complexity**: FEA simulations [93] are time-consuming and complex. By contrast, the method proposed here is fast because it is based on symbolic dynamic equations, which makes it suitable for both pre-operative and intra-operative applications. The average CPU time for 50 simulations of optimal cup orientation was 3.7s on a desktop PC with Intel Core i7 processor.

3. **Both impingement and edge-loading are taken into account**: As shown in Section 3.6.2, the optimal cup orientation in terms of impingement was often different from the optimal orientation in terms of edge-loading. Therefore, it is important to consider both criteria simultaneously when determining the optimal cup orientation. By taking both criteria into account, this method can minimize the risk of impingement and edge-loading simultaneously.

While the method proposed in this chapter provides a computationally efficient way for calculating optimum patient-specific cup alignment based on implant impingement and edge-loading it suffers from three primary limitations. Firstly, collecting motion capture data is a challenging task that is generally not conducted before THA surgeries. Secondly, the patient's motion patterns may vary before and after the procedure due to preoperative hip pain [182]. Lastly, the static optimization technique employed in this chapter to estimate the muscle forces disregards the dynamics of muscle contraction and activation, which could lead to unrealistic outcomes. The subsequent chapter covers an alternative

approach to tackle these issues, which involves a predictive optimal control method.

Chapter 4

Predictive Simulation Approach for Acetabular Cup Orientation Optimization Following THA

4.1 Introduction

Chapter 3 showcased how motion capture data from a patient can be utilized to compute the optimal alignment of the acetabular cup implant, thereby reducing the likelihood of impingement and edge-loading. Nevertheless, that method has two main drawbacks. Firstly, acquiring motion capture data is a complicated task, and it is not typically conducted before THA surgeries. Secondly, the patient's motion may vary before and after the surgery due to the likelihood of hip pain before the procedure. To tackle these issues, predictive dynamic simulations can be used instead. By employing the general assumption that human movement is in some sense "optimal" for a given situation, motions can be predicted using optimal control methods. In this chapter, we utilize the direct collocation-based trajectory optimization approach to produce predictive simulations for motions such as sit-to-stand and lifting objects from the ground. These simulations are then used to

calculate the optimal acetabular cup orientation for different "what-if" scenarios.

4.2 Modified Musculoskeletal Model

Chapter 3 introduced a 3D musculoskeletal model in which each joint was represented as a simple torque-driven joint with no contraction dynamics. To determine the hip contact force, the hip torque calculated through the inverse dynamic method was converted to muscle forces using the static optimization approach that overlooked the dynamics of muscle contraction and activation. In this chapter, a more biofidelic approach was adopted to simulate the actuation of the joints.

For the joints where contact forces are not necessary, i.e. all joints except for the hip joint, a set of agonist-antagonist muscle torque generators (MTGs) is employed. The function of an MTG is to provide a joint torque that imitates the behavior of muscles that cross a specific joint. The MTG model developed by Millard et al. [183] was utilized, which expresses a single MTG torque, τ^M, as:

$$\tau^M\left(a,\theta,\dot{\theta}\right) = \tau_0^M\left(a\tau^A\left(\theta\right)\tau^V\left(\dot{\theta}\right) + \tau^P\left(\theta\right)\right) \tag{4.1}$$

The variables a, θ, and $\dot{\theta}$ represent muscle activation, joint angle, and angular speed, respectively. The maximum isometric torque is denoted by τ_0^M, while τ^A, τ^V, and τ^P are the normalized curves for active-torque-angle, active-torque-angular-speed, and passive-torque-angle of the muscle, respectively. These curves, which are dependent on the muscle's geometric properties and differ from muscle to muscle, are commonly referred to as "characteristic curves" which were obtained from [183–185].

Meanwhile, for the hip joint, since a good estimation of contact forces was needed, each muscle unit described in Section 3.3.3 was modeled as a Hill-type muscle [186] to calculate the muscle forces, F^M:

$$F^M = F_0^M\left(a f_l\left(\tilde{l}\right) f_v\left(\tilde{\dot{l}}\right) + f_p\left(\tilde{l}\right)\right)\cos\alpha_P \tag{4.2}$$

where the maximum isometric muscle force is denoted by F_0^M, and α_P represents the pennation angle. The functions f_l, f_v, and f_p are associated with the normalized curves for active force-length, active force-speed, and passive force-length, respectively. Additionally, a represents muscle activation, while $\tilde{l}$ and $\tilde{\dot{l}}$ correspond to the normalized muscle fiber length and velocity, respectively.

To speed up simulations, the model was simplified by assuming that the feet are stationary with respect to the ground and the movements discussed in this chapter are symmetrical with respect to the sagittal plane. As a result, mediolateral symmetry was imposed on the model described in Section 3.3.1. This assumption enabled us to derive the normalized length of each muscle based on the hip joint flexion/extension angle. Therefore, Eq. (4.2) can be restated as follows:

$$F^M = F_0^M \left(a f_l \left(\mathcal{L} \left(\theta_{hip} \right) \right) f_v \left(\frac{d\mathcal{L} \left(\theta_{hip} \right)}{d\theta_{hip}} \dot{\theta}_{hip} \right) + f_p \left(\mathcal{L} \left(\theta_{hip} \right) \right) \right) \cos \alpha \tag{4.3}$$

where $\mathcal{L}(\theta)$ is the function that defines the normalized muscle length as a function of the hip joint angle. Similarly, one can derive the muscle moment arm of each muscle about the center of the hip joint as a function of the hip joint angle, and multiply it with Eq. (4.3). This enables us to map the muscle force to the torque generated by each muscle about the center of the hip joint, as follows:

$$\tau_{hip}^M = F_0^M \left(a f_l \left(\mathcal{L} \left(\theta_{hip} \right) \right) f_v \left(\mathcal{L}' \left(\theta_{hip} \right) \dot{\theta}_{hip} \right) + f_p \left(\mathcal{L} \left(\theta_{hip} \right) \right) \right) \hbar \left(\theta_{hip} \right) \cos \alpha \tag{4.4}$$

where the muscle moment arm about the hip joint center as a function of the hip joint angle is represented by $\hbar(\theta)$, and the torque generated by the muscle at the hip joint is denoted as τ_{hip}^M. To expedite the musculoskeletal model, we can pre-calculate and store $\mathcal{L}(\theta)$, $\mathcal{L}'(\theta_{hip})$, and $\hbar(\theta)$ offline by transforming them into cubic spline functions. This allows us to avoid calculating muscle geometry at each simulation instance and enhances the speed of the model. It is worth mentioning that, unlike the MTG, this method considers the unique impact of each muscle on the joint's total torque. This feature allows us to compute the muscle forcesc which is crucial for determining the hip contact force.

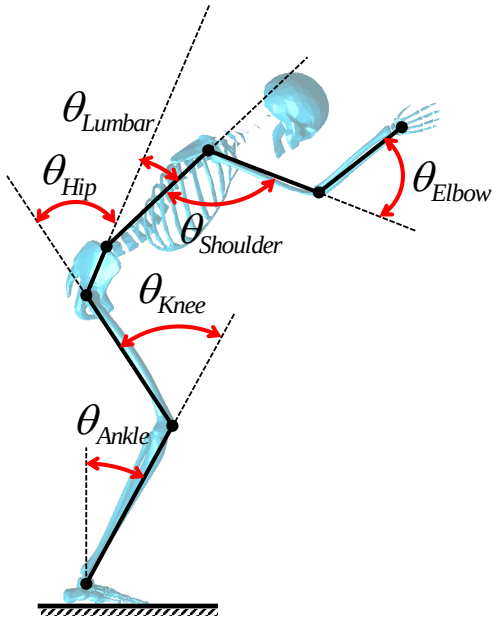

Figure 4.1: Definition of joint angles. All the joints are modeled as ideal revolute joints.

Hence, the dynamic model given in Eq. (3.1) can be rewritten in the following state-space form:

$$\dot{\mathbf{x}} = \mathbf{f}(\mathbf{x}, \mathbf{a}) \tag{4.5}$$

where the musculoskeletal model has 12 states represented by the state vector $\mathbf{x} = [\theta; \dot{\theta}]$, with 6 states corresponding to joint angles (see Fig. 4.1) and the remaining 6 states corresponding to joint velocities. Additionally, the control signals vector, $\mathbf{a}$, consists of 21 muscle activations (see Section 3.3.3) affecting the torque for hip joint flexion/extension as described in Eq. (4.4), and 5 pair of activations for MTGs that impact the ankle, knee, lumbar, shoulder, and elbow joints as detailed in Eq. (4.1).

4.2.1 Buttocks-chair Contact

According to literature [187], during sitting, the buttocks can transmit a force equivalent to 80% of the body weight. Additionally, approximately during the first third of a healthy

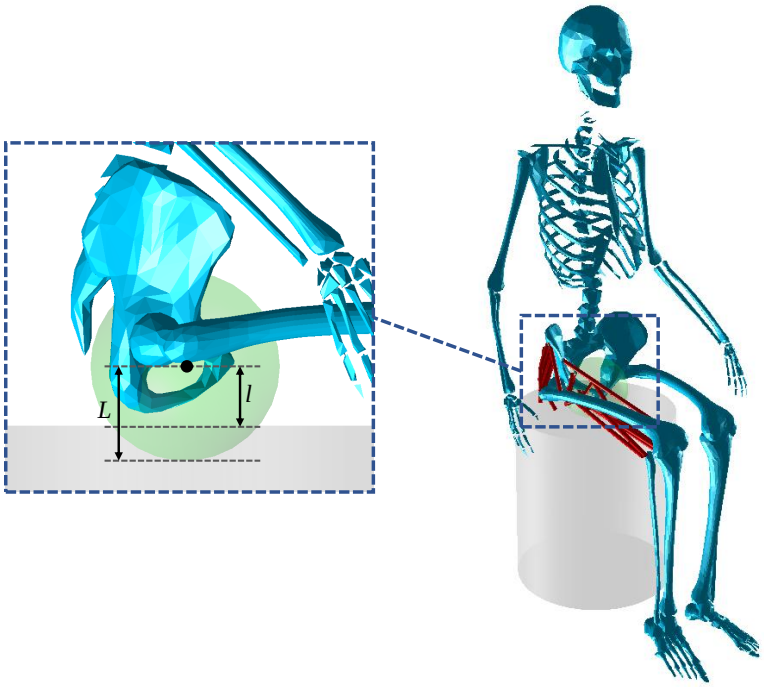

Figure 4.2: The buttocks model.

sit-to-stand movement, the buttocks maintain contact with the chair [188]. To accurately predict sit-to-stand movements, it has been shown that it is crucial to have a buttocks model that can effectively characterize this significant force that occurs while sitting [168]. For this study, we employed the buttocks model developed in [168], which utilized a Mooney-Rivlin model to represent the buttocks. The normal force exerted on the buttocks by the chair, denoted as F_{chair}, can be determined by the following expression:

$$F_{chair} = \begin{cases} \left(\eta_1 \left(1-\delta\right) - \eta_2\right)\left(1 - \frac{1}{(1-\delta)^3}\right) + cL\dot{\delta}\tanh\left(\left(\frac{\delta}{\delta_t}\right)^2\right) & \text{if} \quad \delta > 0 \\ 0 & \text{if} \quad \delta \leq 0 \end{cases} \tag{4.6}$$

$$\delta = \frac{L-l}{L} \tag{4.7}$$

where the material constants, η_1 and η_2, are assigned values of 213 N and 34 N, respectively. As shown in Fig. 4.2, l represents the thickness of the tissue and L represents the reference

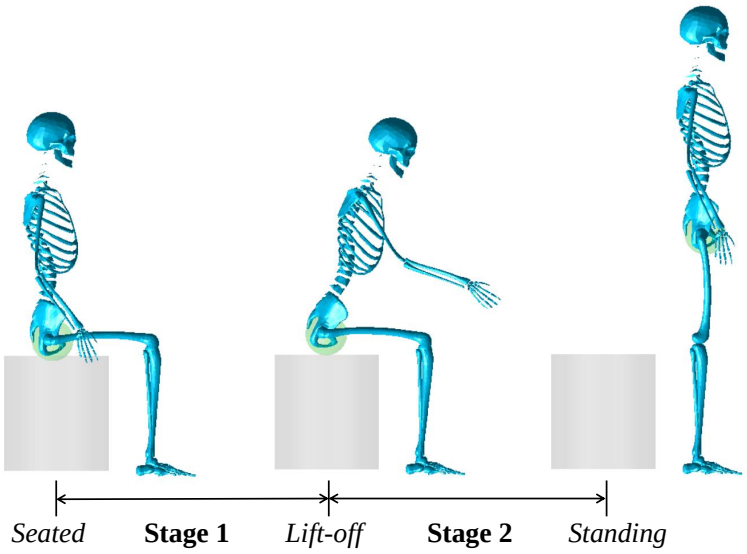

Figure 4.3: Two main stages of sit-to-stand motion.

tissue thickness. The damping coefficient, which has been set to 371 Ns/m, is denoted as c. Also, a value of 0.01 was assigned to δ_t, which represents the transition strain. This value was introduced to ensure the continuity of the piecewise function at $\delta = 0$. To determine the vertical component of the contact force, the buttocks-chair contact was subjected to the no-slip condition by assuming the static coefficient between the buttocks and chair is high enough to prevent any slipping. This assumption is supported by experimental measurements showing negligible changes in the ankle and knee joint angles before lift-off [189]. Further information regarding the specifics of this buttocks model can be located in reference [168].

4.3 Predictive Sit-to-Stand

Sit-to-stand motion refers to the movement of transitioning from a seated position to standing upright. It involves the activation of various muscles, including the quadriceps, glutes, and core, to generate enough force to lift the body up from a seated position. On

average, adults perform over 40 sit-to-stand motions per day, indicating the high frequency of this movement in their daily lives [43]. In this study, the sit-to-stand motion is split into two distinct stages, as illustrated in Fig. 4.3. The first stage ends with the loss of contact to the chair, which is referred to as lift-off. The formulation of the sit-to-stand motion prediction optimal control problem was as follows:

$$\min_{\mathbf{x},\mathbf{a}} \quad \sum_{i=1}^{2} \int_{t_{i-1}}^{t_i} J_i\left(\mathbf{x}(t), \mathbf{a}(t)\right) dt \tag{4.8}$$

subjected to:

$$\begin{aligned}
\text{Dynamic Model:} \quad & \dot{\mathbf{x}} = \mathbf{f}\left(\mathbf{x}, \mathbf{a}\right) \\
\text{Joint Angle Limit:} \quad & \theta_{\min} \leq \mathbf{x}[1:6] \leq \theta_{\max} \\
\text{Ground-foot Contact Location:} \quad & d_{\min} \leq d_{GF}\left(\dot{\mathbf{x}}, \mathbf{x}, \mathbf{a}\right) \leq d_{\max} \\
\text{Activation Limit:} \quad & 0 \leq \mathbf{a} \leq 1 \\
\text{Initial State:} \quad & \mathbf{x}(0) = \begin{bmatrix} \theta_0 & \dot{\theta}_0 \end{bmatrix}^T \\
\text{Final State:} \quad & \mathbf{x}(t_2) = \begin{bmatrix} \theta_f & \dot{\theta}_f \end{bmatrix}^T
\end{aligned} \tag{4.9}$$

where the cost-function of the ith stage is denoted as $J_i\left(\mathbf{x}, \mathbf{a}\right)$. The initial time is denoted as $t_0 = 0$, the time of lift-off is denoted as t_1, and the terminal time is denoted as t_2. By adjusting the cost-function, this optimization problem will be solved for various scenarios in the succeeding sections.

4.3.1 Sit-to-Stand Prediction of a Healthy Individual

To validate our model, we predict a healthy sit-to-stand motion and then compare the results to experimental data from [189,190]. We adjust the seat position to ensure that the initial pose of the model matches the experimental data, specifically by aligning the initial joint angles of the model in the seated position with the average joint angles observed in the experimental data. The cost-function for the first and second stages of the optimal

control problem, as presented in Eq. (4.8), were selected as follows:

$$J_1 = \|\mathbf{a}(t)\|^2 + \alpha \left(\frac{\dot{\theta}_{Ankle}(t)^2 + \dot{\theta}_{Knee}(t)^2}{\dot{\theta}^2_{Norm}} \right) + \gamma \left\| \frac{\dot{\theta}(t)}{\dot{\theta}_{Norm}} \right\|^2 \tag{4.10}$$

$$J_2 = \|\mathbf{a}(t)\|^2 + \beta \left\| \frac{\theta(t) - \theta_f}{\theta_{Norm}} \right\|^2 + \gamma \left\| \frac{\dot{\theta}(t)}{\dot{\theta}_{Norm}} \right\|^2 \tag{4.11}$$

The cost-function for the first stage penalizes a combination of effort, which is expressed as the sum of squared excitations, a^2, the movement of the ankle and knee joints, which is expressed as the sum of squared angular speed of the knee and ankle joints, and the angular speed of the joints. Penalizing the knee and ankle joints helps the model find an equilibrium posture in terms of buttocks-chair contact and avoid any bouncy movements on the chair before lift-off. After conducting several trials, we determined that the smallest value of α needed to stabilize the first stage of the sit-to-stand was about 1.7 $(\text{s/rad})^2$, which we used in our simulation. We did not observe any noticeable changes in the simulation's outcome for higher values of α. The angular speed of the joints was included as an additional cost because the predicted sit-to-stand motion was slightly faster than the average reported in the literature. To address this, an empirical approach was used to determine that setting $\gamma = 0.3$ $(\text{s/rad})^2$ resulted in a predicted sit-to-stand motion duration of 2.1 seconds, which closely aligns with the average duration observed in healthy adults [190].

For the second stage, the cost-function was designed to minimize effort and the duration of the motion by penalizing the difference between the joint angles and their corresponding final desired values. It's important to note that minimizing the effort for the second stage indirectly minimizes the duration of the movement since the full stance position is theoretically a stable posture, and remaining in the full stance does not require any effort. Therefore, taking too long to perform the sit-to-stand is not desirable in terms of the activation cost-function. Because of this, we did not observe any noticeable sensitivity in the optimization outcome in terms of the value of β. We set $\beta = (\pi/2)^{-2}$ $(1/\text{rad})^2$, which implies that the cost of a 90-degree difference between the joint angle and its desired final value is equal to the cost of a full muscle activation, equal to 1. Based on the same logic

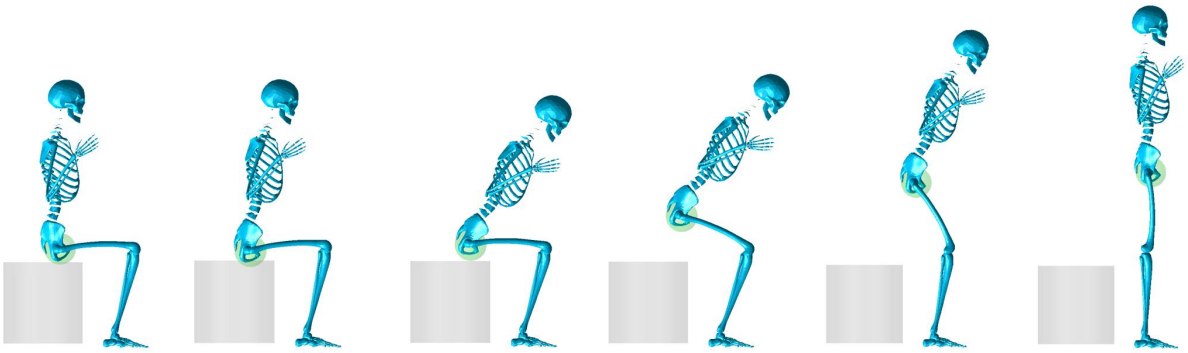

Figure 4.4: Predicted sit-to-stand movements captured at evenly-spaced intervals.

that taking too much time to complete the sit-to-stand and attain an equilibrium state would result in a higher cost, we set t_f to a sufficiently large value, $t_f = 6$, to avoid enforcing a specific time for reaching the full stance phase and stopped the simulation when the joint speeds became negligible in the second stage.

The optimization problem was solved using GPOPS-II [191], a Matlab toolbox for direct collocation optimal control. The predicted motion is shown in Fig. 4.4. It is worth mentioning that the participants' arms were folded across their chests during the data collection process of the experimental data used. As a result, in the predicted sit-to-stand movement presented in this section, the shoulder and elbow angles were adjusted to position the arms in close proximity to the chest, thus replicating the experimental conditions. This adjustment was made to ensure the accuracy and reliability of the simulation.

In Fig. 4.5, a comparison is made between the hip, knee, and lumbar joint angles obtained from the predicted simulation and the experimental data presented in [190]. The model-predicted values for the joint angles at the knee, hip, and lumbar show root mean square errors of 2.6°, 9.6°, and 7.2°, respectively, when compared to the mean value of the experimental data. The discrepancy between the predicted and experimental lumbar joint angle may arise from the fact that the spine was modeled as a solid body, whereas in reality, it is flexible. Specifically, the experimental data in [190] includes measurements taken from the thoracic spine, which exhibits notable motion that our model cannot replicate because

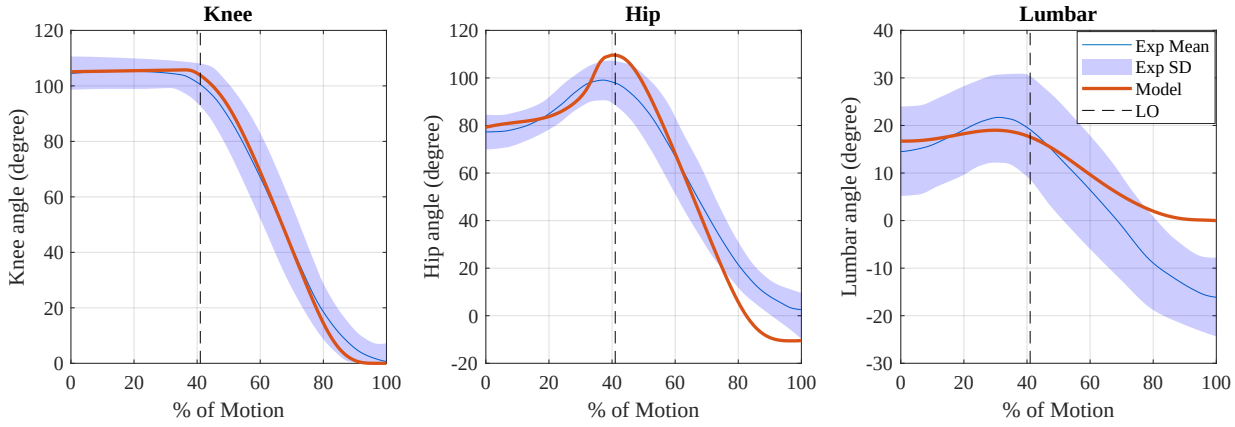

Figure 4.5: The model-predicted joint angle profiles during sit-to-stand movement compared to the experimental measurements conducted by Tully et al. [190]. The point of lift-off is denoted by LO.

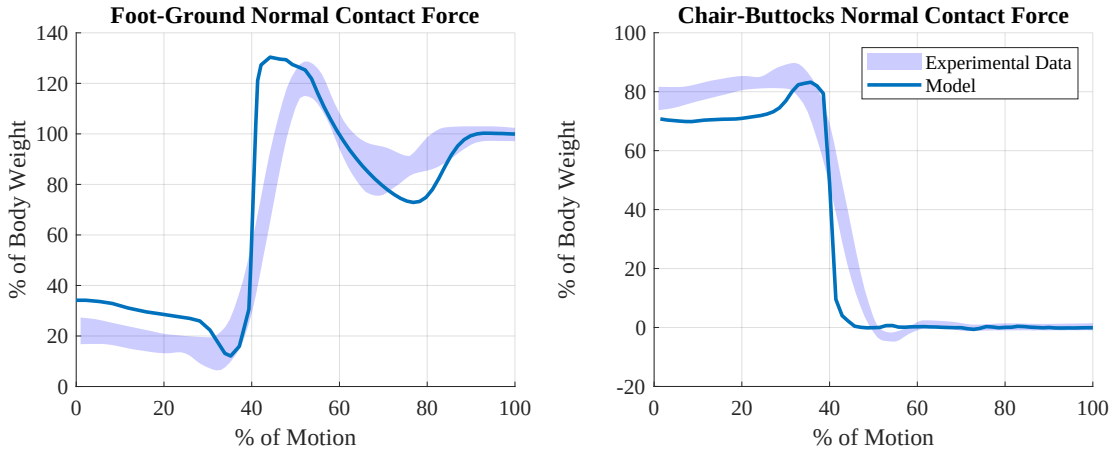

Figure 4.6: Comparison of the predicted foot-ground and chair-buttocks normal contact forces during sit-to-stand movement with the experimental measurements conducted by Norman-Gerum et al. [189].

it lacks a spine model. Furthermore, we notice a hip joint angle that becomes negative towards the end of motion. This behavior could be explained by the fact that leaning slightly backward aligns the center of mass with the joint lines, reducing the effort required.

Additionally, Figure 4.6 compares the normal contact force between the foot-ground and chair-buttocks, which is normalized to the body weight, obtained from the predicted simulation with experimental data from Norman-Gerum et al. [189]. Despite the fact that sit-to-stand motion patterns vary greatly among individuals, as evidenced by the standard deviation of the experimental data shown in Fig. 4.5, the predicted joint angles and contact forces follow the observed trends in the experimental data.

4.3.2 Sit-to-Stand Prediction Under Various Conditions

The ability to explore "what-if" scenarios and predict human movement under varying conditions is the key advantage of predictive simulations. In this section, the predictive model is utilized to estimate sit-to-stand motion under various conditions by modifying the optimal control problem employed for a healthy subject in the previous section. The effect of these conditions on the optimal alignment of the acetabular cup is subsequently examined. We have studied the impact of the following conditions on the motion pattern during sit-to-stand:

1. **Variations in chair height**: The literature suggests that chair height has a significant impact on the sit-to-stand motion pattern [192, 193]. Altering the initial joint angles of the predictive optimization problem can simulate the effect of various chair heights. Figure 4.7 displays the predicted sit-to-stand motion for chair heights 25% higher and lower than the original. Notably, the figure highlights that when using a low seat, the arms are utilized more to generate additional momentum during the lift-off phase, whereas in the case of a high chair, the movement of the arms is negligible. In addition, Fig. 4.8 depicts how various chair heights impact the hip joint angle, revealing an inverse relationship between chair height and the maximum value

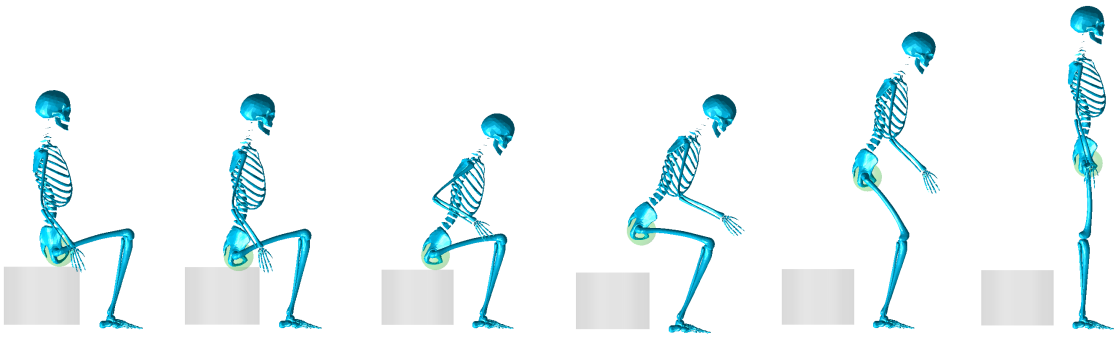

(a) low chair

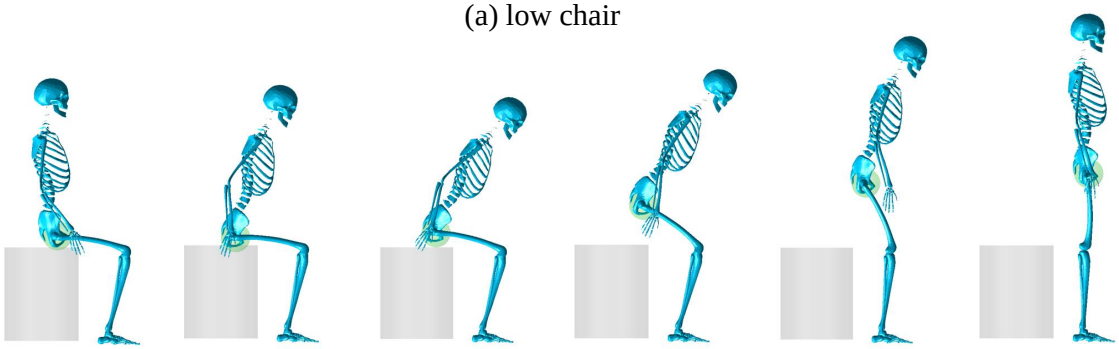

(b) High chair

Figure 4.7: The predicted sit-to-stand motion for high- and low-chairs.

of the hip joint angle during the lift-off phase. This finding is significant because excessive hip flexion can raise the possibility of hip implant impingement [194].

2. **Spinal fusion**: According to existing literature, individuals who have undergone lumbar spinal fusion surgery are more susceptible to hip dislocation [195]. It is important to acknowledge that this study did not model the spine and only used a single revolute joint to represent the lumbar joint. As a result, it is not possible to conduct a thorough assessment of spinopelvic mobility and its impacts, which is beyond the scope of this thesis [196]. Therefore, this study only evaluated a theoretical scenario where there is no spine mobility by setting the lumbar joint angle to zero during the motion. Figure 4.9 depicts the simulation outcomes, which compare the hip joint angles of an individual with a fused lumbar to that of a person

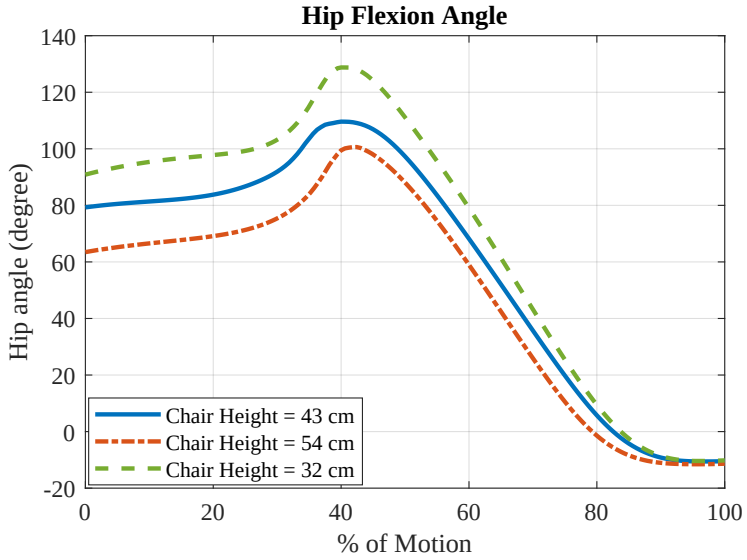

Figure 4.8: Hip flexion angle for different chair heights. The hip flexion angle is higher in lower seats.

with a flexible lumbar. The figure illustrates that restricted spinal mobility results in greater hip flexion during sit-to-stand movements, elevating the risk of dislocation.

3. **Hip and knee pain**: Previous research has demonstrated that knee and hip osteoarthritis can impact how people perform sit-to-stand movements [197]. This study aimed to predict the movements of people with knee and hip osteoarthritis pain by integrating the hip and knee joint reaction forces into the cost-function of the optimal control problem. The fundamental premise behind this approach was that a higher joint force is correlated to higher joint pain. Specifically, for people with hip joint osteoarthritis, the cost-function of the second stage of sit-to-stand was modified as follows:

$$J_2 = \|\mathbf{a}(t)\|^2 + (\pi/2)^{-2}\|\theta(t) - \theta_f\|^2 + 0.3\left\|\dot{\theta}(t)\right\|^2 + 0.01\|\mathbf{F}_{Hip}\|^2 \tag{4.12}$$

where the final component imposes an additional cost on the force exerted on the hip joint. The coefficient assigned to this component, set at 0.01 ($1/\mathrm{N}^2$), implies that a 10 N hip reaction force corresponds to a complete muscle activation.

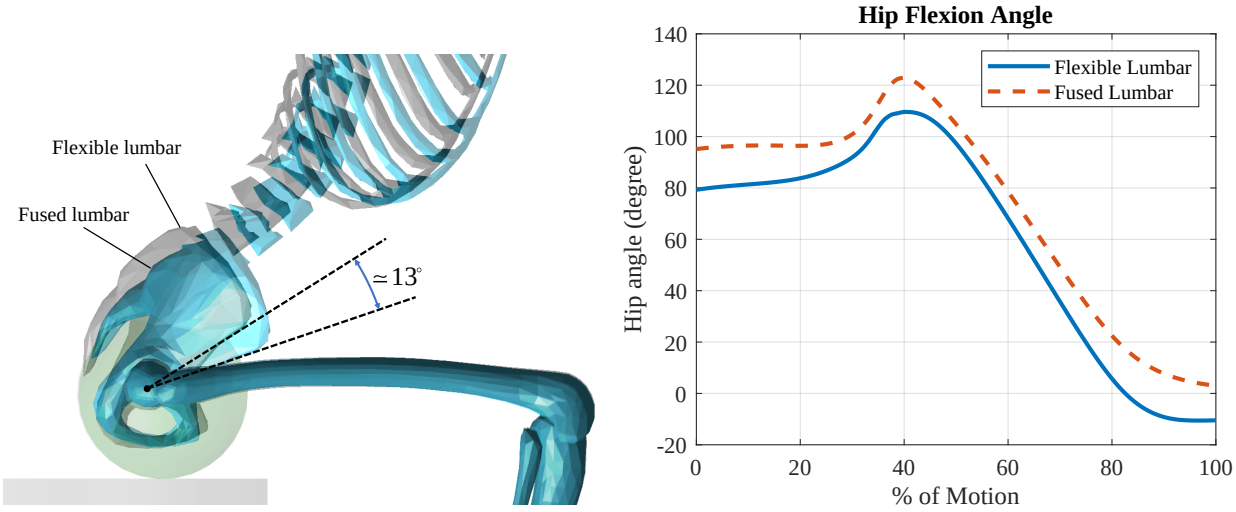

(a) Hip angle at the lift-off phase.

(b) Hip flexion angle throughout the motion for flexible and fused lumbar joint.

Figure 4.9: Effect of lumbar fusion on the hip flexion angle during sit-to-stand motion.

For those with knee joint osteoarthritis, as the current model did not consider the muscles surrounding the knee joint, a combination of the knee contact force (obtained from the force equilibrium equation at the knee joint) and the knee actuation torque (obtained from the MTG at the knee joint) was used to penalize the cost-function. The cost-function was modified as follows:

$$J_2 = \|\mathbf{a}(t)\|^2 + (\pi/2)^{-2}\|\theta(t) - \theta_f\|^2 + 0.3\|\dot{\theta}(t)\|^2 + 0.1\left(\|\mathbf{F}_{Knee}\|^2 + \left(\frac{\tau_{knee}}{0.03}\right)^2\right) \quad (4.13)$$

The value 0.03 in this equation is expressed in meters. Figure 4.10 illustrates the predicted movements of sit-to-stand when experiencing pain in the hip and knee joints. Additionally, Fig. 4.11 displays the hip joint flexion angle for two scenarios. These figures demonstrate that reducing stress in the knee and hip joints results in two distinct sit-to-stand movement patterns. Based on the results, to minimize stress in the knee joint, it is preferable to lean forward and overextend the upper body. Conversely, to reduce stress in the hip joint, it is preferable to maintain an

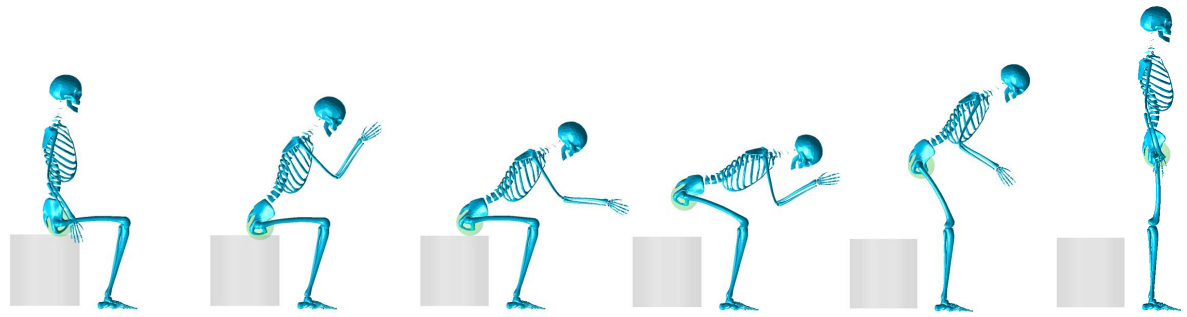

(a) Individual with knee pain

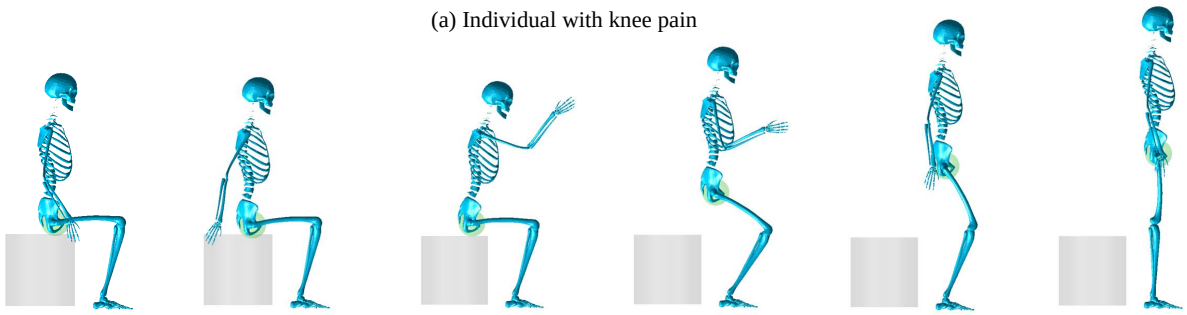

(b) Individual with hip pain

Figure 4.10: The predicted sit-to-stand motion for subjects with hip and knee pain.

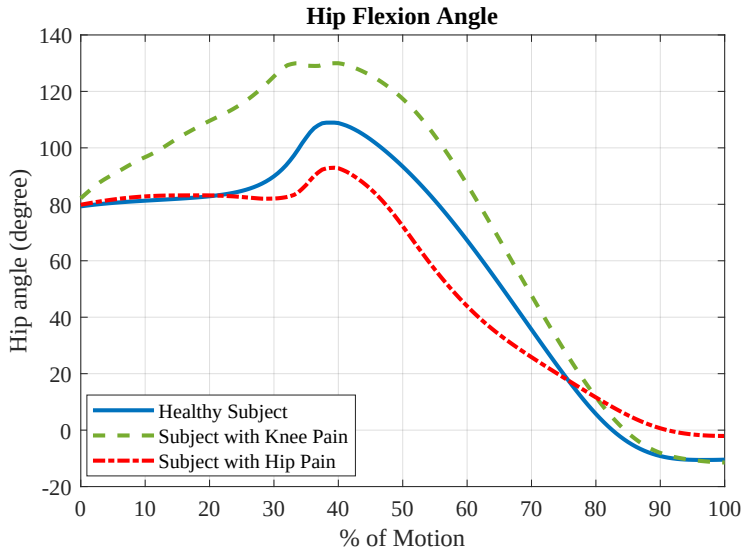

Figure 4.11: Hip flexion angle for subjects with hip and knee pain.

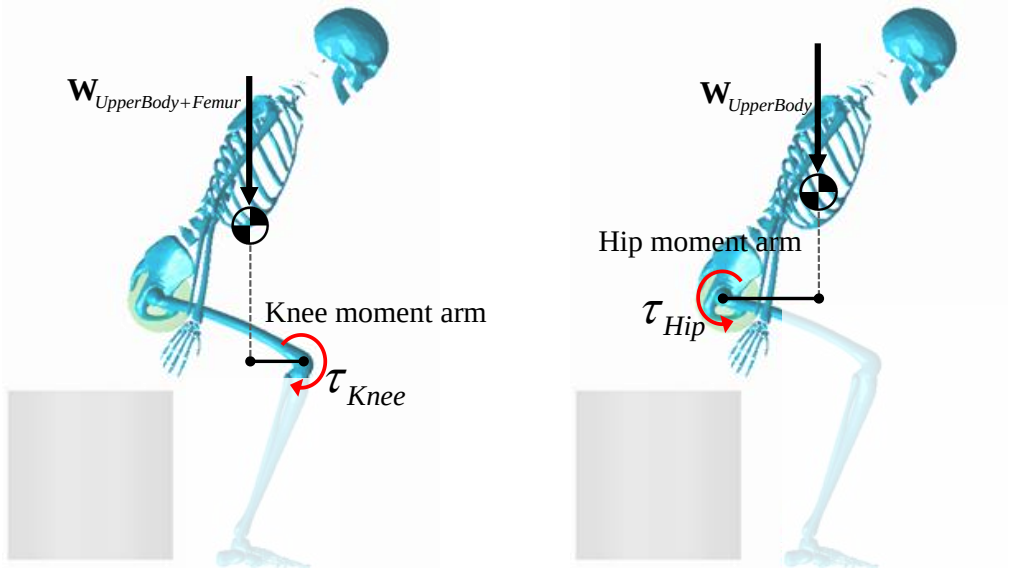

Figure 4.12: When the center of mass of the upper body moves over the knee joint, the moment arm of the knee joint decreases, while the moment arm of the hip joint increases.

upright position with minimal trunk flexion, which was accomplished by creating a forward moment in the arms before lift-off. This outcome is supported by the static equilibrium analysis shown in Fig. 4.12. By shifting the center of mass of the upper body over the knee joint by leaning forward, the knee moment arm becomes smaller, resulting in lower knee joint torque. These findings are consistent with the results of a previous experiment on patients with advanced knee osteoarthritis [198]. On the other hand, keeping the center of mass of the upper body over the hip joint through an upright position makes the hip moment arm smaller, resulting in lower hip joint torque. As a result, individuals with knee osteoarthritis may have greater hip flexion during sit-to-stand, which may increase the risk of hip dislocation, as seen in Fig. 4.11. Conversely, individuals with hip joint pain may exhibit lower hip flexion angles than healthy subjects, which could be advantageous in terms of reducing the risk of hip joint impingement.

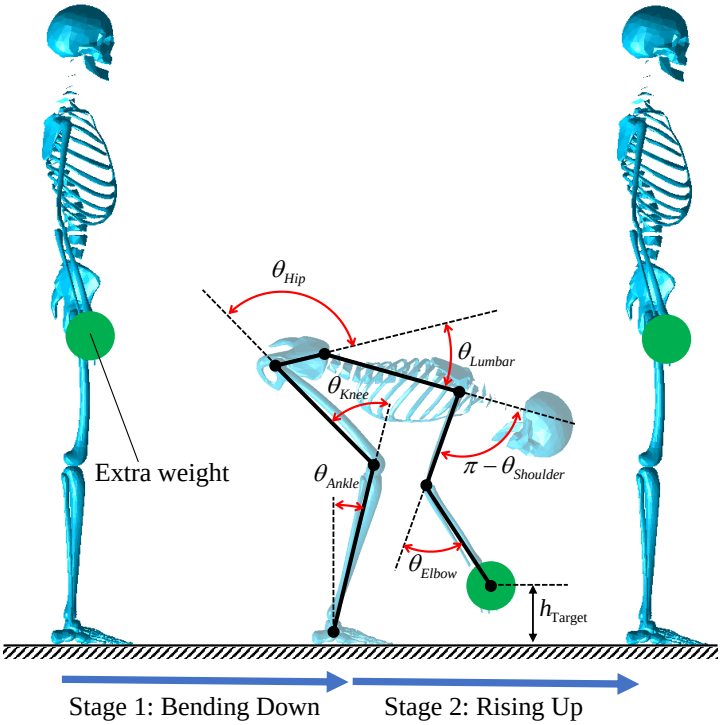

Figure 4.13: Stooping/lifting movement.

4.4 Predictive Stooping Down/Lifting Movement

Stooping down refers to the act of bending forward at the waist and lowering one's upper body towards the ground or a lower surface. It is a movement that involves the flexion of the spine and the hip joints, and it is often used in activities such as picking up objects from the ground, tying shoes, or performing exercises such as deadlift [199]. Due to the high degree of hip flexion involved, stooping down is deemed a risky movement for hip dislocation [53]. Thus, it is critical to take this motion into account when aiming for the optimal alignment of the acetabular cup.

Fig. 4.13 illustrates how the stooping movement was divided into two phases: bending down and rising up. To simplify the analysis, we assumed that the subject held weights (5 Kg per hand) during both stages, which eliminated the need to include the gripping

phase in our simulations. We formulated the optimal control problem for a predictive stooping movement in a similar manner to the optimal control problem defined for sit-to-stand motion, as specified in Eq. (4.8) and (4.9). However, we added a path-constraint to ensure that the hands reach a target height, h_{Target}, from the ground in the middle of the motion, simulating a pick-up movement. This constraint was implemented as follows:

$$\sum_{j=1}^{6} l_i \cos\left(\sum_{k=1}^{j} \beta_k\right) = h_{\text{Target}} \tag{4.14}$$

where

$$\begin{aligned} &\beta_1 = \theta_{Ankle}(t_1); \quad \beta_2 = -\theta_{Knee}(t_1); \quad \beta_3 = \theta_{Hip}(t_1); \\ &\beta_4 = \theta_{Lumbar}(t_1); \quad \beta_5 = \pi - \theta_{Shoulder}(t_1); \quad \beta_6 = -\theta_{Elbow}(t_1). \end{aligned} \tag{4.15}$$

where the length of the ith body segment, which begins at the tibia and extends up to the arm, is denoted as l_i (see Fig. 4.13). We assumed that the subject's foot placement was optimal before initiating the stooping motion, which is why we didn't impose a constraint on the horizontal component of the target point.

Similar to sit-to-stand predictive simulations, the stooping movement was predicted for subjects with varying conditions, including healthy subjects, those with lumbar fusion, and those with hip or knee pain. Figure 4.14 displays the predicted movements for healthy individuals and those with spinal fusion, with the individuals with spinal fusion exhibiting greater hip flexion, as expected. In Fig. 4.15, joint angle profiles throughout the movement for the knee, hip, and lumbar joint are compared for healthy individuals and those with spinal fusion, highlighting the higher hip flexion in the latter group. The results for individuals with hip and knee pain were very similar to those of healthy individuals, unlike the sit-to-stand motion, so they are not included in the results presented here.

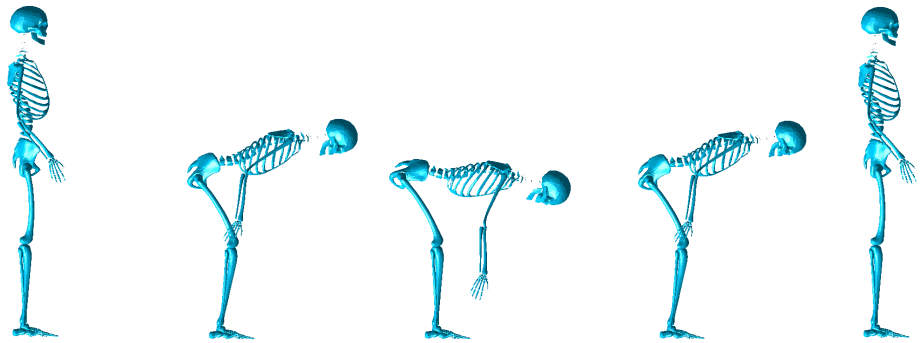

(a) Flexible lumbar joint

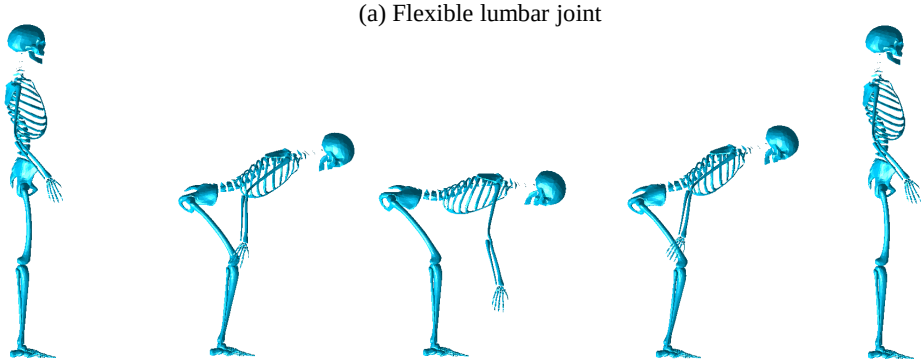

(b) Fused lumbar joint

Figure 4.14: Predicted stooping down movement for subject with (a) flexible and (b) fused spine.

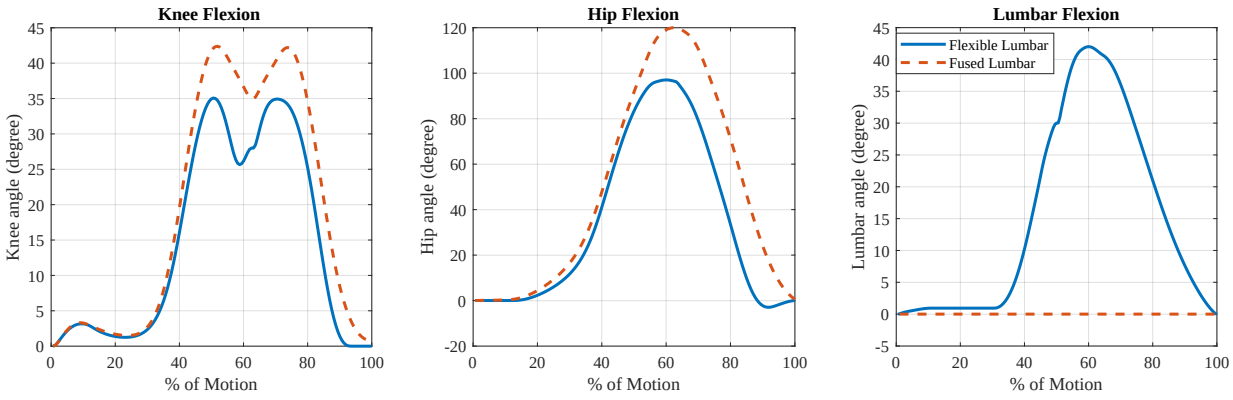

Figure 4.15: The model-predicted joint angle profiles during stooping movement for a healthy flexible spine and a fused spine.

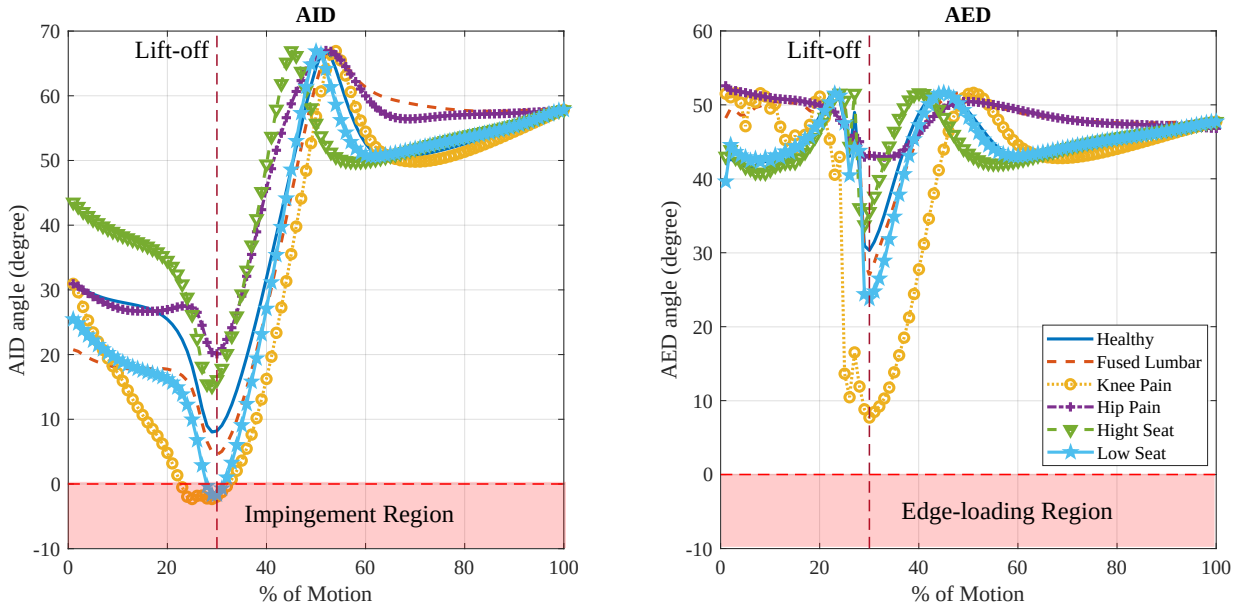

Figure 4.16: The AID and AED angles for predicted sit-to-stand movements with different conditions, for radiographic anteversion and inclination respectively equal to 15° and 40°.

4.5 Optimal Acetabular Cup Orientation based on Predictive Simulations

Figures 4.16 and 4.17 display the AID and AED values (defined in Section 3.4) for cup orientation set at the center of the Lewinnek safe zone (Anteversion = 15°, Inclination = 40°) for predicted sit-to-stand and stooping down movements under various conditions. The following observations can be drawn from the figures:

- The riskiest moment for hip dislocation occurs during lift-off when both the AID and AED values reach their lowest values. This is because, as noted in the previous section, the hip flexion angle is highest during the lift-off phase.
- Comparison of the AID and AED values of patients with spinal fusion to those of healthy individuals in the predictive simulations confirms that spinal fusion patients

are at a higher risk of dislocation during sit-to-stand and stooping movements, as widely known [200].

- Sit-to-stand from a high chair is safer than from a low chair in terms of distance from impingement and edge-loading. This finding aligns with the common recommendation for patients after total hip arthroplasty to use a high chair and raised toilet seats to minimize the risk of dislocation [201].

- Figure 4.16 also shows that changes in the sit-to-stand movement pattern due to knee pain can be even more catastrophic than the well-recognized risky case of spinal fusion. However, little has been reported regarding the association between knee injuries and hip dislocation in patients following THA [202–204]. This holds significance because, while spinal stiffness can be detected by examining medical images taken from patients during sitting and standing poses in pre-operative routine [205], knee pain is usually not studied or taken into account in typical pre-operative planning.

- Based on Fig. 4.16, unlike individuals with knee pain, those with hip pain alter their sit-to-stand motion pattern in a manner that reduces the risk of dislocation during this activity. Therefore, the motion capture-based approach described in Chapter 3 may not always yield the ideal cup orientation because the patient's movement pattern prior to THA may be more cautious than post-operation. Consequently, cup orientation determined from recorded movements prior to surgery may not be optimal or even safe after the surgery.

Using the same approach as in Section 3.6.2, we determined the optimal orientation of the acetabular cup by analyzing predicted movements for various conditions. We employed the optimization criteria outlined in Section 3.5, specifically optimization #1, which assigns equal weights to distances from impingement and edge-loading. The optimal cup orientation is presented in Table 4.1. Our findings reveal that higher anteversion and inclination angles are optimal for conditions that elicit greater hip flexions, such as lumbar fusion or knee pain. This aligns with the results we observed in Fig. 3.15, which showed

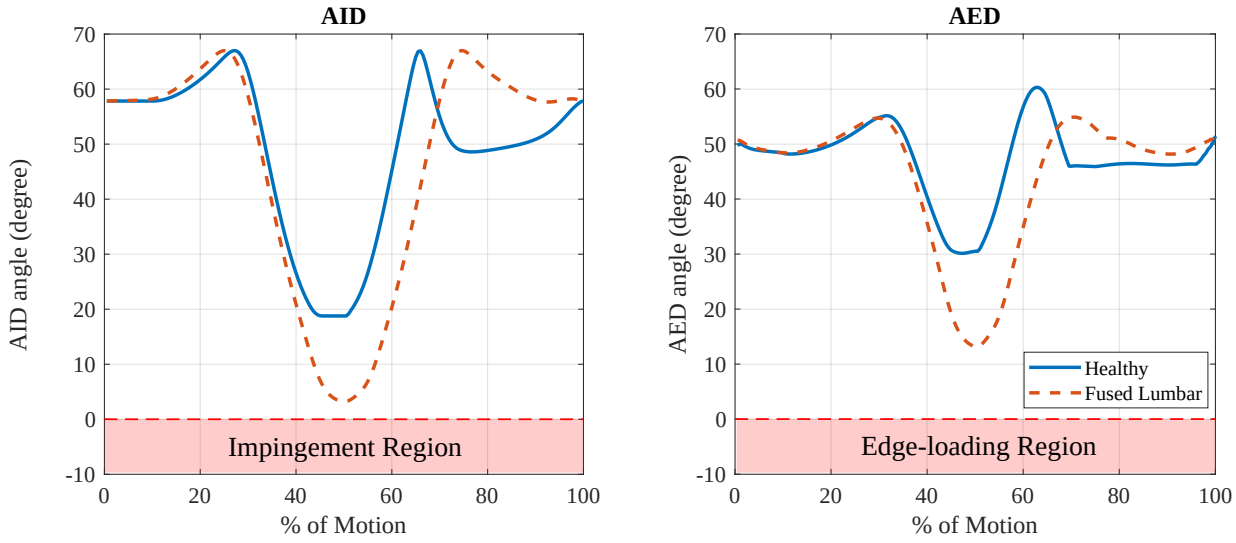

Figure 4.17: The AID and AED angles for predicted stooping movements with different conditions, for radiographic anteversion and inclination respectively equal to 15° and 40°.

a direct correlation between pelvic tilt and the optimal anteversion and inclination angles. Additionally, subjects with knee pain had a lower margin of safety, as evidenced by the minimum AID and AED angles. This phenomenon may be attributed to the fact that knee pain only results in heightened hip flexions during particular movements, such as sit-to-stand, wherein leaning forward reduces stress on the knee joint, but not during other movements like stooping down. Therefore, individuals experiencing knee pain are anticipated to have a broader range of hip flexions, requiring more extensive coverage from the acetabular cup, unlike in the case of lumbar fusion where higher hip flexions are consistently generated.

4.6 Conclusion

In this chapter, the discussed approach of predictive optimal control overcomes the main limitation of the inverse dynamic method presented in the previous chapter, which relied on

Table 4.1: Optimal orientation of the cup based on the predictive simulations under different conditions.

Condition	Movement	Optimal Cup Alignment (degree)		Min AID & AED (degree)
		Ant	Inc	
Healthy	Sit-to-Stand	9	43	19
	Stooping	22	49	24
	Combined	12	42	18
Lumbar Fusion	Sit-to-Stand	18	44	19
	Stooping	24	51	18
	Combined	21	46	16
Knee Pain	Sit-to-Stand	19	46	17
	Stooping	22	49	24
	Combined	20	48	14
Hip Pain	Sit-to-Stand	7	41	27
	Stooping	22	49	24
	Combined	9	40	22

motion capture data. This predictive approach allowed us to explore "what-if" scenarios to study the impact of various conditions, such as lumbar fusion and joint pain, on movement and subsequent optimal alignment of the acetabular cup. For instance, it was found that changes in sit-to-stand movement patterns due to knee pain can be more severe than the risky case of spinal fusion. Furthermore, the study's results suggest that the cup orientation determined from pre-surgery motion recordings may not be the same post-surgery under hip joint pain conditions.

It is worth noting that the "what-if" scenarios analyzed in the study are just a few examples of the many subject-specific conditions that a patient may have. The primary aim of the study was to demonstrate the value of predictive simulations in providing insights into the impact of different patient-specific conditions to assist in adjusting implant positioning.

In contrast to the motion capture-based method, the predictive simulation approach has two main disadvantages. Firstly, each simulation in this method takes around 4.5 hours on average to complete in a Windows 10 64-bit operating system with Intel Core i7 3.6 GHz processor and a 16 GB RAM, making it unsuitable for intra-operative applications. Secondly, generating subject-specific simulations in this approach is more difficult than in the motion capture-based method because the predicted motion depends on many subject-specific parameters, such as muscle properties and optimization problem tuning, which may necessitate a degree of proficiency in mathematics and physics. To address this issue, we suggest creating a library of cost-functions associated with different patient conditions that surgeons can select and use when performing predictive simulations. While this approach may provide surgeons with general insights into how selected conditions might impact a patient's motion pattern, it is still challenging to use this method in a clinical setting to generate subject-specific simulations [15].

Additionally, even though the techniques presented in the previous two chapters offer an approach for determining the optimal patient-specific cup alignment based on implant impingement and edge-loading, developing a comprehensive algorithm for determining optimal cup orientation requires considering other factors such as bony impingement [100,206],

implant wear [93], soft tissue management [207], and implant design choice [208]. Also, to comprehensively evaluate the model, validation of the optimal cup alignment obtained from the model against a gold standard measurement is necessary.

Chapter 5

Optimal Knee Implant Positioning Following Total Knee Arthroplasty

5.1 Introduction

Total Knee Arthroplasty (TKA), as explained in Section 1.2, is a surgical procedure that aims to alleviate knee pain and improve mobility in patients with knee osteoarthritis. Although TKA has been performed for several decades, the optimal positioning of knee implants remains a challenge [141]. The proper placement of the femoral and tibial components is essential for the success of the procedure and can significantly affect the long-term outcomes of TKA [142]. Therefore, there is a need to develop reliable and efficient methods to optimize the positioning of the knee implants.

In this chapter, the aim is to find the optimal knee implant positioning following TKA based on predictive dynamic simulations. To achieve this goal, two knee models are used in a co-simulation framework: a detailed volumetric contact model that includes the surrounding ligaments and has 12 degrees-of-freedom (DoF), and a simpler single-degree-of-freedom equivalent kinematic (SEK) joint model. The former provides high-level details and can

predict secondary kinematics (all five DoF apart from the flexion-extension motion), while the latter has much less computational time, which is advantageous in optimization loops.

The experimental data used is described in Section 5.2, while the modifications made to the original musculoskeletal model from Chapter 4 are discussed in Section 5.3. Section 5.4 presents the specifics of the two knee models. To calibrate the ligament parameters of the model, the experimental data from the 4th Grand Challenge Competition [13] is utilized. Additionally, the same dataset is utilized in Section 5.5 to validate the models, which exhibit a good agreement with the experimental data. Section 5.6 outlines the three main metrics employed in this study to assess the results of TKA: medial and lateral load distribution, ligament balancing, and varus-valgus alignment. These factors are mathematically quantified to better understand their impact on the outcome of TKA. In Section 5.7, the effect and sensitivity of the placement of the femoral and tibial components on the three aforementioned factors are investigated. Finally, in Section 5.8, these factors are utilized to determine the optimal placement of the knee implant components, aiming to achieve desired values for medial and lateral load distribution, ligament balancing, and varus-valgus alignment concurrently.

5.2 Experimental Data

The data used in this chapter was obtained from a publicly accessible database for the 4th Grand Challenge Competition Predicting In Vivo Knee Loads [13]. This is a standardized dataset widely used by the scientific community to validate musculoskeletal models. The database consists of Computed Tomography (CT) scans (pre- and post-op) of a male subject (88 years old, 168 cm tall, and weighing 66.7 kg) who underwent a TKA due to primary osteoarthritis and received a telemetrically monitored TKA using the first-generation eKnee tray design of standard size [209]. The database encompasses 3D geometric Standard Triangle Language (STL) representations of the lower right limb bones (pelvis, femur, patella, tibia) and implant components, along with motion capture data of daily living

movements, knee kinematics obtained from fluoroscopy images, Ground Reaction Forces (GRF), and Electromyography (EMG) signals. Further information on this dataset can be found in [13].

5.3 Musculoskeletal Model

The model of the musculoskeletal system detailed in Section 4.2 was utilized as the starting point. The models segments were linearly scaled based on the subject's height and mass. Given the subject's age of 88 years, and the knowledge that muscle strength decreases by roughly 15% every decade after the age of 50 [210], the maximum isometric force for each muscle in the model was adjusted using a scaling factor of $0.85^3 \approx 0.6$. As depicted in Fig. 5.1, the model was also supplemented with six muscle-tendon units that were responsible for knee joint flexion and extension. The following muscles were added to the model to actuate the knee joint: rectus femoris, vastus medialis, vastus lateralis, vastus intermedius, gastrocnemius medialis, and gastrocnemius lateralis.

5.4 Knee Implant Model

In this study, two knee implant models were established and utilized, the first being a comprehensive 12 degree-of-freedom (DoF) model incorporating the contact between femoral and tibial implants, patellofemoral contact, and ligaments. The second model is a Single-degree-of-freedom Equivalent Kinematic (SEK) representation of the knee joint. The first model provides a higher level of detail and allows for the calculation of contact forces on both the medial and lateral sides of the knee joint. On the other hand, the second model is less computationally intensive and more efficient to simulate. Further information about each model is given in the subsequent two subsections.

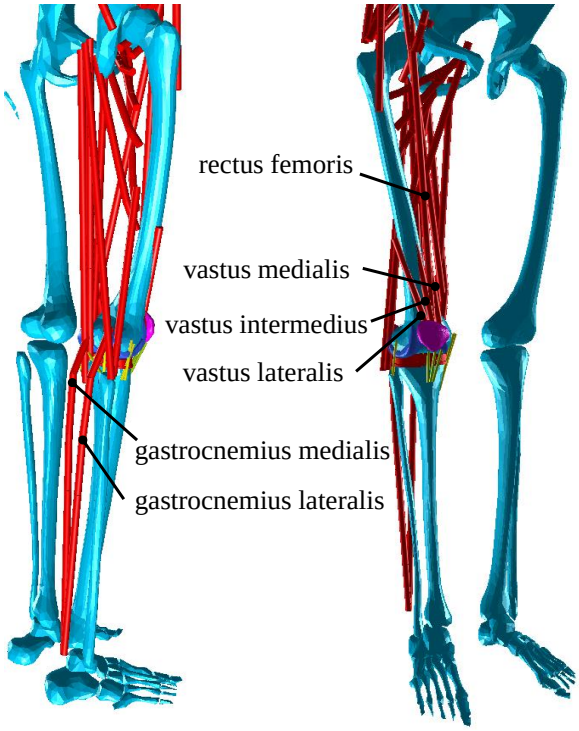

Figure 5.1: Muscles added to the musculoskeletal model to actuate the knee joint.

5.4.1 12 DoF Model

A 12 DoF knee joint model was created to predict the contact force on the medial and lateral sides of the knee implant and to calculate the secondary movements of the knee joint, encompassing three translational movements (anterior/posterior, superior/inferior, and medial/lateral) and two rotational movements (internal/external and abduction/adduction). This model has 6 DoF for the motion of the femur relative to the tibia and 6 DoF for the motion of the patella relative to the femur.

Ligament Modeling

As shown in Fig. 5.2, the following seven ligaments were included in the knee joint model: medial collateral ligament (MCL), lateral collateral ligament (LCL), posterior capsule

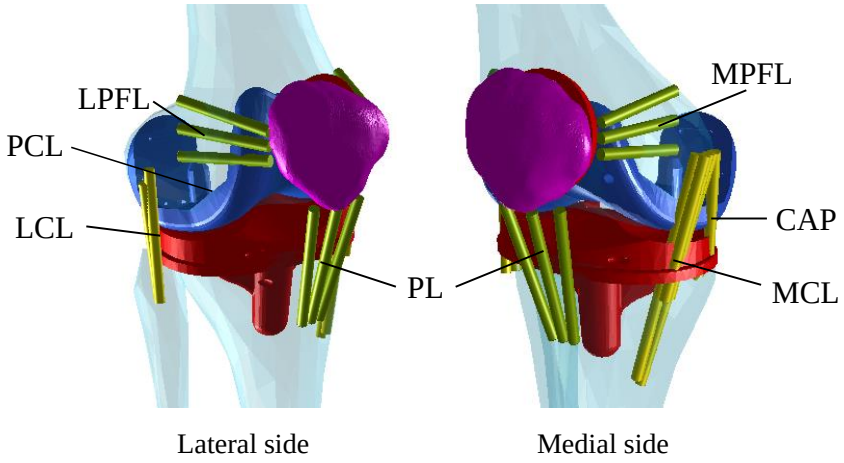

Figure 5.2: Ligaments included in the musculoskeletal model.

(CAP), posterior cruciate ligament (PCL), medial patellofemoral ligament (MPFL) and lateral patellofemoral ligament (LPFL), and patellar ligament (PL). As the anterior cruciate ligament (ACL) is sacrificed during TKA, it was not included in the model. Each ligament was divided into separate bundles for a more detailed model. For the CAP, these bundles include the arcuate (aCAP), popliteal lateral (lCAP), medial (mCAP), and oblique popliteal (oCAP) bundles. The MCL was divided into anterior (aMCL), intermediate (iMCL), and posterior (pMCL) bundles. The LCL was divided into anterior (aLCL) and posterior (pLCL) bundles. The LPFL was split into proximal (pLPFL), middle (mLPFL), and distal (dLPFL) bundles, while the MPFL was divided into proximal (pMPFL), middle (mMPFL), and distal (dMPFL) bundles. The PL was divided into medial (mPL), intermediate (iPL), and lateral (lPL) bundles. Given the absence of ligament geometry data for the test subject, the origins and insertions of the ligaments were estimated by referencing the descriptions of bony landmarks associated with each ligament from various literature sources [211–215].

The force exerted by each ligament bundle was calculated by representing it as a tension-only spring element modeled as a straight line connecting the origin and inser-

tion points [216]:

$$f = \begin{cases} k\left(\varepsilon - \varepsilon_L\right), & \varepsilon > 2\varepsilon_L \\ k\dfrac{\varepsilon^2}{4\varepsilon_L}, & 0 \le \varepsilon \le 2\varepsilon_L \\ 0, & \varepsilon < 0 \end{cases} \tag{5.1}$$

$$\varepsilon = \frac{l - l_0}{l_0} \tag{5.2}$$

where the variables in the equation include the ligament strain ε, the transition strain ε_L, which has a value of 0.03 [217], the stiffness parameter k, which is expressed as the ratio of force to strain, the actual length of the ligament l, and the slack length of the ligament l_0.

Contact Modeling

The knee joint model with 12-DoF consists of two distinct joints. The first joint, with 6 degrees-of-freedom, is the tibiofemoral joint, which involves the articulation between the medial and lateral condyles of the femur and the tibia. The second joint, also with 6-DoF, is the patellofemoral joint where the patella articulates against the trochlear groove. As shown in Fig. 5.3, two sphere-to-sphere compliant volumetric contact models [113,218] were used to model the contact between the medial and lateral sides of the femoral component and the medial and lateral sides of the tibial component. Additionally, two sphere-to-sphere volumetric contact models were used to model the contact between the patella and the trochlear groove on the femoral component.

The volumetric contact model yields the normal and tangential friction forces, obtained respectively as [113, 218]:

$$\mathbf{F}_n = k_v V \left(1 + a_V \left|\mathbf{v}_{cn}\right|\right) \hat{\mathbf{n}} \tag{5.3}$$

$$\mathbf{F}_t = \left|\mathbf{F}_n\right| \mu \left(\left|\mathbf{v}_{ct}\right|\right) \frac{\mathbf{v}_{ct}}{\left|\mathbf{v}_{ct}\right|} \tag{5.4}$$

The variables in the equations are as follows: V represents the volume of penetration, $\mathbf{v}_{cn}$ and $\mathbf{v}_{ct}$ denote the relative normal and tangential velocity of the centroid, C, of the penetration volume, respectively. $\mathbf{F}_n$ and $\mathbf{F}_t$ act at C. Additionally, the volumetric stiffness

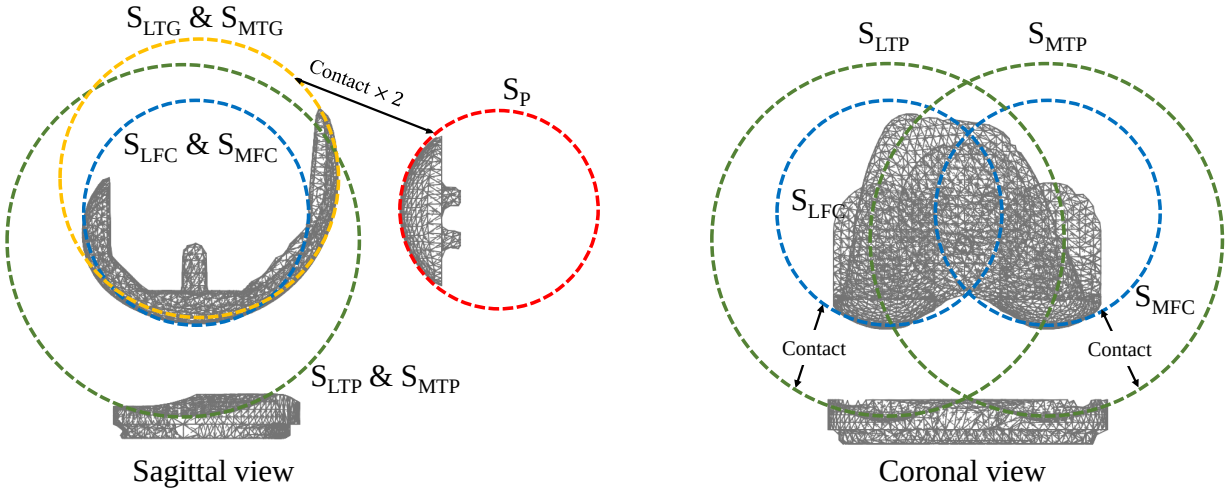

Figure 5.3: Contact model of the knee implant. The figure displays various contact spheres, each indicated by a circle. Specifically, S_{LFC} and S_{MFC} mark the lateral and medial condyles at the femur, S_{LTP} and S_{MTP} denote the lateral and medial tibial plateaus, and S_{LTG} and S_{MTG} represent the lateral and medial trochlear grooves. Additionally, the sphere that stands for the patellar button is identified as S_P.

k_v is set to 2×10^9 N/m^3 [113], and the damping coefficient a_V is set to -0.1 s/m to reduce high-frequency responses. Moreover, the ratio of friction to normal force, $\mu(v)$, is defined as:

$$\mu(v) = \mu_d \tanh\left(\frac{4v}{v_t}\right) + (\mu_s - \mu_d) \frac{\frac{v}{v_t}}{\left(\left(\frac{v}{2v_t}\right)^2 + \frac{3}{4}\right)^2} \tag{5.5}$$

We used a static and dynamic frictional coefficient of $\mu_s = 0.04$ and $\mu_d = 0.01$, respectively, for the patellofemoral and tibiofemoral contact in our model, which is consistent with previous studies [110, 133] that have reported good agreement with experimental data using these values. Also, a value of 0.005 m/s was assigned to v_t, which represents the transition velocity from sticking to sliding.

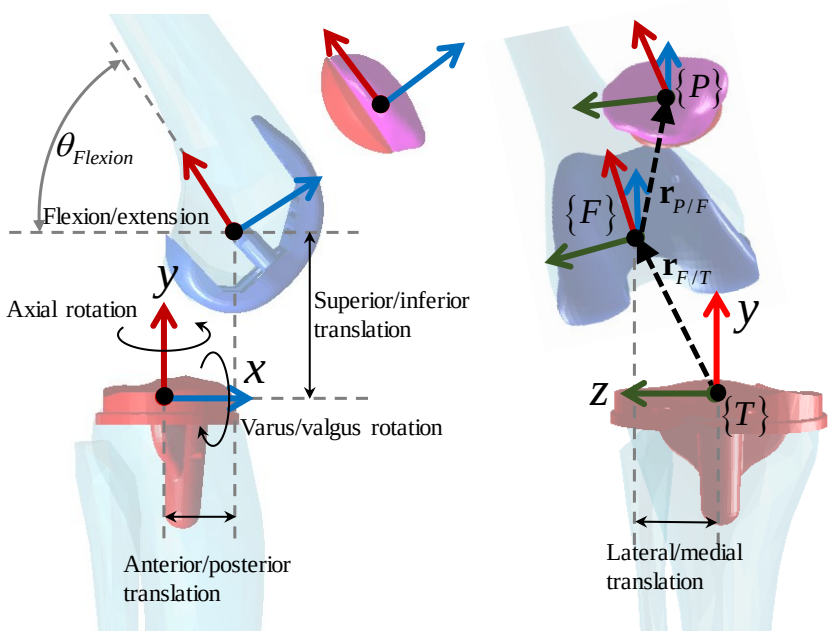

Figure 5.4: The relative motion of different parts of the knee joint.

5.4.2 Single-DoF Equivalent Kinematic (SEK) Model

A Single-Degree-of-Freedom Equivalent Kinematic (SEK) joint is a mechanism that describes the kinematics of a complex 1-DoF system that experiences both translational and rotational displacements with respect to a single independent variable. SEK joints are utilized in various studies to simplify intricate systems, such as car suspensions, for quicker simulation times [219].

In this study, the motion of the knee joint is described using two SEK joints as a function of the knee flexion angle: (1) tibiofemoral joint, which represents the movement of the femur relative to the tibia and includes three translations (anterior-posterior, medial-lateral, and superior-inferior) and two rotations (internal-external and abductin-adduction), and (2) patellofemoral joint, which represents the movement of the patella relative to the femur:

$$\begin{bmatrix} {}^{F}\mathbf{r}_{P/F} \\ \theta_{P/F} \end{bmatrix} = \mathbf{\Psi}_{P/F}\left(\theta_{Flexion}\right) \tag{5.6}$$

$$\begin{bmatrix} {}^{T}\mathbf{r}_{F/T} \\ \theta_{F/T} \end{bmatrix} = \mathbf{\Psi}_{F/T}\left(\theta_{Flexion}\right) \tag{5.7}$$

Here, as shown in Fig. 5.4, ${}^{F}\mathbf{r}_{P/F}$ and ${}^{T}\mathbf{r}_{F/T}$ denote the positions of the patella relative to the femur in the femur coordinate frame and the femur relative to the tibia in the tibia coordinate frame, respectively. $\theta_{P/F}$ and $\theta_{F/T}$ are column matrices containing the rotation angles of the patella relative to the femur and the femur relative to the tibia in the body-fixed xyz-Euler angle convention. $\mathbf{\Psi}_{P/F}$ and $\mathbf{\Psi}_{F/T}$ are each a 6 by 1 column matrix containing six spline functions for the corresponding SEK joint expressed in terms of the knee flexion angle.

Compared to the common method of utilizing an ideal revolute joint to model the knee joint, the SEK joint provides more accurate kinematics without increasing simulation time. While this knee model is faster to simulate compared to the 12-DoF model, it cannot determine medial and lateral contact forces or account for the impact of varying loads on knee kinematics due to its limited 1-DoF.

5.4.3 Co-simulation Between SEK Model and Contact Model

The knee models created in this research, specifically the SEK model and the volumetric contact model, each possess their own pros and cons. The volumetric contact model's strength lies in its ability to forecast contact forces and secondary knee joint kinematics based on external loads and muscle forces. However, due to the presence of high stiffness contact parameters, it necessitates small simulation time steps and is unsuitable for scenarios requiring a high number of iterative simulations, such as optimization problems. Conversely, the SEK model is a kinematically-based model with fast computation, but it cannot predict secondary movements and contact forces since these movements are predetermined as a function of the knee joint flexion angle.

Figure 5.5 illustrates the combined use of these two models to capitalize on their respective benefits. The SEK joint model, with initially predefined functions $\mathbf{\Psi}_{P/F}$ and

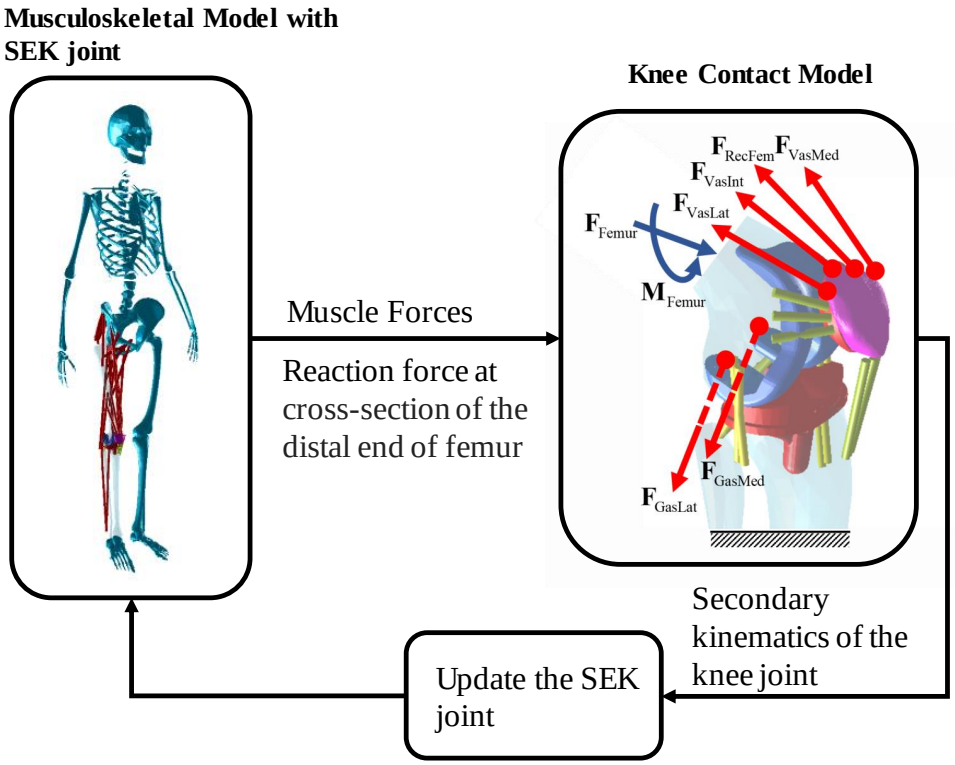

Figure 5.5: The co-simulation framework.

$\mathbf{\Psi}_{F/T}$, is employed in the musculoskeletal model, where the muscle forces and reaction forces and moments at the femur's distal cross-section are determined. These forces are then applied to the volumetric knee contact model, where the knee flexion angle is the only knee DoF derived from the musculoskeletal simulation result. The remaining 11 DoFs (5 tibiofemoral and 6 patellofemoral) are calculated under the influence of external loads, muscle, ligament, and contact forces for the entire movement. Subsequently, the calculated secondary kinematics are utilized to update the SEK joint model ($\mathbf{\Psi}_{P/F}$ and $\mathbf{\Psi}_{F/T}$), and this cycle continues until the SEK joint and contact model converge. It is important to note that the convergence of this process is typically fast (usually after two iterations) due to the insignificant impact of the knee joint's secondary motions on the overall dynamic performance of the musculoskeletal model.

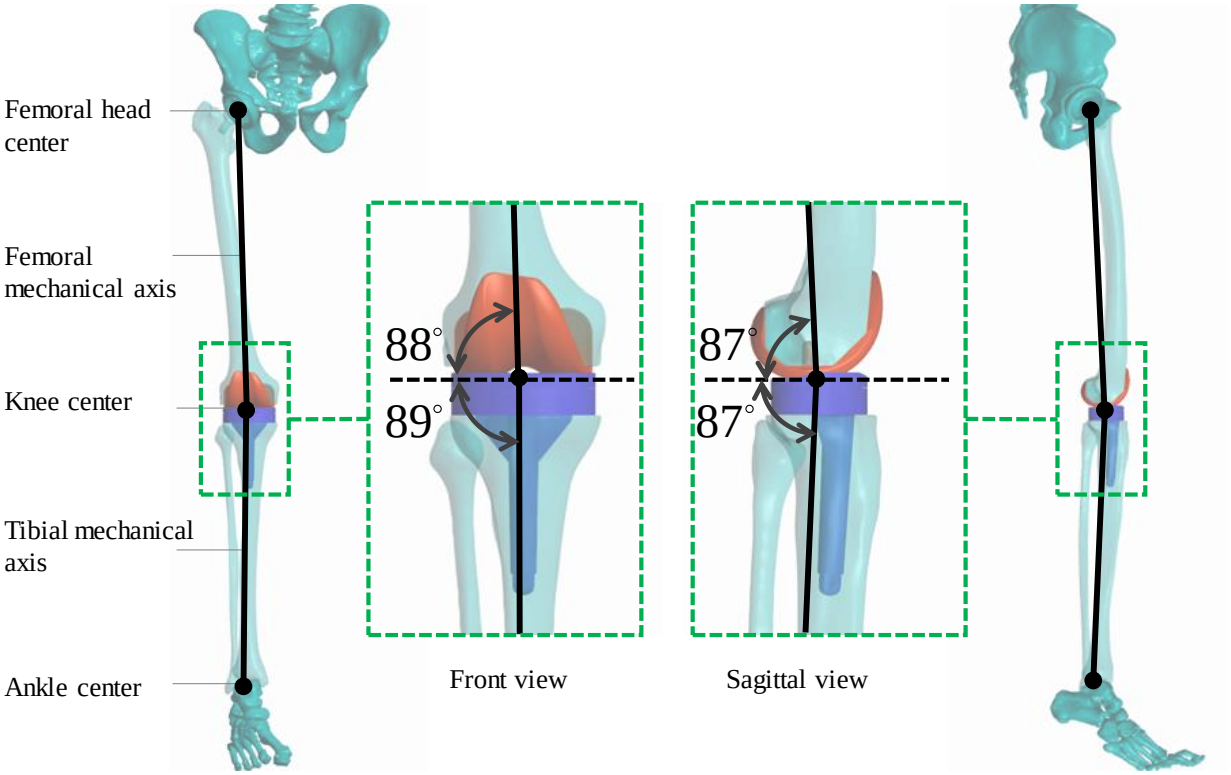

Figure 5.6: The assembled patient-specific CAD model of the lower limbs and knee implant [13].

5.5 Model Calibration and Validation

Considering that knee models are highly sensitive to the slack lengths or positions of ligaments due to their significant stiffness [220], this section focuses on calibrating the ligament slack lengths by minimizing discrepancies between the knee contact force magnitude at each condyle, specifically the medial and lateral sides, as determined by the model and the experimental data from the 4th Grand Challenge Competition gathered during a sit-to-stand motion. Initially, as illustrated in Fig. 5.6, the tibial and femoral components of the knee implant are positioned according to the post-operative CAD files present in the dataset [13], which were acquired from the patient's CT scans following TKA surgery. Subsequently, us-

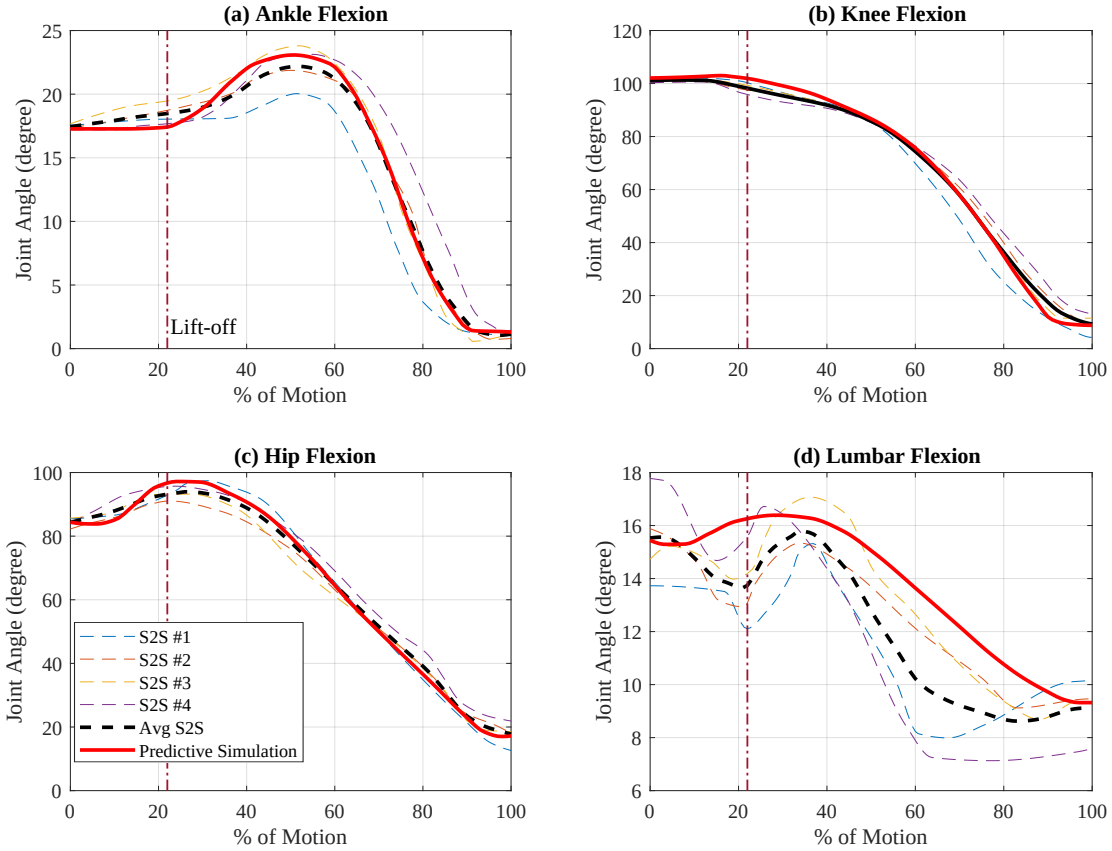

Figure 5.7: The comparison between predicted and experimental joint angles for sit-to-stand motion. (a) Ankle flexion. (b) Knee flexion. (c) Hip flexion. (d) Lumbar flexion.

ing the approach described in Section 4.3, an optimal control-based sit-to-stand movement is predicted to match the experimental joint angles and normal foot-ground contact force of the patient during four sit-to-stand motions referred to as "jw_chairrise1". To achieve this parameter identification, the cost function presented in Section 4.3 for predicting sit-to-stand motion (J_1 denotes the cost prior to lift-off, while J_2 represents the cost after lift-off) was modified as follows:

$$J_1 = \|\mathbf{a}(t)\|^2 + a\left(\dot{\theta}_{Ankle}(t)^2 + \dot{\theta}_{Knee}(t)^2\right) + b\|\theta(t) - \theta_{Exp}(t)\|^2 + c\left(\frac{F_{GF}(t) - F_{GF,Exp}(t)}{W}\right)^2 \quad (5.8)$$

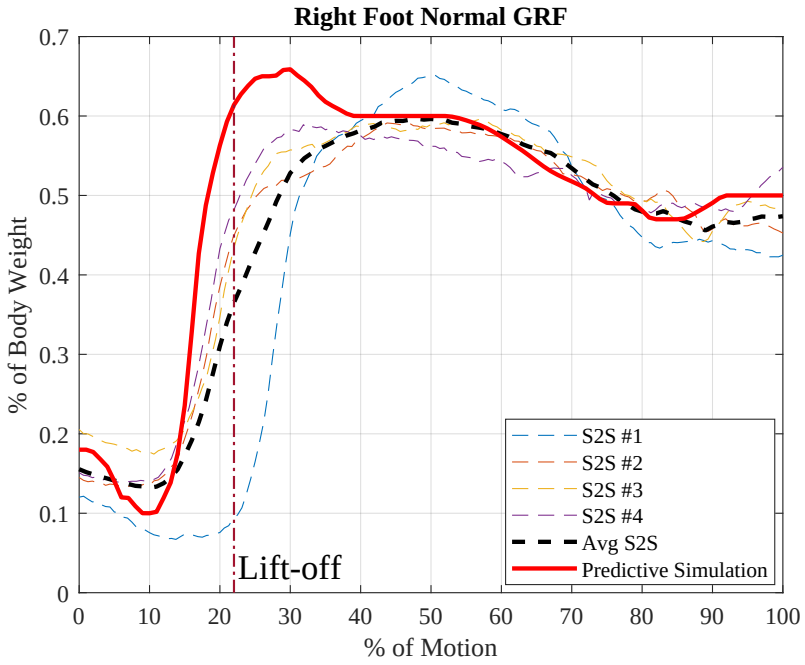

Figure 5.8: The comparison between predicted and experimental normalized foot-ground contact force.

$$J_2 = \|\mathbf{a}(t)\|^2 + b\|\theta(t) - \theta_{Exp}(t)\|^2 + c\left(\frac{F_{GF}(t) - F_{GF,Exp}(t)}{W}\right)^2 \tag{5.9}$$

where, θ and θ_{Exp} represent the predicted and average experimental joint angles, respectively, while F_{GF} and $F_{GF,Exp}$ denote the predicted and average experimental normal foot-ground contact forces, respectively. As in the simulations conducted in Section 4.3, the value of a was set to 1.7 (s/rad)^2. The values of b and c were set to $\left(36/\pi \quad \frac{1}{\text{rad}}\right)^2$ and 400, respectively. This implies that the cost of a 5-degree error between the experimental and predicted joint angle and a 5% error between the predicted and experimental normal foot contact force, normalized to body weight (W), is equal to the cost of full muscle activation, which is 1.

Figure 5.7 presents a comparison between the experimental and the predicted joint angles, while Fig. 5.8 shows a comparison between the normalized predicted foot-ground

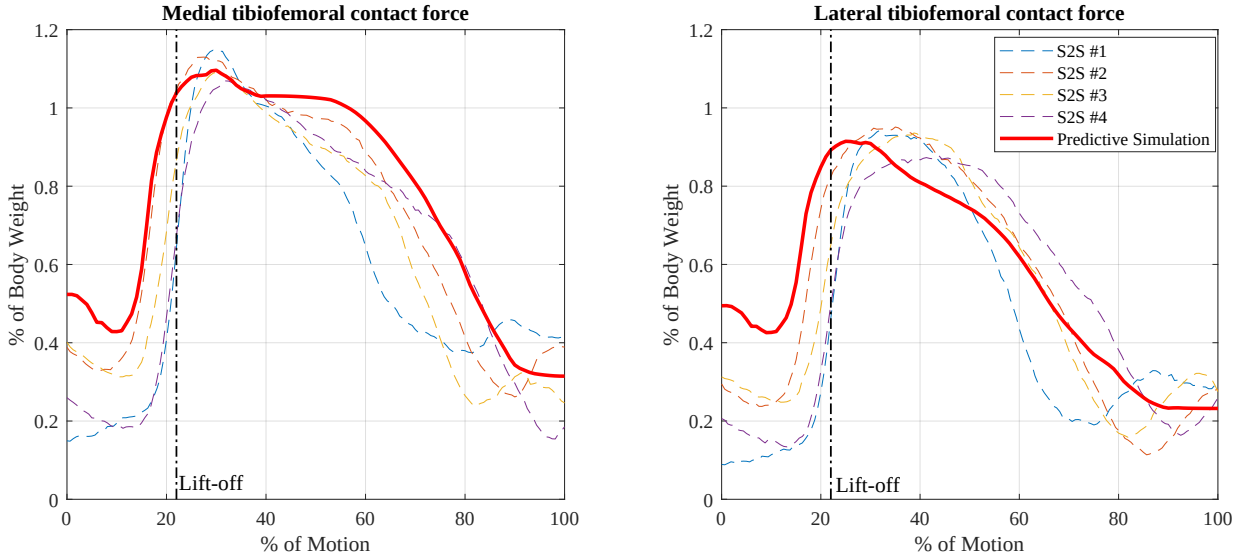

Figure 5.9: Comparison between the predicted and experimental normalized medial and lateral tibiofemoral contact forces.

contact force and the corresponding experimental data. In general, there is good correspondence between the predicted outcomes and the actual measurements, both in terms of their magnitude and overall pattern, especially after the moment when the buttocks lose contact with the chair (referred to as the moment of lift-off). Specifically, the root mean square error (RMSE) between the model and experimental data is approximately 8.7% of the body weight, and the Pearson correlation coefficient is approximately 0.88. One possible reason for the discrepancy between the model and experimental data could be the assumption of left-right symmetry in the model, whereas in reality, the GRF on the left and right sides may not be equal. In fact, upon examining the experimental data, it was observed that, on average, the GRF on the left side is higher than that on the right side. This limitation of the model is further discussed in the Conclusion chapter, specifically in Section 6.2.

It is noteworthy that the experimental data exhibits a sudden alteration in the angle of the lumbar joint just prior to the chair lift-off point. This was not observed in a previous

experimental study [190], nor did the model in this study replicate the lumbar joint angle pattern before lift-off, as indicated by Fig. 5.7 (d). This issue may be resolved with a more detailed spine model. However, given that the maximum error in lumbar flexion is less than 4 degrees, this discrepancy is unlikely to significantly impact the analysis of the knee joint as long as the predicted foot-ground contact force and lower limb joint angles are reasonably accurate.

To determine the subject-specific slack length of ligaments, the following optimization problem is solved by minimizing the error between experimental measurements and calculated contact forces on both the medial and lateral sides of the knee:

$$\begin{aligned} &\min_{{l_0}^{(1)},\cdots,{l_0}^{(n)}} \quad \int \left[\left(F_{Med,Model} - F_{Med,Exp}\right)^2 + \left(F_{Lat,Model} - F_{Lat,Exp}\right)^2 \right] dt \\ &\text{s.t.} \quad \left| \frac{{l_0}^{(i)}}{l_{0,nom}^{(i)}} - 1 \right| \leq 0.1 \quad \text{for} \quad i = 1, \cdots, n \end{aligned} \tag{5.10}$$

where $F_{Med,Model}$ and $F_{Lat,Model}$ are respectively the magnitudes of the medial and lateral knee contact forces obtained from the model, and $F_{Med,Exp}$ and $F_{Lat,Exp}$ are respectively the average medial and lateral contact forces obtained from the experimental data across all trials. To ensure realistic results, the change in ligament slack length was constrained to 10% of the original length. The nominal value of the ligament slack length, $l_{0,nom}^{(i)}$, was taken from the literature [221–225]. The stiffness of each ligament, along with the optimized values of the slack lengths, can be found in Table 5.1. Figure 5.9 presents the comparison between the predicted and experimental medial and lateral tibiofemoral contact forces using the optimized ligament parameters.

5.5.1 Secondary Kinematics

Figures 5.10 and 5.11 respectively illustrate a comparison between the predicted secondary knee kinematics and trajectories of contact points on the medial and lateral sides with those derived from fluoroscopy measurements in the 4th grand challenge dataset. Overall,

Table 5.1: Mechanical properties of the implemented ligaments. Stiffness is quantified in Newtons per unit strain.

Ligament	Stiffness(N)	Slack length (mm)	Ligament	Stiffness(N)	Slack length (mm)
aPCL	2600	44.2	pMCL	2500	57.2
pPCL	1900	40.56	pMPFL	140	48.2
aLCL	2000	63.7	mMPFL	140	50.7
pLCL	2000	65.2	dMPFL	140	48.3
CAPa	1350	72.8	pLPFL	140	47.4
CAPl	2000	46.8	mLPFL	140	48.8
CAPo	1500	78	dLPFL	140	47.3
CAPm	2000	46.8	lPL	58,000	98.6
aMCL	2500	100.1	iPL	58,000	95.8
iMCL	3000	106.6	mPL	58,000	97.8

the predicted secondary kinematic motion corresponds well with the actual measurements, as shown in Table 5.2 through evaluation metrics including RMSE and Pearson correlation coefficient (r). The largest difference between the experimental and predicted motion pattern is observed around the lift-off instance, which occurs at approximately 95 degrees of knee flexion angle. The experimental data indicates medial translation of the joint as the knee extends while the simulation predicts lateral translation. This difference is also noticeable in the predicted trajectory of center of pressure (see Fig. 5.11) on the lateral side during high knee flexion angles. Nevertheless, there is generally a good agreement between the results obtained from the knee joint model and the experimental measurements.

5.6 Factors Influencing the Result of TKA

The literature contains a debate regarding the optimal placement of implants in TKA, and there is a lack of consensus on what constitutes a balanced knee replacement [10, 141,

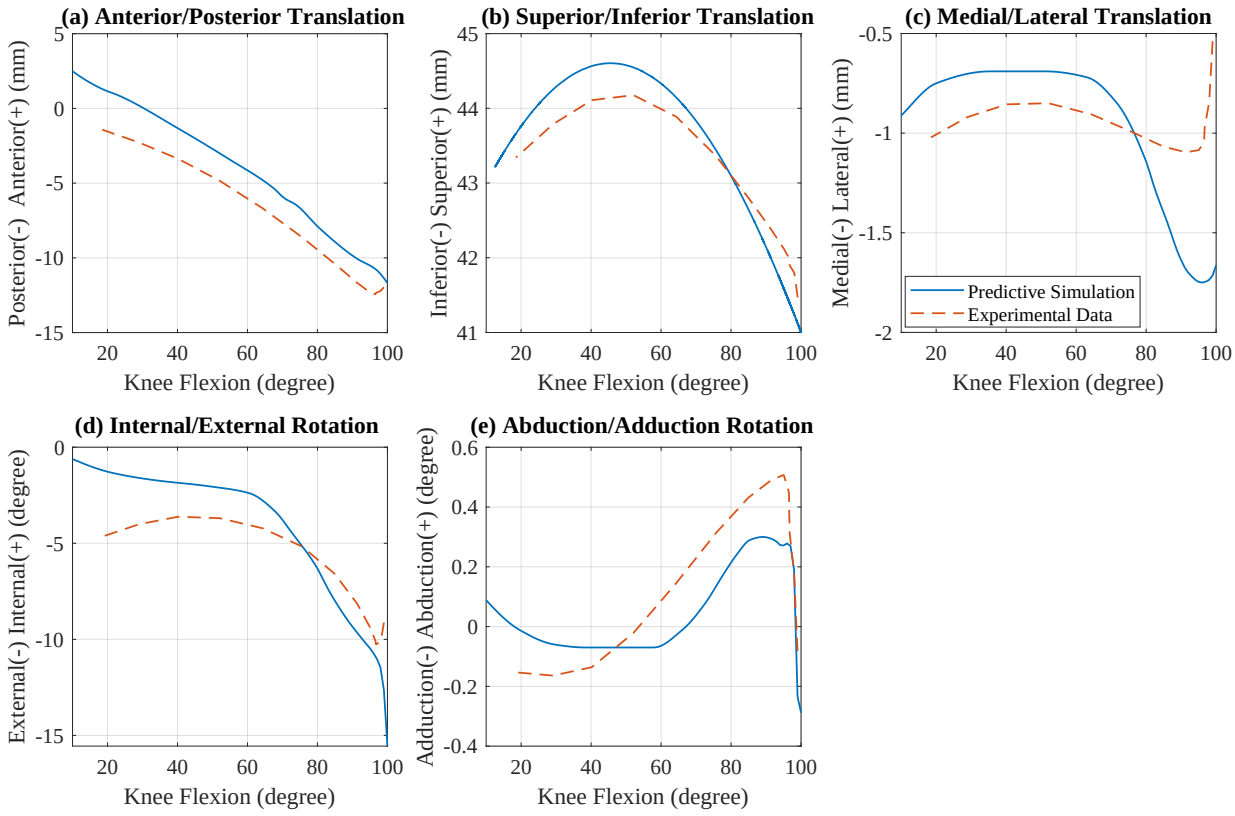

Figure 5.10: The comparison between predicted and measured secondary kinematics of the knee joint over sit-to-stand motion. (a) Anterior/Posterior (A/P) translation. (b) Superior/Inferior (S/I) translation. (c) Medial/Lateral (M/L) Translation. (d) Internal/External (I/E) rotation. (e) Abduction/Addiction (A/A) rotation.

Table 5.2: The correspondence between predicted and measured secondary knee kinematics during sit-to-stand.

Evaluation Metric	Traslational			Rotational	
	A/P	S/I	M/L	I/E	A/A
RMSE	1.77 mm	0.42 mm	0.62 mm	1.9 deg	0.14 deg
Pearson Correlation Coeff. (r)	0.997	0.995	0.821	0.965	0.890

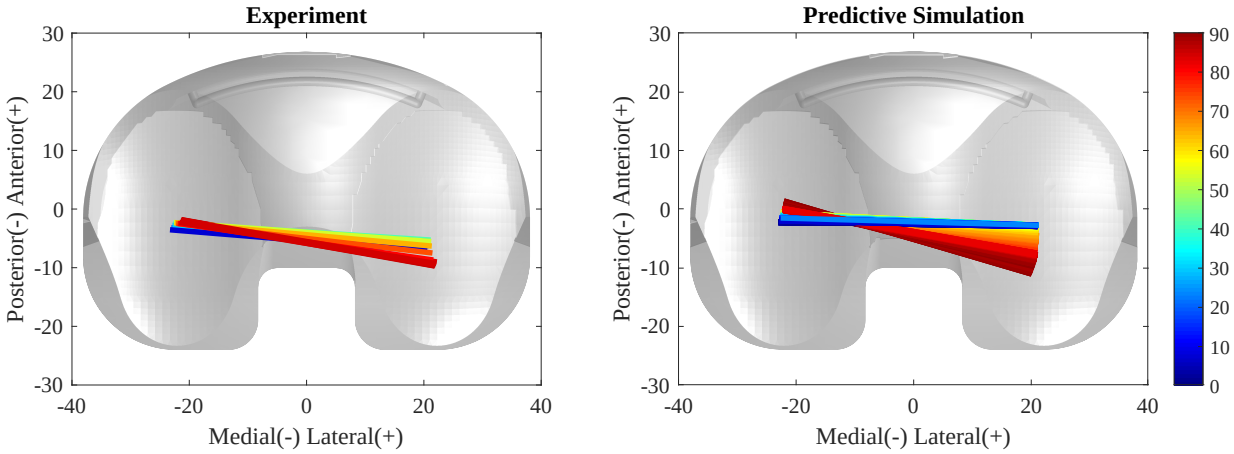

Figure 5.11: The comparison between predicted and experimental center of pressure on tibial insert. The colormap indicates the knee flexion angle. The lines connect the centers of pressure on the medial and lateral sides at each moment.

142]. Nonetheless, after examining the literature, three primary factors emerge as having a significant impact on the outcome of TKA [226–229]: (1) achieving a balance in the load distribution between the medial and lateral compartments, (2) properly balancing and tensioning the medial and lateral ligaments, and (3) attaining proper valgus/varus alignment. Subsequent sections will delve deeper into each of these factors and introduce a suitable mathematical index for each factor, which will later assist in determining the optimal placement of knee implants.

5.6.1 Medial and Lateral Load Distribution

The natural healthy knee typically has a mechanical axis (an imaginary line from the center of the femoral head to the center of the ankle joint) that is situated closer to the medial side of the knee joint, resulting in greater normal force on the medial compartment [230]. However, for TKA, some sources suggest that implant positioning should be adjusted to prevent excessive loading on the medial compartment, which could result in uneven wear and premature failure [145, 231]. To assess the balance of load distribution between the

medial and lateral compartments, the following index was developed in this study:

$$\mathcal{I}_{LD} = \ln\left(\frac{F_{Med}}{F_{Lat}}\right) \tag{5.11}$$

where as defined in Eq. (5.10), F_{Med} and F_{Lat} are respectively the magnitudes of the medial and lateral knee contact forces. By utilizing this Load Distribution (LD) index[1], it is possible to determine the optimal placement of knee implants that will result in a desired load distribution. This is achieved by minimizing the following cost function:

$$C_{LD} = (\mathcal{I}_{LD} - \mathcal{I}^*_{LD})^2 \tag{5.12}$$

where $\mathcal{I}^*_{LD}$ represents the desired proportion of force between the medial and lateral compartments. For instance, $\mathcal{I}^*_{LD} = 0$ signifies an equal distribution of load between the medial and lateral sides.

5.6.2 Ligament Balancing

Achieving balanced tension of the medial and lateral ligaments is crucial in TKA, as imbalanced ligament tension can lead to joint instability and stiffness, which are among the primary causes for revision TKA [228, 232]. One commonly used technique to attain balanced tension of ligaments on both sides of the knee joint is gap-balancing [233]. This method involves making a tibial bone cut first, followed by applying symmetrical tension to the joint line in both extension and 90 flexion using a ligament tensor, knee balancer, or laminar spreaders [141]. The femoral component is then positioned to achieve equal and symmetrical medial and lateral gaps in both flexion and extension.

However, gap-balancing has a significant drawback in that it only evaluates and balances tension at 0 and 90 flexion angles, failing to account for the entire range of motion. Consequently, this method may result in mid-flexion instability [234, 235]. Furthermore,

[1]The logarithmic function was employed to achieve a symmetrical outcome for F_{Med}/F_{Lat} and its inverse.

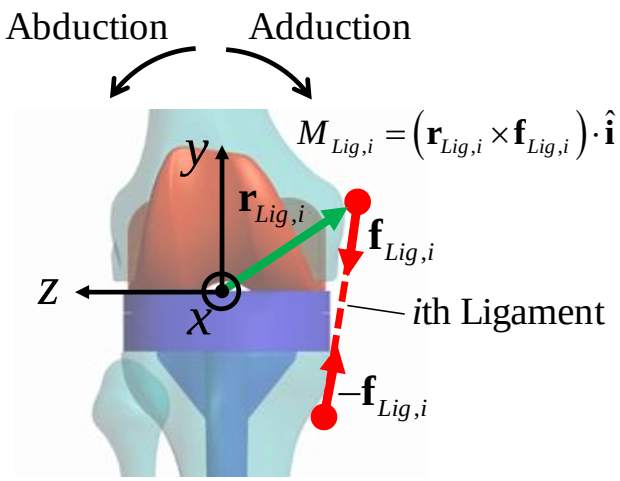

Figure 5.12: The ith ligament force's moment with respect to the anteroposterior axis (in the direction of the x-axis).

the goal of gap-balancing contradicts the ligament balance in the natural knee, as evidenced by cadaveric research [236]. The native knee possesses an inherently relaxed LCL relative to the MCL, which contrasts with the proposed symmetrical medial-lateral balance in a TKA. Additionally, there is more rollback of the lateral femoral condyle than the medial, with internal rotation of the tibia in flexion, as opposed to the rectangular tibiofemoral flexion gap in a TKA. To evaluate ligament balance, this study introduced the following index:

$$\mathcal{I}_{LB} = \ln\left(\frac{\sum |M_{Lig,i}| + M_{Lig,i}}{\sum |M_{Lig,i}| - M_{Lig,i}}\right) \tag{5.13}$$

where, as shown in Fig. 5.12, $M_{Lig,i} = (\mathbf{r}_{Lig,i} \times \mathbf{f}_{Lig,i}) \cdot \hat{\mathbf{i}}$ is the moment produced by the force of the ith ligament around the anteroposterior axis (x-axis in Fig. 5.12), which passes through the center of the tibial component. It's worth noting that the fraction inside the $\ln(\cdot)$ function in Eq. (5.13) has the numerator and denominator as the sum of the knee abduction and adduction moments generated by the ligament forces. Therefore, when the medial and lateral ligaments are perfectly balanced, $\mathcal{I}_{LB}$ becomes zero. Using this Ligament Balance (LB) index, it is possible to optimize the positioning of the knee implant to achieve

a specific target for $\mathcal{I}_{LB}$ by minimizing the following cost function:

$$C_{LB} = \left(\mathcal{I}_{LB} - \mathcal{I}^*_{LB}\right)^2 \tag{5.14}$$

where the value of $\mathcal{I}^*_{LB}$ determines the desired level of medial-lateral ligament laxity: a value of $\mathcal{I}^*_{LB} = 0$ results in symmetrical laxity, while $\mathcal{I}^*_{LB} > 0$ leads to a looser LCL relative to the MCL, and conversely, a value of $\mathcal{I}^*_{LB} < 0$ results in a looser MCL compared to the LCL.

5.6.3 Varus/Valgus Alignment

The angle between the mechanical axis of the femur and the tibia, projected into the coronal plane, is referred to as the valgus/varus angle. The formula to calculate this angle for the right knee joint is given as follows, as depicted in Fig. 5.13:

$$\alpha_{VV} = \arcsin\left(\left(\widehat{KH} \times \widehat{AK}\right) \cdot \hat{\mathbf{i}}\right) \tag{5.15}$$

where α_{VV} represents the varus/valgus angle, and $\widehat{KH}$ and $\widehat{AK}$ are unit vectors along the femoral and tibial mechanical axis, respectively. A positive value of α_{VV} indicates varus alignment, while a negative value indicates valgus alignment.

In recent years, there has been increasing attention on alignment in TKA as a means of improving patient satisfaction [143]. Various alignment philosophies have been proposed, which can be broadly categorized into three main groups [237]: (1) Mechanical alignment (MA), which aims to position the femoral and tibial components perpendicular to the mechanical axis of each bone, thus aligning their mechanical axes [145]; (2) Kinematic alignment (KA), which seeks to maintain the natural alignment of the limb [238]; and (3) Hybrid alignment approaches, which aim to preserve the native coronal alignment within a safe varus/valgus range of $-3^\circ < \alpha_{VV} < 3^\circ$. Some studies have suggested that the KA technique results in greater range of motion and higher rates of post-operative satisfaction in TKA compared to MA [150], while other research has found similar outcomes for both techniques [151]. Given the lack of a definitive agreement on which alignment method

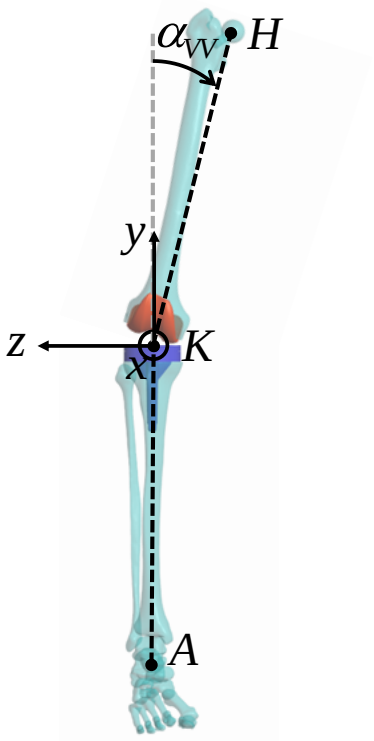

Figure 5.13: The angle of varus/valgus (α_{VV}) alignment of the right knee joint. A positive value of α_{VV} implies that the knee has a varus alignment, as depicted here, while a negative value of α_{VV} indicates a valgus alignment.

produces better results, we have included varus/valgus alignment angle as a parameter in our optimization problem, which will be elaborated on in Section 5.8.

5.7 The Effect of Implant Placement

This section investigates the impact of the placement of femoral and tibial components of the knee implant on load distribution, ligament balance, and varus/valgus angle. To assess this, we made slight translational (1 mm) and rotational (3 degrees) modifications to the placement of the original components in three distinct directions (see Fig. 5.14).

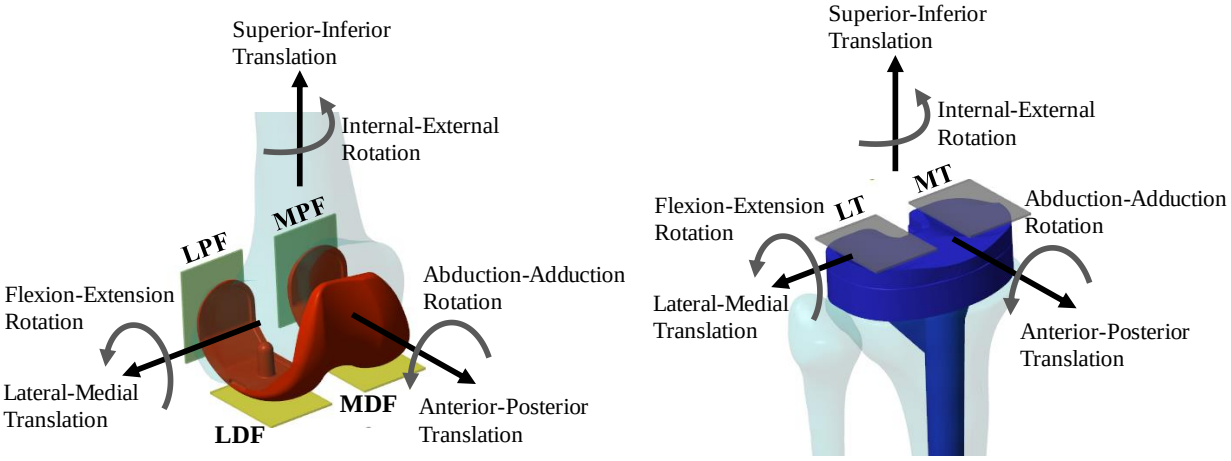

(a) Femoral Component

(b) Tibial Component

Figure 5.14: Variables involved in the placement of femoral and tibial implants. The lateral and medial distal femur planes (LDF and MDF) are tangent to the most distal parts of the femoral implant, and the lateral and medial posterior femur planes (LPF and MPF) are tangent to the most posterior parts of the femoral implant. The lateral and medial tibia planes (LT and MT) are tangent to the lateral and medial tibial plateau.

We then compared the resulting values of $\mathcal{I}_{LD}$, $\mathcal{I}_{LB}$, and α_{VV} with their original values by performing predictive sit-to-stand simulations and utilizing the co-simulation framework introduced in section 5.4.3.

5.7.1 Femoral Component

Figures 5.15 and 5.16 present the effects of altering the translational and rotational placement of the femoral implant, respectively. Upon examining Fig. 5.15, it is apparent that altering the translational placement of the femoral component (FC) has an insignificant effect on the varus/valgus angle. Additionally, no significant changes in the outcomes were observed for medial-lateral translations.

Examining the first column of Fig. 5.15 reveals that the anterior-posterior (A-P) trans-

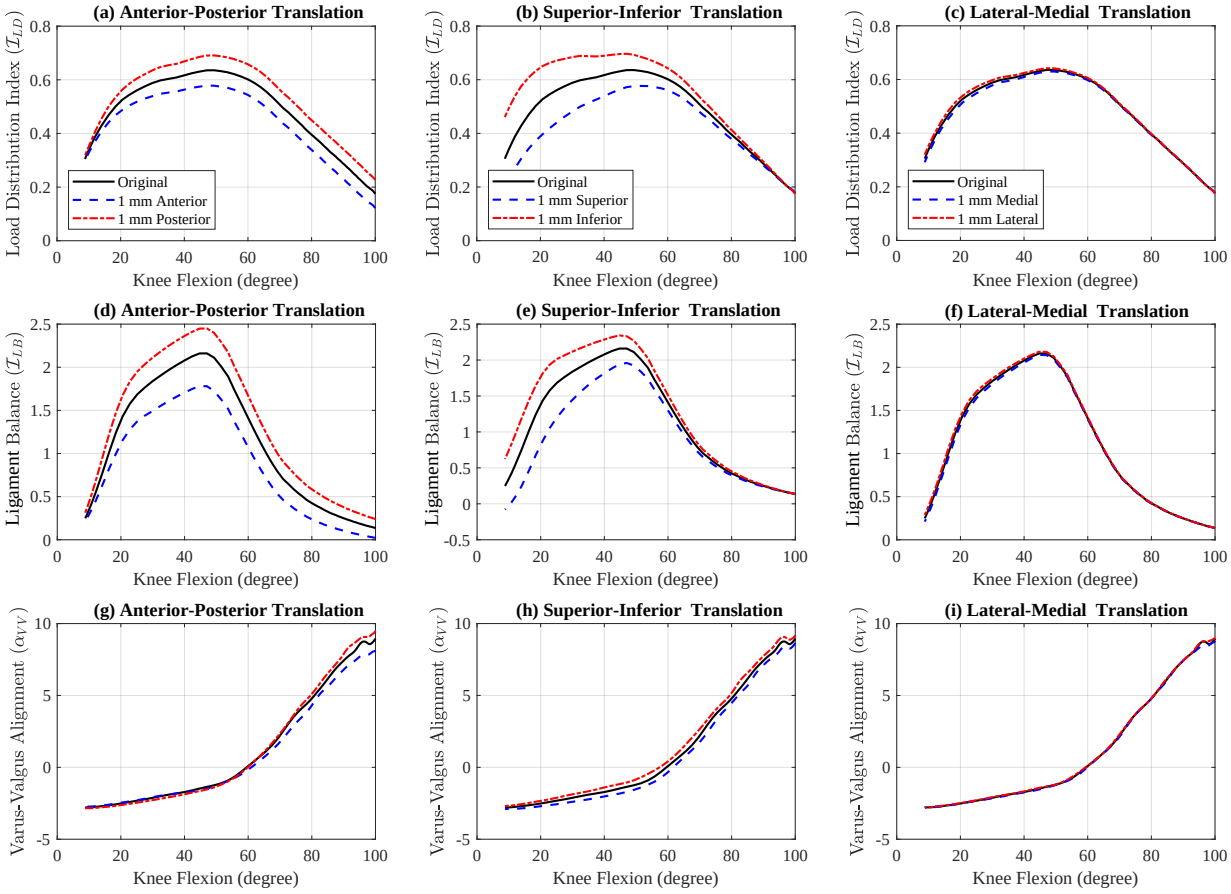

Figure 5.15: Effect of translational displacement of femoral component on the outcome of TKA: $\mathcal{I}_{LD}$ (a, b, and c), $\mathcal{I}_{LB}$ (d, e, and f), and α_{VV} (g, h, and i).

lation of the FC does not produce a significant impact on the outcomes when the knee is completely extended. However, in mid and high knee flexion, anterior translation of the FC decreases the values of $\mathcal{I}_{LD}$ and $\mathcal{I}_{LB}$. The underlying reason for this can be understood by analyzing the effects of A-P translation of the FC on the LDF, MDF, LPF, and MPF planes depicted in Fig. 5.14. A-P translation does not change the LDF and MDF but rather shifts the LPF and MPF in an A-P direction relative to the femur. Thus, when the knee is fully extended, there is no considerable change in the outcomes as the LDF and MDF are in contact with the tibial component. However, as the angle of knee flexion increases,

the impact of the shift on the LPF and MPF planes becomes more evident. The anterior displacement of LPF and MPF reduces the distance between the attachment points of the medial and lateral ligaments, resulting in a decrease in tension for both ligaments. However, due to the medial ligaments being stiffer, the decrease in force on the medial side is greater than that on the lateral side for an equal displacement. This explains why there is a reduction in $\mathcal{I}_{LD}$ and $\mathcal{I}_{LB}$ with the anterior displacement of the FC in mid and high flexions.

The second column of Fig. 5.15 displays the impact of superior-inferior (S-I) translation of the FC. When comparing the first and second columns of Fig. 5.15, we can observe that the effect of S-I translation is opposite to that of A-P translation. Unlike A-P translation, the effect of S-I translation is significant in low knee flexions but becomes insignificant in high knee flexions. This is due to the effects of S-I translation on the LDF, MDF, LPF, and MPF planes (see Fig. 5.14). S-I translation of the FC does not alter the position of the LPF and MPF planes, but it shifts the LDF and MDF equally in the S-I direction. The superior shift of FC relative to the femur reduces the distance between the attachment points of the medial and lateral ligaments in low knee flexions, causing a decrease in tension for both ligaments. However, since the medial ligaments are stiffer than the lateral ligaments, the decrease in laxity is greater for the medial ligaments.

The impact of abduction-adduction (A-A) rotation on load distribution, ligament balance, and varus-valgus alignment in the knee joint is depicted in the first column of Fig. 5.16. As illustrated in Fig. 5.14, abduction rotation shifts the MDF plane upwards and the LDF downwards. This implies that the attachment points of the medial ligaments move closer together while those of the lateral ligaments move further apart for low and mid-flexion angles. Consequently, the medial side becomes looser while the lateral side becomes stiffer, which is evident in Fig. 5.16 (d). However, the effect on ligament laxity in higher knee flexions is insignificant since A-A rotation does not shift the LPF and MPF planes. Moreover, A-A rotation has a considerable influence on the varus-valgus angle. Rotating the FC about the x-axis (abduction) results in increased varus, which means the femur head moves towards the medial side, shifting the load on the knee joint towards the

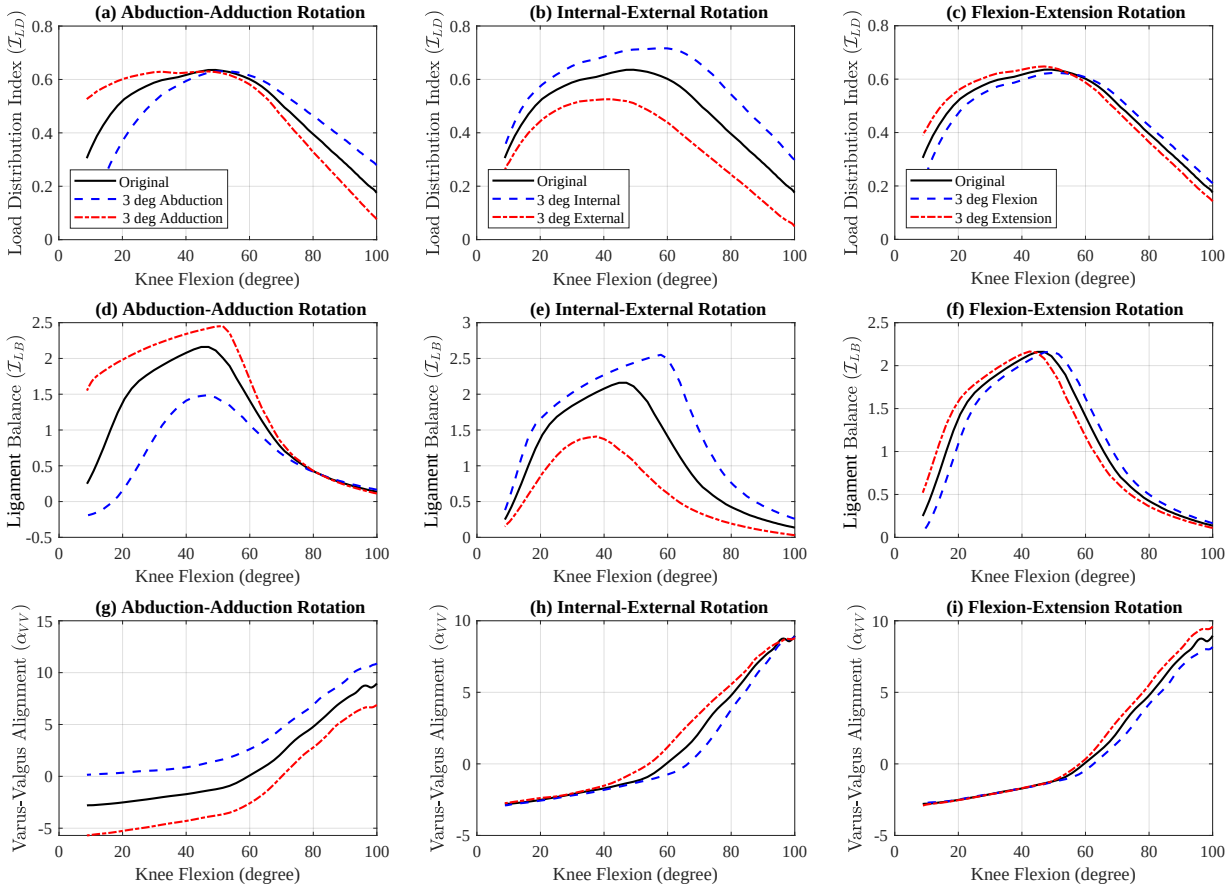

Figure 5.16: Effect of rotational displacement of femoral component on the outcome of TKA.

medial side. The combination of changes in the varus-valgus angle and ligament balance leads to a lower value of $\mathcal{I}_{LD}$ in low knee flexions (due to higher laxity of the medial side and stiffer lateral side) and a higher value of $\mathcal{I}_{LD}$ in high knee flexions because of the medial shift of the load caused by more varus alignment.

According to Fig. 5.14, internal rotation moves the MPF plane towards the back and the LPF in the forward direction (with respect to the femur). This means that, for high knee flexion angles, the attachment points of the medial ligaments move farther apart while those of the lateral ligaments move closer together. This makes the medial side stiffer

and the lateral side looser (higher $\mathcal{I}_{LB}$), as seen in Fig. 5.16 (e). However, the effect on ligament laxity in lower knee flexions is not significant since I-E rotation does not shift the LDF and MDF planes. Additionally, unlike A-A rotation, I-E rotation does not produce a substantial change in the varus-valgus angle. Consequently, for high knee flexion angles, due to the higher laxity of the lateral side and the stiffer medial side, the values of $\mathcal{I}_{LD}$ are higher.

5.7.2 Tibial Component

Figures 5.17 and 5.18 depict the effects of changing the translational and rotational placement of the tibial implant, respectively. From Fig. 5.17, it is evident that varying the tibial component (TC) placement in the A-P and L-M directions has an insignificant effect on the outcomes. Also, similar to the results obtained for the FC, none of the translational displacements of TC have a significant impact on the varus-valgus alignment.

When the TC is translated superiorly, both LT and MT planes (see Fig. 5.14) move upward by an equal amount, resulting in an increased distance between the attachment points of the medial and lateral ligaments throughout the full range of motion of the knee. Consequently, the tension in both medial and lateral ligaments increases. However, due to the medial ligaments' greater stiffness, the additional force on the medial side increases more than the lateral ligaments, resulting in an increase in both $\mathcal{I}_{LD}$ and $\mathcal{I}_{LB}$, as indicated in Fig. 5.17.

The first column of Fig. 5.18 demonstrates the effects of abduction-adduction (A-A) rotation of the TC on load distribution, ligament balance, and varus-valgus alignment in the knee joint. According to Fig. 5.14, abduction rotation shifts the MT plane upwards and the LDF downwards, causing the attachment points of the lateral ligaments to move closer together and those of the medial ligaments to move further apart throughout the full range of motion of the knee joint. This, in turn, causes the lateral side to become looser and the medial side to become stiffer, which is clearly visible in the second row of the first column in Fig. 5.18. Additionally, A-A rotation of the TC significantly affects the

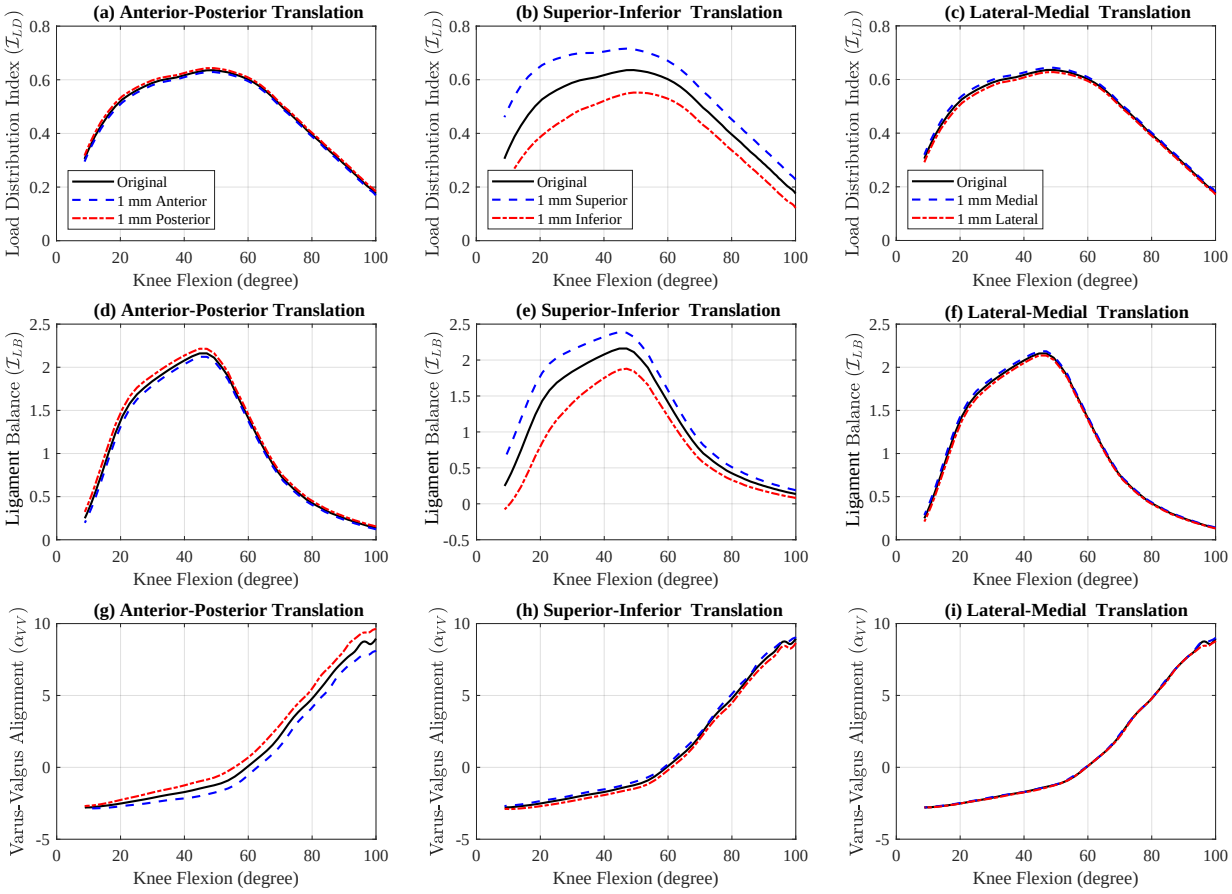

Figure 5.17: Effect of translational displacement of tibial component on the outcome of TKA.

varus-valgus angle during the low and mid-knee flexion of the knee joint. Rotating the TC about the x-axis (abduction) increases valgus, moving the femur head towards the lateral side, and shifting the load on the knee joint to the lateral side. However, the change in the ligament balance overrides the load shift, and we can observe higher medial load after abduction rotation of the TC in Fig. 5.18 (a).

Regarding the I-E rotation of the TC, as shown in the second column of Fig. 5.18, there is no significant change in the ligament balance. However, internal rotation of the TC leads

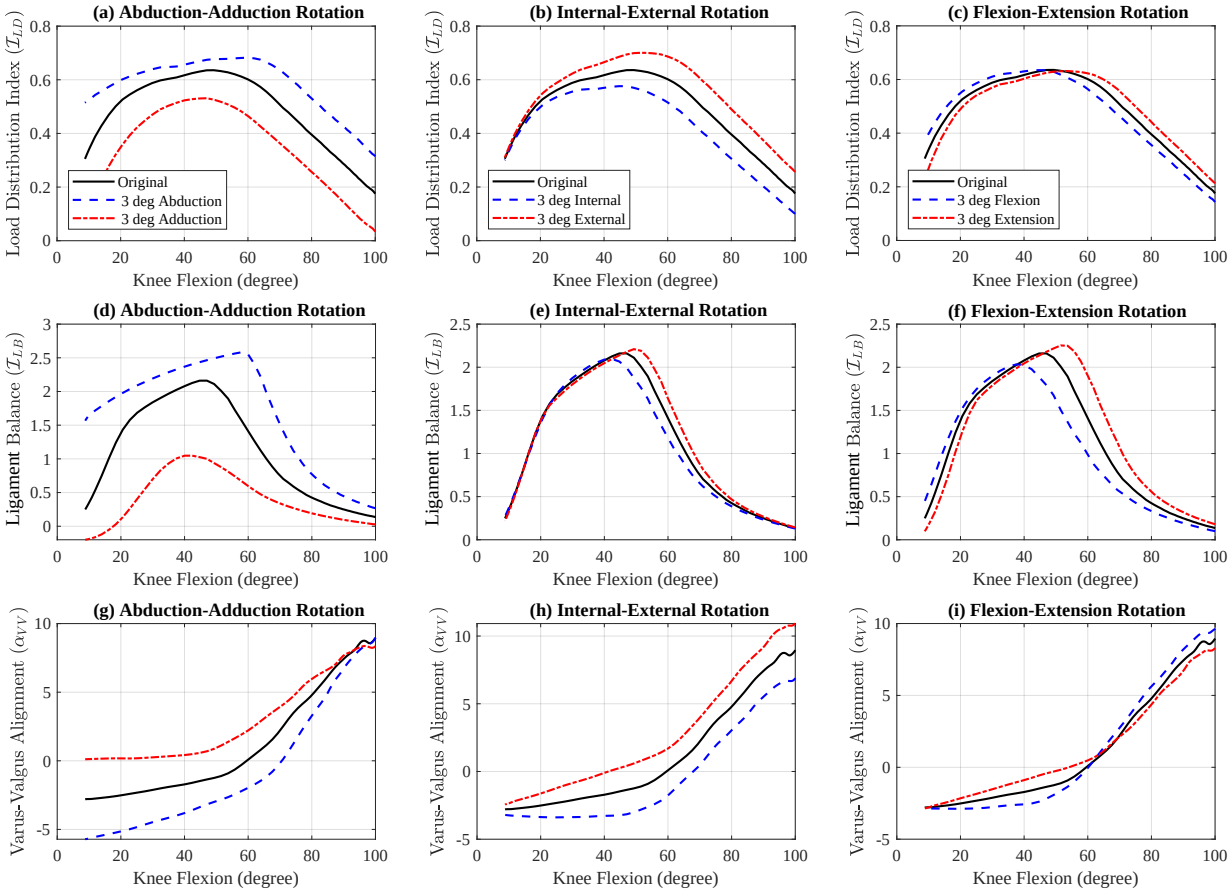

Figure 5.18: Effect of rotational displacement of tibial component on the outcome of TKA.

to an increase in the valgus alignment of the knee at mid and high knee flexions. This leads to a displacement of the femoral head towards the lateral side, causing a corresponding shift in the load distribution of the knee joint towards that side. This shift is evident from the decrease in $\mathcal{I}_{LD}$ for mid and high knee flexions. The sole significant impact of flexion-extension(F-E) rotation of TC is observable in the ligament balance during the knee joint's mid-to-high flexion. An increase in TC rotation in flexion causes greater looseness on the medial side than the lateral side.

Figure 5.19 provides a summary of the impact of modifications in the placement of the

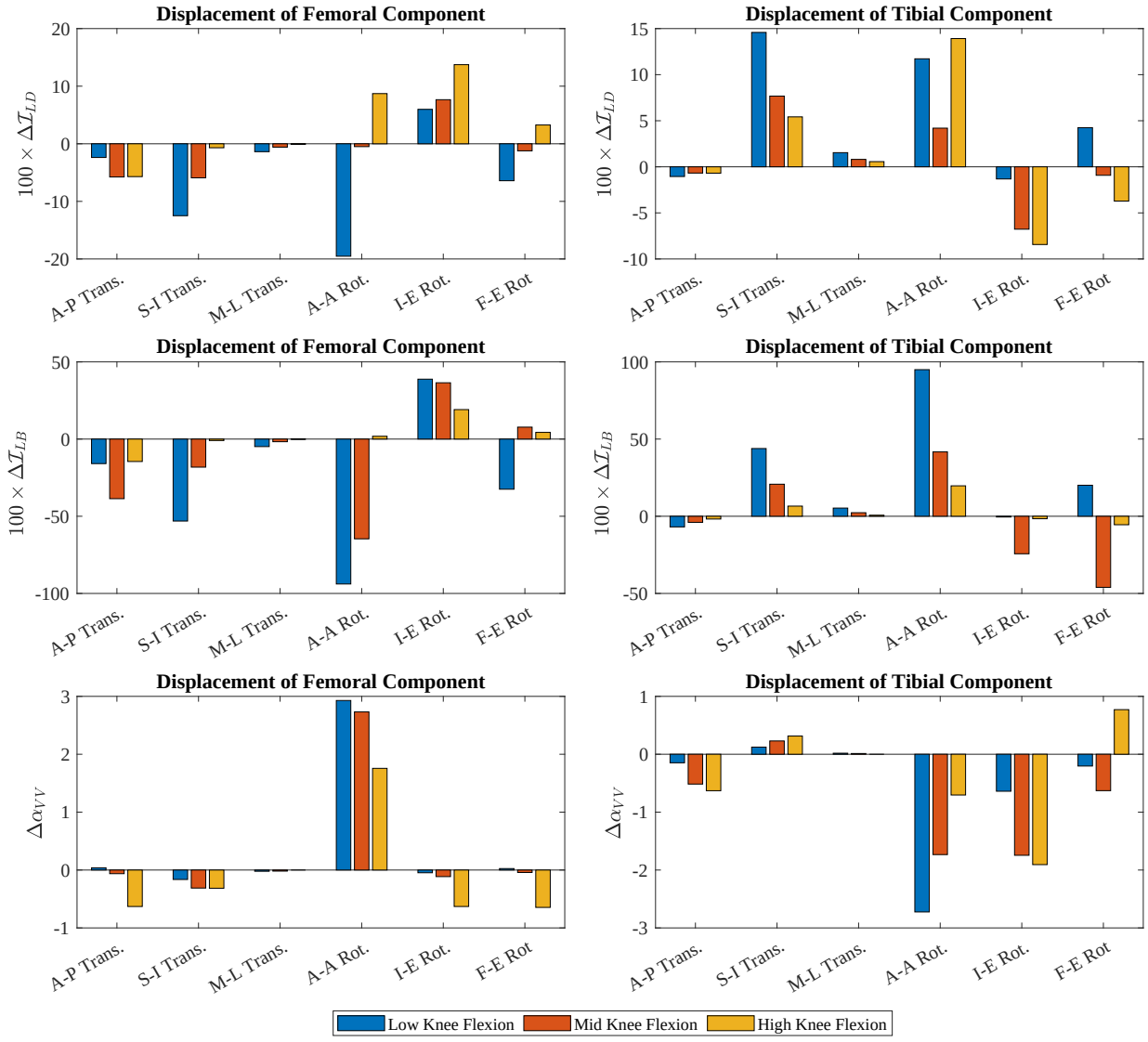

Figure 5.19: The effects resulting from the changes made in the placement of the Femoral and Tibial components (1 mm translational and 3 degree rotational) on $\mathcal{I}_{LD}$, $\mathcal{I}_{LB}$, and α_{VV}. The mid-flexion interval is defined as the range of knee flexion angles from 30 to 60 degrees, while angles below and above this range are respectively classified as low and high knee flexions. The vertical axis shows the average changes in the corresponding interval.

femoral and tibial components. The effects of these changes are presented in three distinct categories based on the degree of knee flexion, namely low, mid, and high.

5.8 Optimal Placement of the Knee Implant

This section describes the method used to optimize the placement of knee implants by considering three key factors explained in Section 5.6, namely load distribution between medial and lateral sides, the balance of medial and lateral ligaments, and varus-valgus alignment. Prior to delving into the details of the method, an evaluation of the current knee implant's performance with regard to these factors is necessary. Figure 5.20 depicts the results obtained from the original placement of the knee implant (see Fig. 5.6), as represented by bold black lines. The figure shows that the original placement of the knee joint has achieved a relatively balanced distribution of medial and lateral loads and ligament laxity at both low and high flexion angles. However, during mid-flexion angles, both $\mathcal{I}_{LD}$ and $\mathcal{I}_{LB}$ exhibit high values, indicating an imbalanced load and laxity of the medial-lateral ligament. It is noteworthy that the literature indicates that the gap balancing technique used in implant placement usually leads to a balanced knee joint in knee extension and high flexion angles but may cause imbalanced ligament laxity during mid-flexion, resulting in mid-flexion instability [234, 235]. This is consistent with the results here.

To identify the optimal location for implant placement, a cost function is defined based on the the disparity between $\mathcal{I}_{LD}$, $\mathcal{I}_{LB}$, and α_{VV} values and their desired values, and then minimizing it through adjustments in FC and TC placement. This can be expressed as the optimization problem shown below, where the cost function is formulated as the integral of the squared differences between each factor's value and its ideal value, with the weighting factors of w_{LD}, w_{LB}, and w_{VV} reflecting their respective levels of importance. Additionally, there is a regularization term aimed at minimizing the modifications to the

initial placement.

$$\underset{\boldsymbol{\mathcal{X}}_{Tibia},\boldsymbol{\mathcal{X}}_{Femur}}{\arg\min} \int_0^{t_f} w_{LD}(\mathcal{I}_{LD}-\mathcal{I}^*_{LD})^2 + w_{LB}(\mathcal{I}_{LB}-\mathcal{I}^*_{LB})^2 + w_{VV}(\alpha_{VV}-\alpha^*_{VV})^2 + \|\boldsymbol{\mathcal{X}}\|^2$$

Subject to:

$$\boldsymbol{\mathcal{X}}_{Min} \leq \boldsymbol{\mathcal{X}} \leq \boldsymbol{\mathcal{X}}_{Max} \tag{5.16}$$

where $\boldsymbol{\mathcal{X}} = [\boldsymbol{\mathcal{X}}_{Femur}; \boldsymbol{\mathcal{X}}_{Tibia}]$ is defined as the concatenation of two matrices: $\boldsymbol{\mathcal{X}}_{Femur}$, representing the modifications made to the femoral component, and $\boldsymbol{\mathcal{X}}_{Tibia}$, representing the modifications made to the tibial component, both in terms of their 6-DoFs (as depicted in Fig. 5.14). These changes collectively describe the displacement of the knee implants from their original positions. In Eq. (5.16), the translational displacements are written in millimeters, and angular displacements are written in degrees.

The results of the knee implant placement optimization and the corresponding effects on $\mathcal{I}_{LD}$, $\mathcal{I}_{LB}$, and α_{VV} for four distinct weighting factor combinations are presented in Table 5.3 and Fig. 5.20.

Optimization #1: The first optimization involves setting the weighting factors for ligament balance and varus-valgus alignment to zero, such that the optimal placement of the implant is determined solely by minimizing the error between the load distribution of the medial and lateral sides and a desired value of equal load distribution, i.e., $\mathcal{I}^*_{LD} = 0$. The optimal solution, as shown in Table 5.3, involves a combination of posterior and superior translation and abduction and external rotation for the femoral component, and inferior translation and adduction and internal rotation for the tibial component. These adjustments are consistent with the effects each individual displacement has on the load distribution, as illustrated in Fig. 5.19.

The findings presented in Fig. 5.20 reveal that the optimal solution effectively distributes loads almost equally between the medial and lateral sides throughout the motion. It is worth mentioning that ligament balance was not considered a cost in this optimization,

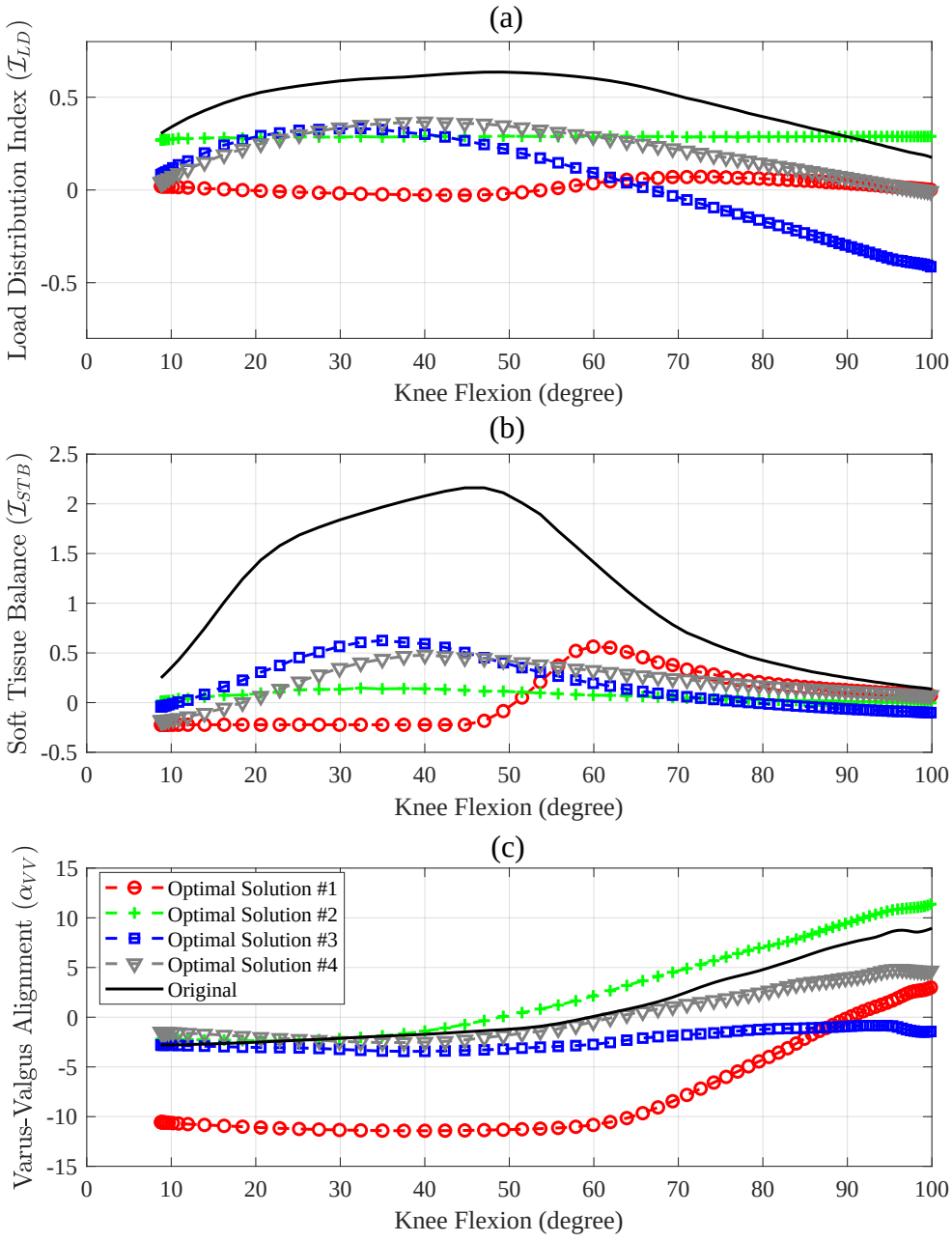

Figure 5.20: The results of the optimal placement of the knee implant.

Table 5.3: Optimal displacement of the knee implant for different weighting values. The displacement was constrained within a limit of ±2 mm for linear displacement and ±3 degrees for angular displacement.

Optimization #	Weights	Component	Displacement	
			Translational (mm) [A/P S-I L-M]	Rotational (deg) [A-A I-E F-E]
1	[4 0 0]	Femoral	[−1.6 1.3 0]	[3 −3 0]
		Tibial	[0 −0.9 0]	[−2.5 2.6 0]
2	[0 4 0]	Femoral	[−1 −0.5 0]	[3 −3 0]
		Tibial	[0 1.4 0]	[−2 0 0]
3	[0 0 1]	Femoral	[0 0 0]	[−2.6 −2.8 0]
		Tibial	[0 0 0]	[−3 3 0]
4	[4 4 1]	Femoral	[−0.4 0 0]	[−1 −3 0]
		Tibial	[0 0 0]	[−3 3 0]

yet the optimal solution demonstrates a more balanced ligament due to its direct impact on load distribution. Moreover, the results indicate a rise in valgus alignment, as expected because increasing valgus leads to a shift in the load from medial to lateral side.

Optimization #2: The second optimization aims to determine the optimal position of the components by solely focusing on achieving a ligament balance index of zero. Table 5.3 shows that the optimal solution requires a combination of posterior and inferior translation, abduction and external rotation for the femoral component, and superior translation and adduction rotation for the tibial component. The results depicted in Fig. 5.20 indicate that the optimal solution effectively achieves a balanced ligament tension. Also, even though

load distribution balance was not considered in the cost function in this optimization, we still observe a more even load distribution compared to the original results, indicating a direct correlation between load distribution and ligament balance.

Optimization #3: The objective of the third optimization is to find the optimal component position that maintains a zero varus-valgus alignment. According to Table 5.3, this can be accomplished by pure rotational displacements from the original implant placement. This involves adduction rotations for both implants, with internal rotation for the femoral component and external rotation for the tibial component. The results presented in Fig. 5.20 demonstrate that the optimal solution successfully achieves excellent mechanical alignment by keeping the varus-valgus angle close to zero. Furthermore, as shown in Fig. 5.20 (a), preventing the knee joint from becoming varus, which is typical for a healthy natural knee [230], causes a significant shift in the load distribution to the lateral side during high knee flexions.

Optimization #4: The fourth optimization integrates the goals of the previous three optimizations by considering all three factors examined in this study, namely load distribution, ligament balance, and varus-valgus alignment, to determine the optimal position of the implant components. As illustrated in Table 5.3, the optimal solution requires a combination of posterior translation and adduction and external rotation for the femoral component, and adduction and internal rotation for the tibial component. The results presented in Fig. 5.20 indicate a well-balanced trade-off between the three factors.

It is important to emphasize that the optimization outcomes presented in this study are purely for demonstration purposes to showcase the ability of this approach to achieve a specific set of desired characteristics, namely ligament balance, load distribution, or varus-valgus alignment. It is worth noting that the optimal knee placement may vary based on the specific preferences and needs of each patient. As the literature is still divided on the ideal outcome for TKA, we do not suggest that an equal medial-lateral load distribution or

ligament laxity is the best alignment. Nevertheless, the optimization method introduced in this study can serve as a useful tool for surgeons to tailor the placement of the knee components according to their preferred attributes.

5.9 Conclusion

This chapter presented a novel approach to finding the optimal placement of knee implants that takes into account three important factors: load distribution, ligament balance, and varus-valgus alignment. The quantitative values obtained by formulating these factors mathematically enable the calculation of their impact on the outcome. Moreover, this is the first study to optimize the placement of knee implants systematically by simultaneously taking into account multiple factors based on user-defined desired values. The study also highlighted the effects of changes to the placement of femoral and tibial components on the outcome. However, it is important to note that this study does not cover all factors that affect the satisfactory outcome of TKA, such as patella tracking, which is a limitation of this work. Overall, this approach can help improve the outcomes of knee arthroplasty and serve as a valuable tool for surgeons in planning and performing this procedure.

Chapter 6

Conclusion

The primary goal of this thesis was to employ predictive computational musculoskeletal simulations to investigate how subject-specific conditions influence the optimal placement of hip and knee implants for total hip arthroplasty (THA) and total knee arthroplasty (TKA). This chapter presents an overview of the thesis's key findings and contributions, along with suggestions for future research that take into account the limitations of this study.

6.1 Summery of Results and Contributions

In Chapter 3, we introduced an inverse dynamics-based method for achieving the optimal alignment of the acetabular cup in THA. This approach utilized motion capture data from a subject and estimated ground reaction forces in double stance postures, eliminating the need for force plate measurements. To quantify the distance from implant impingement and edge-loading, we introduced two indices: Angular Impingement and Edge-loading Distance (AID and AED). We proposed three different optimization criteria to obtain the optimal cup alignment, considering both impingement and edge-loading simultaneously. The results revealed the importance of incorporating various types of movements when

calculating the optimal cup alignment, as relying solely on a specific movement, such as sit-to-stand, may lead to sub-optimal or even risky cup alignment for other movements. Furthermore, we demonstrated the significance of considering both impingement and edge-loading, as focusing solely on impingement may increase the risk of edge-loading, and vice versa. Additionally, we examined the impact of pelvic tilt on the optimal cup alignment and found that a 1° change in pelvic tilt resulted in a 0.72° alteration in the anteversion and a 0.19° shift in the inclination angle for optimal cup orientation. These findings align with previous studies investigating the effect of pelvic tilt on optimal cup alignment.

The objective of Chapter 4 was to address the limitations of the method proposed in Chapter 3, which relied on experimental motion capture data. Instead, we utilized predictive simulations to synthesize sit-to-stand and stooping down movements across various patient conditions, including hip and knee pain as well as lumbar fusion. This approach allowed us to investigate how these conditions impact optimal cup alignment without the need for experimental data. The results obtained from the predictive simulations revealed intriguing connections between the presence of hip and knee joint pain and the risk of hip dislocation, which had not been reported previously. Notably, it was observed that knee pain could modify the sit-to-stand movement in a way that increased the hip's susceptibility to dislocation.

In Chapter 5, we presented two models for knee implants. The initial model was a comprehensive representation with 12 degrees of freedom (DoF), encompassing the volumetric contact model for the femoral and tibial implants, as well as the patellofemoral contact. The second model utilized a Single-DoF Equivalent Kinematic (SEK) approach for the knee joint. To simulate our models, we proposed a co-simulation framework that combined both knee models. We calibrated and validated the knee model using data specific to individual patients. Additionally, we introduced three quantitative measures to assess the optimal positioning of the implants based on three criteria: distribution of load between the medial and lateral sides, balance of ligaments, and alignment of varus/valgus angles. We analyzed the sensitivity of these three measures to changes in implant positioning to gain insights into how different modifications affect the results. The predicted medial and

lateral load on the knee and the secondary kinematics of the knee closely corresponded to the experimental measurements. By making minor adjustments to the positioning and orientation of the tibial and femoral implants, the optimization framework successfully achieved the desired values for load distribution, ligament balance, and varus/valgus angle alignment simultaneously.

6.2 Limitations and Recommendations for Future Research

This section will address the main limitations of the current study. Firstly, the original model developed in Chapter 3 was restricted to a left-right symmetrical model in Chapters 4 and 5. The purpose of this restriction was to reduce computational time of predictive simulations, which was crucial for performing implant optimization algorithms. However, in real-life scenarios, the reaction forces at the left and right hips or knees may not be equal, even during motions that appear symmetrical, such as sit-to-stand. Analysis of the 4th Grand Challenge Competition [13] dataset revealed lower ground reaction forces on the side that underwent THA surgery (refer to Fig. 6.1) during sit-to-stand movements. Various factors, including pain or muscle weakness, can contribute to unsymmetrical reaction forces. One possible approach to overcome this limitation is to employ sub-optimal methods, such as nonlinear model predictive control (NMPC), for predictive simulations. By utilizing relatively short horizons in NMPC models, the optimization process can run faster, allowing for relaxation of the left-right symmetrical assumption [239].

Another limitation of the current study pertains to the optimization framework proposed for hip and knee implant positioning. Although this framework considers multiple factors in optimizing implant positions, rendering it more comprehensive than previous studies in the literature, there are additional factors that should be taken into account when optimizing implant positioning, which were not considered in this study. Regarding the hip joint, this study assessed the risk of dislocation after THA based on two factors:

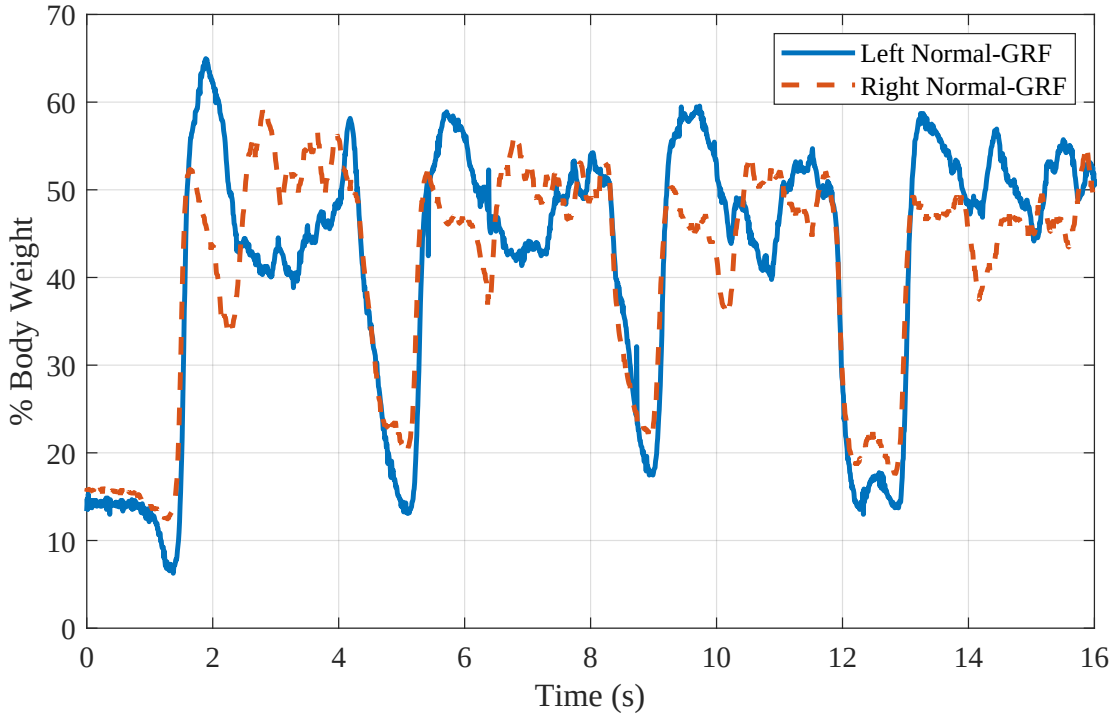

Figure 6.1: The normal ground reaction force (GRF) of the left and right foot, adjusted to the body weight, during a sequence of four consecutive sit-to-stand and stand-to-sit movements [13]. It is noticeable that the maximum GRF values of the left foot are greater than those of the right foot. The subject had undergone a TKA on his right knee.

implant impingement and edge-loading. However, for a more comprehensive optimization, other factors such as bony impingement [100, 206], implant wear [93], and soft tissue management [207] should also be considered. Incorporating bony impingement into the optimization framework requires accurate computer-aided design (CAD) models of the patient's pelvis and femur bones. Once these CAD models are obtained, the bony impingement factor can be included in the presented optimization framework using CAD collision detection algorithms like fast triangle-to-triangle intersection tests [240].

Regarding the knee joint, three factors were utilized in this study to assess optimal implant positioning: medial and lateral load balance, ligament balance, and varus/valgus

alignment, which were identified as important in the literature [226–229]. However, other factors such as proper patella tracking and stability [241], which were not considered in this study, are also important. Including these patella-related factors in the optimization presents challenges, mainly due to the lack of experimental data on patellofemoral contact forces. Additionally, defining patellar maltracking and instability in a mathematical manner suitable for inclusion in an optimization algorithm poses another challenge.

References

[1] F Birrell, O Johnell, and A Silman. Projecting the need for hip replacement over the next three decades: influence of changing demography and threshold for surgery. *Annals of the Rheumatic Diseases*, 58(9):569–572, 1999.

[2] Mayo Foundation for Medical Education and Research. Mayo foundation for medical education and research website, Accessed 27 February 2021, https://www.mayo.edu/, 2020.

[3] Canadian Institute for Health Information. Hip and knee replacements in canada, 2016–2017: Canadian Joint Replacement Registry Annual Report, 2018.

[4] R Biedermann, A Tonin, M Krismer, F Rachbauer, G Eibl, and B Stöckl. Reducing the risk of dislocation after total hip arthroplasty: the effect of orientation of the acetabular component. *The Journal of Bone and Joint Surgery. British volume*, 87(6):762–769, 2005.

[5] J Dargel, J Oppermann, G Brüggemann, and P Eysel. Dislocation following total hip replacement. *Deutsches Ärzteblatt International*, 111(51-52):884, 2014.

[6] G Lewinnek, J Lewis, R Tarr, C Compere, and J Zimmerman. Dislocations after total hip-replacement arthroplasties. *The Journal of Bone and Joint Surgery*, 60(2):217–220, 1978.

[7] M Abdel, P Roth, M Jennings, A Hanssen, and M Pagnano. What safe zone? the vast majority of dislocated thas are within the lewinnek safe zone for acetabular component position. *Clinical Orthopaedics and Related Research®*, 474(2):386–391, 2016.

[8] C Esposito, B Gladnick, Y Lee, S Lyman, T Wright, David J Mayman, and Douglas E Padgett. Cup position alone does not predict risk of dislocation after hip arthroplasty. *The Journal of Arthroplasty*, 30(1):109–113, 2015.

[9] University of Rochester Medical Center Rochester. University of Rochester Medical Center Rochester Website, Accessed 27 February 2021, https://www.urmc.rochester.edu/encyclopedia.aspx, 2021.

[10] R Gunaratne, D Pratt, J Banda, D Fick, R Khan, and B Robertson. Patient dissatisfaction following total knee arthroplasty: a systematic review of the literature. *The Journal of Arthroplasty*, 32(12):3854–3860, 2017.

[11] L Shu, S Li, and N Sugita. Systematic review of computational modelling for biomechanics analysis of total knee replacement. *Biosurface and Biotribology*, 6(1):3–11, 2020.

[12] G Bergmann. Orthoload. Charit - Universittsmedizin Berlin. Accessed 11 November 2021, *See http://www. orthoload. com*, 2008.

[13] B Fregly, T Besier, D Lloyd, S Delp, S Banks, M Pandy, and D D'lima. Grand challenge competition to predict in vivo knee loads. *Journal of Orthopaedic Research*, 30(4):503–513, 2012.

[14] F Groote and A Falisse. Perspective on musculoskeletal modelling and predictive simulations of human movement to assess the neuromechanics of gait. *Proceedings of the Royal Society B*, 288(1946):20202432, 2021.

[15] B Fregly. A conceptual blueprint for making neuromusculoskeletal models clinically useful. *Applied Sciences*, 11(5):2037, 2021.

[16] M Febrer-Nafría, A Nasr, M Ezati, P Brown, J Font-Llagunes, and J McPhee. Predictive multibody dynamic simulation of human neuromusculoskeletal systems: a review. *Multibody System Dynamics*, pages 1–41, 2022.

[17] A Alamdari and V Krovi. A review of computational musculoskeletal analysis of human lower extremities. *Human Modelling for Bio-inspired Robotics*, pages 37–73, 2017.

[18] M Ezati, B Ghannadi, and J McPhee. A review of simulation methods for human movement dynamics with emphasis on gait. *Multibody System Dynamics*, 47:265–292, 2019.

[19] M Sreenivasa, M Millard, I Kingma, J Van Dieen, and K Mombaur. Predicting the influence of hip and lumbar flexibility on lifting motions using optimal control. *Journal of Biomechanics*, 78:118–125, 2018.

[20] R Pàmies-Vilà, J Font-Llagunes, J Cuadrado, and F Alonso. Analysis of different uncertainties in the inverse dynamic analysis of human gait. *Mechanism and Machine Theory*, 58:153–164, 2012.

[21] J Holder, U Trinler, A Meurer, and F Stief. A systematic review of the associations between inverse dynamics and musculoskeletal modeling to investigate joint loading in a clinical environment. *Frontiers in Bioengineering and Biotechnology*, 8:603907, 2020.

[22] T Uchida and S Delp. *Biomechanics of movement: the science of sports, robotics, and rehabilitation*. Mit Press, 2021.

[23] B Prilutsky and V Zatsiorsky. Optimization-based models of muscle coordination. *Exercise and Sport Sciences Reviews*, 30(1):32, 2002.

[24] Y Lai, S Sutjipto, M Carmichael, and G Paul. Preliminary validation of upper limb musculoskeletal model using static optimization. In *2021 43rd Annual International*

Conference of the IEEE Engineering in Medicine & Biology Society (EMBC), pages 4509–4512. IEEE, 2021.

[25] M Morrow, J Rankin, R Neptune, and K Kaufman. A comparison of static and dynamic optimization muscle force predictions during wheelchair propulsion. *Journal of Biomechanics*, 47(14):3459–3465, 2014.

[26] M Shourijeh, N Mehrabi, and J McPhee. Forward static optimization in dynamic simulation of human musculoskeletal systems: a proof-of-concept study. *Journal of Computational and Nonlinear Dynamics*, 12(5), 2017.

[27] A Erdemir, S McLean, W Herzog, and A van den Bogert. Model-based estimation of muscle forces exerted during movements. *Clinical Biomechanics*, 22(2):131–154, 2007.

[28] S Hamner, A Seth, and S Delp. Muscle contributions to propulsion and support during running. *Journal of Biomechanics*, 43(14):2709–2716, 2010.

[29] M Wesseling, F De Groote, and I Jonkers. The effect of perturbing body segment parameters on calculated joint moments and muscle forces during gait. *Journal of Biomechanics*, 47(2):596–601, 2014.

[30] D Thelen, K Choi, and A Schmitz. Co-simulation of neuromuscular dynamics and knee mechanics during human walking. *Journal of Biomechanical Engineering*, 136(2):021033, 2014.

[31] V Norman-Gerum and J McPhee. Constrained dynamic optimization of sit-to-stand motion driven by bézier curves. *Journal of Biomechanical Engineering*, 140(12), 2018.

[32] K Ho Hoang and K Mombaur. Optimal design of a physical assistive device to support sit-to-stand motions. In *2015 IEEE International Conference on Robotics and Automation (ICRA)*, pages 5891–5897. IEEE, 2015.

[33] C Jansen and J McPhee. Predictive dynamic simulation of olympic track cycling standing start using direct collocation optimal control. *Multibody System Dynamics*, 49:53–70, 2020.

[34] C Brown and J McPhee. Predictive forward dynamic simulation of manual wheelchair propulsion on a rolling dynamometer. *Journal of Biomechanical Engineering*, 142(7):071008, 2020.

[35] C Dembia, N Bianco, A Falisse, J Hicks, and S Delp. Opensim moco: Musculoskeletal optimal control. *PLOS Computational Biology*, 16(12):e1008493, 2020.

[36] M Roebroeck, C Doorenbosch, J Harlaar, R Jacobs, and G Lankhorst. Biomechanics and muscular activity during sit-to-stand transfer. *Clinical Biomechanics*, 9(4):235–244, 1994.

[37] M Sadeghi, M Andani, F Bahrami, and M Parnianpour. Trajectory of human movement during sit to stand: a new modeling approach based on movement decomposition and multi-phase cost function. *Experimental Brain Research*, 229:221–234, 2013.

[38] K Mombaur and K Hoang. How to best support sit to stand transfers of geriatric patients: Motion optimization under external forces for the design of physical assistive devices. *Journal of Biomechanics*, 58:131–138, 2017.

[39] P Roberts and G McCollum. Dynamics of the sit-to-stand movement. *Biological cybernetics*, 74(2):147–157, 1996.

[40] O Chuy, Y Hirata, Z Wang, and K Kosuge. Approach in assisting a sit-to-stand movement using robotic walking support system. In *2006 IEEE/RSJ International Conference on Intelligent Robots and Systems*, pages 4343–4348. IEEE, 2006.

[41] S Jatsun, S Savin, A Yatsun, and R Turlapov. Adaptive control system for exoskeleton performing sit-to-stand motion. In *2015 10th International Symposium on Mechatronics and Its Applications (ISMA)*, pages 1–6. IEEE, 2015.

[42] K Strausser and H Kazerooni. The development and testing of a human machine interface for a mobile medical exoskeleton. In *2011 IEEE/RSJ International Conference on Intelligent Robots and Systems*, pages 4911–4916. IEEE, 2011.

[43] R Bohannon, S Barreca, M Shove, C Lambert, L Masters, and Christopher S Sigouin. Documentation of daily sit-to-stands performed by community-dwelling adults. *Physiotherapy Theory and Practice*, 24(6):437–442, 2008.

[44] K Huffman, B Sanford, A Zucker-Levin, J Williams, and W Mihalko. Increased hip abduction in high body mass index subjects during sit-to-stand. *Gait & Posture*, 41(2):640–645, 2015.

[45] M Bobbert, D Kistemaker, M Aurélio-Vaz, and M Ackermann. Searching for strategies to reduce the mechanical demands of the sit-to-stand task with a muscle-actuated optimal control model. *Clinical Biomechanics*, 37:83–90, 2016.

[46] H Hemami and V Jaswa. On a three-link model of the dynamics of standing up and sitting down. *IEEE Transactions on Systems, Man, and Cybernetics*, 8(2):115–120, 1978.

[47] M Millard and K Mombaur. Sit-to-stand models of older adults should include muscle nonlinearities and arms. In *Converging Clinical and Engineering Research on Neurorehabilitation IV: Proceedings of the 5th International Conference on Neurorehabilitation (ICNR2020), October 13–16, 2020*, pages 333–338. Springer, 2022.

[48] M Geravand, P Korondi, C Werner, K Hauer, and A Peer. Human sit-to-stand transfer modeling towards intuitive and biologically-inspired robot assistance. *Autonomous Robots*, 41:575–592, 2017.

[49] J Kuželički, M Žefran, H Burger, and Bajd. Synthesis of standing-up trajectories using dynamic optimization. *Gait & Posture*, 21(1):1–11, 2005.

[50] A Mughal and K Iqbal. 3d bipedal model with holonomic constraints for the decoupled optimal controller design of the biomechanical sit-to-stand maneuver. *Journal of Biomechanical Engineering*, 132(4): 041010, 2010.

[51] B Ozsoy and J Yang. Simulation-based unassisted sit-to-stand motion prediction for healthy young individuals. In *International Design Engineering Technical Conferences and Computers and Information in Engineering Conference*, volume 46391, page V006T10A001. American Society of Mechanical Engineers, 2014.

[52] H Yamasaki, H Kambara, and Y Koike. Dynamic optimization of the sit-to-stand movement. *Journal of Applied Biomechanics*, 27(4):306–313, 2011.

[53] M Ghaffari, R Nickmanesh, Ne Tamannaee, and F Farahmand. The impingement-dislocation risk of total hip replacement: Effects of cup orientation and patient maneuvers. In *2012 Annual International Conference of the IEEE Engineering in Medicine and Biology Society*, pages 6801–6804. IEEE, 2012.

[54] Ö Gündogdu, K Anderson, and M Parnianpour. Simulation of manual materials handling: Biomechanial assessment under different lifting conditions. *Technology and Health Care*, 13(1):57–66, 2005.

[55] C Chang, D Brown, D Bloswick, and S Hsiang. Biomechanical simulation of manual lifting using spacetime optimization. *Journal of Biomechanics*, 34(4):527–532, 2001.

[56] S Zheng, Q Li, and T Liu. Multi-phase optimisation model predicts manual lifting motions with less reliance on experiment-based posture data. *Ergonomics*, pages 1–16, 2022.

[57] J Song, X Qu, and C Chen. Lifting motion simulation using a hybrid approach. *Ergonomics*, 58(9):1557–1570, 2015.

[58] CJ Lin, MM Ayoub, and TM Bernard. Computer motion simulation for sagittal plane lifting activities. *International Journal of Industrial Ergonomics*, 24(2):141–155, 1999.

[59] R Zaman, Y Xiang, J Cruz, and J Yang. Two-dimensional versus three-dimensional symmetric lifting motion prediction models: a case study. *Journal of Computing and Information Science in Engineering*, 21(4), 2021.

[60] R Rakshit, Y Xiang, and J Yang. Dynamic-joint-strength-based two-dimensional symmetric maximum weight-lifting simulation: Model development and validation. *Proceedings of the Institution of Mechanical Engineers, Part H: Journal of Engineering in Medicine*, 234(7):660–673, 2020.

[61] S Zheng, T Li, Q Li, and T Liu. Different phases in manual materials handling have different performance criteria: evidence from multi-objective optimization. *Journal of Biomechanical Engineering*, 144(9):091004, 2022.

[62] Y Xiang, J Arora, S Rahmatalla, T Marler, R Bhatt, and K Abdel-Malek. Human lifting simulation using a multi-objective optimization approach. *Multibody System Dynamics*, 23:431–451, 2010.

[63] J Song, X Qu, and C Chen. Simulation of lifting motions using a novel multi-objective optimization approach. *International Journal of Industrial Ergonomics*, 53:37–47, 2016.

[64] S Hsiang and MM Ayoub. Development of methodology in biomechanical simulation of manual lifting. *International Journal of Industrial Ergonomics*, 13(4):271–288, 1994.

[65] R Zaman, Y Xiang, R Rakshit, and J Yang. Hybrid predictive model for lifting by integrating skeletal motion prediction with an opensim musculoskeletal model. *IEEE Transactions on Biomedical Engineering*, 69(3):1111–1122, 2021.

[66] Y Xiang, J Arora, and K Abdel-Malek. 3d human lifting motion prediction with different performance measures. *International Journal of Humanoid Robotics*, 9(02):1250012, 2012.

[67] R Zaman, J Quarnstrom, Y Xiang, R Rakshit, and J Yang. Hybrid predictive model for assessing spinal loads for 3d asymmetric lifting. In *International Design Engineering Technical Conferences and Computers and Information in Engineering Conference*, volume 86212, page V002T02A022. American Society of Mechanical Engineers, 2022.

[68] Y Xiang, S Tahmid, P Owens, and J Yang. Two-dimensional symmetric box delivery motion prediction and validation: Subtask-based optimization method. *Applied Sciences*, 10(24):8798, 2020.

[69] M Wesseling, L Derikx, F De Groote, W Bartels, C Meyer, N Verdonschot, and I Jonkers. Muscle optimization techniques impact the magnitude of calculated hip joint contact forces. *Journal of Orthopaedic Research*, 33(3):430–438, 2015.

[70] BW Stansfield, AC Nicol, JP Paul, IG Kelly, F Graichen, and G Bergmann. Direct comparison of calculated hip joint contact forces with those measured using instrumented implants. an evaluation of a three-dimensional mathematical model of the lower limb. *Journal of Biomechanics*, 36(7):929–936, 2003.

[71] J Costa, J Peixoto, P Moreira, A Pedro Souto, P Flores, and H Lankarani. Influence of the hip joint modeling approaches on the kinematics of human gait. *Journal of Tribology*, 138(3):031201, 2016.

[72] G Lenaerts, F DeGroote, B Demeulenaere, M Mulier, G Van der Perre, A Spaepen, and I Jonkers. Subject-specific hip geometry affects predicted hip joint contact forces during gait. *Journal of Biomechanics*, 41(6):1243–1252, 2008.

[73] M Wesseling, F Groote, L Bosmans, W Bartels, C Meyer, K Desloovere, and I Jonkers. Subject-specific geometrical detail rather than cost function formulation affects hip loading calculation. *Computer Methods in Biomechanics and Biomedical Engineering*, 19(14):1475–1488, 2016.

[74] R Bohannon, D Bubela, S Magasi, Y Wang, and R Gershon. Sit-to-stand test: performance and determinants across the age-span. *Isokinetics and exercise science*, 18(4):235–240, 2010.

[75] E Sariali, T Stewart, Z Jin, and J Fisher. Effect of cup abduction angle and head lateral microseparation on contact stresses in ceramic-on-ceramic total hip arthroplasty. *Journal of Biomechanics*, 45(2):390–393, 2012.

[76] M Mak, Z Jin, J Fisher, and T D Stewart. Influence of acetabular cup rim design on the contact stress during edge loading in ceramic-on-ceramic hip prostheses. *The Journal of Arthroplasty*, 26(1):131–136, 2011.

[77] Q Meng, J Wang, P Yang, Z Jin, and J Fisher. The lubrication performance of the ceramic-on-ceramic hip implant under starved conditions. *journal of the mechanical behavior of biomedical materials*, 50:70–76, 2015.

[78] M M Mak and Z M Jin. Analysis of contact mechanics in ceramic-on-ceramic hip joint replacements. *Proceedings of the Institution of Mechanical Engineers, Part H: Journal of Engineering in Medicine*, 216(4):231–236, 2002.

[79] J Elkins, M K O'Brien, N J Stroud, D R Pedersen, J J Callaghan, and T D Brown. Hard-on-hard total hip impingement causes extreme contact stress concentrations. *Clinical Orthopaedics and Related Research®*, 469(2):454–463, 2011.

[80] M M Morlock, N Bishop, J Zustin, M Hahn, W Rüther, and M Amling. Modes of implant failure after hip resurfacing: morphological and wear analysis of 267 retrieval specimens. *JBJS*, 90(Supplement_3):89–95, 2008.

[81] J M Elkins, D R Pedersen, J J Callaghan, and T D Brown. Fracture propagation propensity of ceramic liners during impingement-subluxation: a finite element exploration. *The Journal of Arthroplasty*, 27(4):520–526, 2012.

[82] M Al-Hajjar, I J Leslie, J Tipper, S Williams, J Fisher, and L M Jennings. Effect of cup inclination angle during microseparation and rim loading on the wear of biolox® delta ceramic-on-ceramic total hip replacement. *Journal of Biomedical Materials Research Part B: Applied Biomaterials*, 95(2):263–268, 2010.

[83] X Hua, J Li, Z Jin, and J Fisher. The contact mechanics and occurrence of edge loading in modular metal-on-polyethylene total hip replacement during daily activities. *Medical engineering & physics*, 38(6):518–525, 2016.

[84] J Pierrepont, L Yang, J Arulampalam, C Stambouzou, B Miles, and Q Li. The effect of seated pelvic tilt on posterior edge-loading in total hip arthroplasty: A finite element investigation. *Proceedings of the Institution of Mechanical Engineers, Part H: Journal of Engineering in Medicine*, 232(3):241–248, 2018.

[85] J W Pierrepont, C Z Stambouzou, B P Miles, P B O'Connor, L Walter, A Ellis, R Molnar, J V Baré, M Solomon, S McMahon, et al. Patient specific component alignment in total hip arthroplasty. *Reconstructive Review*, 6(4), 2016.

[86] J Hsu, M de La Fuente, and K Radermacher. Multi-dimensional range-of-motion-based safe zone for patient-specific total hip arthroplasty. *CAOS*, 1:175–180, 2017.

[87] A M DiGioia III, M A Hafez, B Jaramaz, T J Levison, and J E Moody. Functional pelvic orientation measured from lateral standing and sitting radiographs. *Clinical Orthopaedics and Related Research®*, 453:272–276, 2006.

[88] V Kanawade, L D Dorr, and Z Wan. Predictability of acetabular component angular change with postural shift from standing to sitting position. *JBJS*, 96(12):978–986, 2014.

[89] S Nishihara, N Sugano, T Nishii, K Ohzono, and H Yoshikawa. Measurements of pelvic flexion angle using three-dimensional computed tomography. *Clinical Orthopaedics and Related Research®*, 411:140–151, 2003.

[90] J W Babisch, F Layher, and L P Amiot. The rationale for tilt-adjusted acetabular cup navigation. *JBJS*, 90(2):357–365, 2008.

[91] B Lembeck, O Mueller, P Reize, and N Wuelker. Pelvic tilt makes acetabular cup navigation inaccurate. *Acta orthopaedica*, 76(4):517–523, 2005.

[92] R L Barrack, C Lavernia, M Ries, R Thornberry, and E Tozakoglou. Virtual reality computer animation of the effect of component position and design on stability after total hip arthroplasty. *Orthopedic Clinics*, 32(4):569–577, 2001.

[93] J M Elkins, J J Callaghan, and T D Brown. The 2014 frank stinchfield award: The landing zonefor wear and stability in total hip arthroplasty is smaller than we thought: a computational analysis. *Clinical Orthopaedics and Related Research®*, 473(2):441–452, 2015.

[94] D E McCollum and W J Gray. Dislocation after total hip arthroplasty. causes and prevention. *Clinical Orthopaedics and Related Research*, (261):159–170, 1990.

[95] A B Pedersen, S P Johnsen, S Overgaard, K S oballe, H T S orensen, and U Lucht. Total hip arthroplasty in denmark: incidence of primary operations and revisions during 1996–2002 and estimated future demands. *Acta Orthopaedica*, 76(2):182–189, 2005.

[96] K H Widmer and B Zurfluh. Compliant positioning of total hip components for optimal range of motion. *Journal of Orthopaedic Research*, 22(4):815–821, 2004.

[97] F Yoshimine. The safe-zones for combined cup and neck anteversions that fulfill the essential range of motion and their optimum combination in total hip replacements. *Journal of Biomechanics*, 39(7):1315–1323, 2006.

[98] S J Mellon, G Grammatopoulos, M S Andersen, H G Pandit, H S Gill, and D W Murray. Optimal acetabular component orientation estimated using edge-loading

and impingement risk in patients with metal-on-metal hip resurfacing arthroplasty. *Journal of Biomechanics*, 48(2):318–323, 2015.

[99] K H Widmer. Containment versus impingement: finding a compromise for cup placement in total hip arthroplasty. *International orthopaedics*, 31(1):29–33, 2007.

[100] O Kessler, S Patil, S Wirth, E Mayr, C W Colwell Jr, and D D D'Lima. Bony impingement affects range of motion after total hip arthroplasty: A subject-specific approach. *Journal of Orthopaedic Research*, 26(4):443–452, 2008.

[101] E Askari, P Flores, D Dabirrahmani, and R Appleyard. Dynamic modeling and analysis of wear in spatial hard-on-hard couple hip replacements using multibody systems methodologies. *Nonlinear Dynamics*, 82:1039–1058, 2015.

[102] K B Smale, M Conconi, N Sancisi, M Krogsgaard, T Alkjaer, V Parenti-Castelli, and D L Benoit. Effect of implementing magnetic resonance imaging for patient-specific opensim models on lower-body kinematics and knee ligament lengths. *Journal of Biomechanics*, 83:9–15, 2019.

[103] G Putame, M Terzini, F Rivera, M Kebbach, R Bader, and C Bignardi. Kinematics and kinetics comparison of ultra-congruent versus medial-pivot designs for total knee arthroplasty by multibody analysis. *Scientific Reports*, 12(1):3052, 2022.

[104] P Flores. Contact mechanics for dynamical systems: a comprehensive review. *Multibody System Dynamics*, pages 1–51, 2022.

[105] J P Halloran, A J Petrella, and P J Rullkoetter. Explicit finite element modeling of total knee replacement mechanics. *Journal of Biomechanics*, 38(2):323–331, 2005.

[106] Y Bei and B J Fregly. Multibody dynamic simulation of knee contact mechanics. *Medical engineering & physics*, 26(9):777–789, 2004.

[107] I Eskinazi and B J Fregly. Surrogate modeling of deformable joint contact using artificial neural networks. *Medical engineering & physics*, 37(9):885–891, 2015.

[108] L Shu, K Yamamoto, R Yoshizaki, J Yao, T Sato, and N Sugita. Multiscale finite element musculoskeletal model for intact knee dynamics. *Computers in Biology and Medicine*, 141:105023, 2022.

[109] A C Godest, M Beaugonin, E Haug, M Taylor, and P J Gregson. Simulation of a knee joint replacement during a gait cycle using explicit finite element analysis. *Journal of Biomechanics*, 35(2):267–275, 2002.

[110] J P Halloran, S K Easley, A J Petrella, and P J Rullkoetter. Comparison of deformable and elastic foundation finite element simulations for predicting knee replacement mechanics. 2005.

[111] A Pérez-González, C Fenollosa-Esteve, J L Sancho-Bru, F T Sánchez-Marín, M Vergara, and P J Rodríguez-Cervantes. A modified elastic foundation contact model for application in 3d models of the prosthetic knee. *Medical Engineering & Physics*, 30(3):387–398, 2008.

[112] Y Gonthier, J McPhee, C Lange, and J C Piedbœuf. A contact modeling method based on volumetric properties. In *International Design Engineering Technical Conferences and Computers and Information in Engineering Conference*, volume 47438, pages 477–486, 2005.

[113] P Brown. Contact modelling for forward dynamics of human motion. Master's thesis, University of Waterloo, 2017.

[114] E M Abdel-Rahman and M S Hefzy. Three-dimensional dynamic behaviour of the human knee joint under impact loading. *Medical engineering & physics*, 20(4):276–290, 1998.

[115] J P Halloran, A Erdemir, and A J Van Den Bogert. Adaptive surrogate modeling for efficient coupling of musculoskeletal control and tissue deformation models. 2009.

[116] Y Lu, P R Pulasani, R Derakhshani, and T M Guess. Application of neural networks for the prediction of cartilage stress in a musculoskeletal system. *Biomedical signal processing and control*, 8(6):475–482, 2013.

[117] Y C Lin, J P Walter, S A Banks, M G Pandy, and B J Fregly. Simultaneous prediction of muscle and contact forces in the knee during gait. *Journal of Biomechanics*, 43(5):945–952, 2010.

[118] I Eskinazi and B J Fregly. A computational framework for simultaneous estimation of muscle and joint contact forces and body motion using optimization and surrogate modeling. *Medical engineering & physics*, 54:56–64, 2018.

[119] T M Guess, A P Stylianou, and M Kia. Concurrent prediction of muscle and tibiofemoral contact forces during treadmill gait. *Journal of Biomechanical Engineering*, 136(2):021032, 2014.

[120] M W Hast and S J Piazza. Dual-joint modeling for estimation of total knee replacement contact forces during locomotion. *Journal of Biomechanical Engineering*, 135(2), 2013.

[121] M Andersen and J Rasmussen. Total knee replacement musculoskeletal model using a novel simulation method for non-conforming joints. In *Proceedings of the International Society of Biomechanics conference*. International Society of Biomechanics, ISB, 2011.

[122] A Ribeiro, J Rasmussen, P Flores, and L F Silva. Modeling of the condyle elements within a biomechanical knee model. *Multibody System Dynamics*, 28:181–197, 2012.

[123] J P Walter, N Korkmaz, B Fregly, and M Pandy. Contribution of tibiofemoral joint contact to net loads at the knee in gait. *Journal of Orthopaedic Research*, 33(7):1054–1060, 2015.

[124] M Machado, P Flores, J Claro, J Ambrósio, M Silva, António Completo, and H Lankarani. Development of a planar multibody model of the human knee joint. *Nonlinear Dynamics*, 60:459–478, 2010.

[125] G Serrancolí, A Kinney, and B Fregly. Influence of musculoskeletal model parameter values on prediction of accurate knee contact forces during walking. *Medical Engineering & Physics*, 85:35–47, 2020.

[126] E Pegg, J Walter, D D'Lima, B Fregly, H Gill, and D Murray. Minimising tibial fracture after unicompartmental knee replacement: A probabilistic finite element study. *Clinical Biomechanics*, 73:46–54, 2020.

[127] G Serrancolí, A Kinney, B Fregly, and J Font-Llagunes. Neuromusculoskeletal model calibration significantly affects predicted knee contact forces for walking. *Journal of Biomechanical Engineering*, 138(8), 2016.

[128] S Pejhan, H Chong, L Tennant, and S Acker. A comparison of knee joint moments during high flexion squatting and kneeling postures in healthy individuals. *Work*, 65(1):79–88, 2020.

[129] S Acker. *High flexion kinematics and kinetics for the improvement of artificial knee joints*. PhD thesis, 2010.

[130] D D'Lima, N Steklov, B Fregly, S Banks, and C Colwell Jr. In vivo contact stresses during activities of daily living after knee arthroplasty. *Journal of Orthopaedic Research*, 26(12):1549–1555, 2008.

[131] H Mizu-Uchi, C Colwell Jr, C Flores-Hernandez, B Fregly, S Matsuda, and D DLima. Patient-specific computer model of dynamic squatting after total knee arthroplasty. *The Journal of Arthroplasty*, 30(5):870–874, 2015.

[132] S Smith, R Cockburn, A Hemmerich, R Li, and U Wyss. Tibiofemoral joint contact forces and knee kinematics during squatting. *Gait & Posture*, 27(3):376–386, 2008.

[133] A Stylianou, T Guess, and M Kia. Multibody muscle driven model of an instrumented prosthetic knee during squat and toe rise motions. *Journal of Biomechanical Engineering*, 135(4), 2013.

[134] M Watanabe, S Kuriyama, S Nakamura, K Nishitani, Y Tanaka, K Sekiguchi, H Ito, and S Matsuda. Abnormal knee kinematics caused by mechanical alignment in symmetric bicruciate-retaining total knee arthroplasty are alleviated by kinematic alignment. *The Knee*, 27(5):1385–1395, 2020.

[135] L Wang and C Wang. Preliminary study of a customised total knee implant with musculoskeletal and dynamic squatting simulation. *Proceedings of the Institution of Mechanical Engineers, Part H: Journal of Engineering in Medicine*, 233(10):1010–1023, 2019.

[136] N Nashi, C Hong, and L Krishna. Residual knee pain and functional outcome following total knee arthroplasty in osteoarthritic patients. *Knee Surgery, Sports Traumatology, Arthroscopy*, 23:1841–1847, 2015.

[137] JM Sikorski. Alignment in total knee replacement. *The Journal of Bone and Joint Surgery. British volume*, 90(9):1121–1127, 2008.

[138] J Thompson, M Hast, J Granger, S Piazza, and R Siston. Biomechanical effects of total knee arthroplasty component malrotation: a computational simulation. *Journal of Orthopaedic Research*, 29(7):969–975, 2011.

[139] B Kayani, S Konan, A Ayuob, E Onochie, T Al-Jabri, and F Haddad. Robotic technology in total knee arthroplasty: a systematic review. *EFORT Open Reviews*, 4(10):611, 2019.

[140] E Hampp, M Chughtai, L Scholl, N Sodhi, M Bhowmik-Stoker, D Jacofsky, and M Mont. Robotic-arm assisted total knee arthroplasty demonstrated greater accuracy and precision to plan compared with manual techniques. *The Journal of Knee Surgery*, 32(03):239–250, 2019.

[141] L Walker, N Clement, K Ghosh, and D Deehan. What is a balanced knee replacement? *EFORT Open Reviews*, 3(12):614, 2018.

[142] J Victor. Optimising position and stability in total knee arthroplasty. *EFORT Open Reviews*, 2(5):215–220, 2017.

[143] P Grave, T Luyckx, K Claeys, T Tampere, J Kellens, J Müller, and P Gunst. Higher satisfaction after total knee arthroplasty using restricted inverse kinematic alignment compared to adjusted mechanical alignment. *Knee Surgery, Sports Traumatology, Arthroscopy*, pages 1–12, 2020.

[144] J Cherian, B Kapadia, S Banerjee, J Jauregui, K Issa, and M Mont. Mechanical, anatomical, and kinematic axis in tka: concepts and practical applications. *Current Reviews in Musculoskeletal Medicine*, 7:89–95, 2014.

[145] J Insall, R Binazzi, M Soudry, and L Mestriner. Total Knee Arthroplasty. *Clinical Orthopaedics and Related Research®*, 192:13–22, 1985.

[146] J Bellemans, W Colyn, H Vandenneucker, and J Victor. The chitranjan ranawat award: is neutral mechanical alignment normal for all patients?: the concept of constitutional varus. *Clinical Orthopaedics and Related Research®*, 470:45–53, 2012.

[147] C Rivière, L Villet, D Jeremic, and P Vendittoli. What you need to know about kinematic alignment for total knee arthroplasty. *Orthopaedics & Traumatology: Surgery & Research*, 107(1):102773, 2021.

[148] J Shatrov, C Batailler, E Sappey-Marinier, S Gunst, E Servien, and S Lustig. Kinematic alignment fails to achieve balancing in 50% of varus knees and resects more bone compared to functional alignment. *Knee Surgery, Sports Traumatology, Arthroscopy*, 30(9):2991–2999, 2022.

[149] G Clark, R Steer, and D Wood. Functional alignment achieves a more balanced total knee arthroplasty than either mechanical alignment or kinematic alignment prior

to soft tissue releases. *Knee Surgery, Sports Traumatology, Arthroscopy*, pages 1–7, 2022.

[150] H Dossett, N Estrada, G Swartz, G LeFevre, and B Kwasman. A randomised controlled trial of kinematically and mechanically aligned total knee replacements: two-year clinical results. *The Bone & Joint Journal*, 96(7):907–913, 2014.

[151] M T Hirschmann, S Hess, H Behrend, F Amsler, V Leclercq, and L B Moser. Phenotyping of hip–knee–ankle angle in young non-osteoarthritic knees provides better understanding of native alignment variability. *Knee Surgery, Sports Traumatology, Arthroscopy*, 27:1378–1384, 2019.

[152] J Ro, D Ro, Y Kang, H Han, and C S Shin. Biomechanical effect of coronal alignment and ligament laxity in total knee arthroplasty: a simulation study. *Frontiers in Bioengineering and Biotechnology*, 10:452, 2022.

[153] S Okamoto, H Mizu-uchi, K Okazaki, S Hamai, H Nakahara, and Y Iwamoto. Effect of tibial posterior slope on knee kinematics, quadriceps force, and patellofemoral contact force after posterior-stabilized total knee arthroplasty. *The Journal of Arthroplasty*, 30(8):1439–1443, 2015.

[154] M Watanabe, S Kuriyama, S Nakamura, Y Tanaka, K Nishitani, M Furu, H Ito, and S Matsuda. Varus femoral and tibial coronal alignments result in different kinematics and kinetics after total knee arthroplasty. *Knee Surgery, Sports Traumatology, Arthroscopy*, 25:3459–3466, 2017.

[155] K Sekiguchi, S Nakamura, S Kuriyama, K Nishitani, H Ito, Y Tanaka, M Watanabe, and S Matsuda. Effect of tibial component alignment on knee kinematics and ligament tension in medial unicompartmental knee arthroplasty. *Bone & Joint Research*, 8(3):126–135, 2019.

[156] B Innocenti, S Pianigiani, G Ramundo, and E Thienpont. Biomechanical effects of different varus and valgus alignments in medial unicompartmental knee arthroplasty. *The Journal of Arthroplasty*, 31(12):2685–2691, 2016.

[157] S Inoue, M Akagi, S Asada, S Mori, H Zaima, and M Hashida. The valgus inclination of the tibial component increases the risk of medial tibial condylar fractures in unicompartmental knee arthroplasty. *The Journal of Arthroplasty*, 31(9):2025–2030, 2016.

[158] S Small, M Berend, R Rogge, D Archer, A Kingman, and M Ritter. Tibial loading after uka: evaluation of tibial slope, resection depth, medial shift and component rotation. *The Journal of Arthroplasty*, 28(9):179–183, 2013.

[159] P Tzanetis, R Fluit, K deSouza, S Robertson, B Koopman, and N Verdonschot. Pre-planning the surgical target for optimal implant positioning in robotic-assisted total knee arthroplasty. *Bioengineering*, 10(5):543, 2023.

[160] L Bartsoen, M GR Faes, R Wirix-Speetjens, D Moens, I Jonkers, and J Sloten. Probabilistic planning for ligament-balanced tkaidentification of critical ligament properties. *Frontiers in Bioengineering and Biotechnology*, 10, 2022.

[161] Mocap. *Carnegie Mellon University Graphics Lab Motion Capture Database. [Online] http://mocap.cs.cmu.edu/.* Accessed 11 November, 2021.

[162] G Yamaguchi. *Dynamic modeling of musculoskeletal motion: a vectorized approach for biomechanical analysis in three dimensions*. Springer Science & Business Media, 2005.

[163] R Fluit, M Andersen, S Kolk, N Verdonschot, and H Koopman. Prediction of ground reaction forces and moments during various activities of daily living. *Journal of Biomechanics*, 47(10):2321–2329, 2014.

[164] S Skals, M Jung, M Damsgaard, and M Andersen. Prediction of ground reaction forces and moments during sports-related movements. *Multibody System Dynamics*, 39(3):175–195, 2017.

[165] A Karatsidis, G Bellusci, H Schepers, M Zee, M Andersen, and P Veltink. Estimation of ground reaction forces and moments during gait using only inertial motion capture. *Sensors*, 17(1):75, 2017.

[166] A Karatsidis, M Jung, H Schepers, G Bellusci, M Zee, P Veltink, and M Andersen. Musculoskeletal model-based inverse dynamic analysis under ambulatory conditions using inertial motion capture. *Medical Engineering & Physics*, 65:68–77, 2019.

[167] D Catelli, M Wesseling, I Jonkers, and M Lamontagne. A musculoskeletal model customized for squatting task. *Computer Methods in Biomechanics and Biomedical Engineering*, 22(1):21–24, 2019.

[168] V Norman-Gerum. Predictive dynamic simulation of healthy sit-to-stand movement. 2019.

[169] G Bergmann, A Bender, J Dymke, G Duda, and P Damm. Standardized loads acting in hip implants. *PloS one*, 11(5):e0155612, 2016.

[170] S Delp, F Anderson, A Arnold, P Loan, A Habib, C John, E Guendelman, and D Thelen. Opensim: open-source software to create and analyze dynamic simulations of movement. *IEEE Transactions on Biomedical Engineering*, 54(11):1940–1950, 2007.

[171] J Buchman-Pearle and S Acker. Estimating soft tissue artifact of the thigh in high knee flexion tasks using optical motion capture: Implications for marker cluster placement. *Journal of Biomechanics*, 127:110659, 2021.

[172] V Camomilla, R Dumas, and A Cappozzo. Human movement analysis: The soft tissue artefact issue. *Journal of Biomechanics*, 62:pp–1, 2017.

[173] G Lamberto, S Martelli, A Cappozzo, and C Mazzà. To what extent is joint and muscle mechanics predicted by musculoskeletal models sensitive to soft tissue artefacts? *Journal of Biomechanics*, 62:68–76, 2017.

[174] J Hsu, M Fuente, and K Radermacher. Calculation of impingement-free combined cup and stem alignments based on the patient-specific pelvic tilt. *Journal of Biomechanics*, 82:193–203, 2019.

[175] D Murray. The definition and measurement of acetabular orientation. *The Journal of Bone and Joint Surgery. British volume*, 75(2):228–232, 1993.

[176] D D'Lima et al. Standard for hip joint coordinate system recommendations from the isb standardization committee. *Jul*, 17:1–8, 2000.

[177] J Lazennec, F Thauront, C Robbins, and A Pour. Acetabular and femoral anteversions in standing position are outside the proposed safe zone after total hip arthroplasty. *The Journal of Arthroplasty*, 32(11):3550–3556, 2017.

[178] J Pierrepont, G Hawdon, BP Miles, B Connor, J Baré, LR Walter, E Marel, M Solomon, S McMahon, and AJ Shimmin. Variation in functional pelvic tilt in patients undergoing total hip arthroplasty. *The Bone & Joint Journal*, 99(2):184–191, 2017.

[179] T Thelen, P Thelen, H Demezon, S Aunoble, and J-C Le Huec. Normative 3d acetabular orientation measurements by the low-dose eos imaging system in 102 asymptomatic subjects in standing position: analyses by side, gender, pelvic incidence and reproducibility. *Orthopaedics & Traumatology: Surgery & Research*, 103(2):209–215, 2017.

[180] Y Desmarais, D Mottet, P Slangen, and P Montesinos. A review of 3d human pose estimation algorithms for markerless motion capture. *Computer Vision and Image Understanding*, page 103275, 2021.

[181] S Corazza, L Muendermann, AM Chaudhari, T Demattio, C Cobelli, and Thomas P Andriacchi. A markerless motion capture system to study musculoskeletal biomechanics: visual hull and simulated annealing approach. *Annals of Biomedical Engineering*, 34(6):1019–1029, 2006.

[182] S Abujaber, A Marmon, F Pozzi, J Rubano, and J Zeni Jr. Sit-to-stand biomechanics before and after total hip arthroplasty. *The Journal of Arthroplasty*, 30(11):2027–2033, 2015.

[183] M Millard, A Emonds, M Harant, and K Mombaur. A reduced muscle model and planar musculoskeletal model fit for the simulation of whole-body movements. *Journal of Biomechanics*, 89:11–20, 2019.

[184] M Jackson. *The mechanics of the table contact phase of gymnastics vaulting*. PhD thesis, Loughborough University, 2010.

[185] D Anderson, M Madigan, and M Nussbaum. Maximum voluntary joint torque as a function of joint angle and angular velocity: model development and application to the lower limb. *Journal of Biomechanics*, 40(14):3105–3113, 2007.

[186] M Millard, T Uchida, A Seth, and S Delp. Flexing computational muscle: modeling and simulation of musculotendon dynamics. *Journal of Biomechanical Engineering*, 135(2), 2013.

[187] C Oomens, O Bressers, E Bosboom, C Bouten, and D Bader. Can loaded interface characteristics influence strain distributions in muscle adjacent to bony prominences? *Computer Methods in Biomechanics and Biomedical Engineering*, 6(3):171–180, 2003.

[188] A Kralj, R J Jaeger, and M Munih. Analysis of standing up and sitting down in humans: definitions and normative data presentation. *Journal of Biomechanics*, 23(11):1123–1138, 1990.

[189] V Norman-Gerum and J McPhee. Comprehensive description of sit-to-stand motions using force and angle data. *Journal of Biomechanics*, 112:110046, 2020.

[190] E Tully, M Reza Fotoohabadi, and M Galea. Sagittal spine and lower limb movement during sit-to-stand in healthy young subjects. *Gait & Posture*, 22(4):338–345, 2005.

[191] M Patterson and A Rao. Gpops-ii: A matlab software for solving multiple-phase optimal control problems using hp-adaptive gaussian quadrature collocation methods and sparse nonlinear programming. *ACM Transactions on Mathematical Software (TOMS)*, 41(1):1–37, 2014.

[192] W Janssen, H Bussmann, and H Stam. Determinants of the sit-to-stand movement: a review. *Physical Therapy*, 82(9):866–879, 2002.

[193] S Kawagoe, N Tajima, and E Chosa. Biomechanical analysis of effects of foot placement with varying chair height on the motion of standing up. *Journal of Orthopaedic Science*, 5(2):124–133, 2000.

[194] M Mohtajeb, J Cibere, M Mony, H Zhang, E Sullivan, Michael A Hunt, and David R Wilson. Open mri assessment of anterior femoroacetabular clearance in active and passive impingement-provoking postures. *Bone & Joint Open*, 2(11):988–996, 2021.

[195] AJ Buckland, V Puvanesarajah, J Vigdorchik, R Schwarzkopf, A Jain, EO Klineberg, R Hart, JJ Callaghan, and H Hassanzadeh. Dislocation of a primary total hip arthroplasty is more common in patients with a lumbar spinal fusion. *The Bone & Joint Journal*, 99(5):585–591, 2017.

[196] A MohammadiNasrabadi, W McNally, G Moammer, and J McPhee. Automatic extraction of spinopelvic parameters using deep learning to detect landmarks as objects. In *Medical Imaging with Deep Learning*, 2022.

[197] M Galli, M Crivellini, F Sibella, A Montesano, P Bertocco, and C Parisio. Sit-to-stand movement analysis in obese subjects. *International Journal of Obesity*, 24(11):1488–1492, 2000.

[198] K Turcot, S Armand, D Fritschy, P Hoffmeyer, and D Suvà. Sit-to-stand alterations in advanced knee osteoarthritis. *Gait & Posture*, 36(1):68–72, 2012.

[199] M Arx, M Liechti, L Connolly, C Bangerter, M Meier, and S Schmid. From stoop to squat: A comprehensive analysis of lumbar loading among different lifting styles. *Frontiers in Bioengineering and Biotechnology*, 9:769117, 2021.

[200] C Esposito, K Carroll, P Sculco, D Padgett, S Jerabek, and D Mayman. Total hip arthroplasty patients with fixed spinopelvic alignment are at higher risk of hip dislocation. *The Journal of Arthroplasty*, 33(5):1449–1454, 2018.

[201] T Youm, S Maurer, and S Stuchin. Postoperative management after total hip and knee arthroplasty. *The Journal of Arthroplasty*, 20(3):322–324, 2005.

[202] G Schmidt, R Sciulli, and G Altman. Knee injury in patients experiencing a high-energy traumatic ipsilateral hip dislocation. *JBJS*, 87(6):1200–1204, 2005.

[203] WJ Gillespie. The incidence and pattern of knee injury associated with dislocation of the hip. *The Journal of Bone and Joint Surgery. British volume*, 57(3):376–378, 1975.

[204] J Tabuenca and J Truan. Knee injuries in traumatic hip dislocation. *Clinical Orthopaedics and Related Research (1976-2007)*, 377:78–83, 2000.

[205] H Ike, L Dorr, N Trasolini, M Stefl, B McKnight, and N Heckmann. Spine-pelvis-hip relationship in the functioning of a total hip replacement. *JBJS*, 100(18):1606–1615, 2018.

[206] W Kurtz, T Ecker, W Reichmann, and S Murphy. Factors affecting bony impingement in hip arthroplasty. *The Journal of Arthroplasty*, 25(4):624–634, 2010.

[207] D Osei, K Rebehn, and M Boyer. Soft-tissue defects after total knee arthroplasty: management and reconstruction. *The Journal of the American Academy of Orthopaedic Surgeons*, 24(11):769, 2016.

[208] R Barrack. Dislocation after total hip arthroplasty: implant design and orientation. *JAAOS-Journal of the American Academy of Orthopaedic Surgeons*, 11(2):89–99, 2003.

[209] D DLima, C Townsend, S Arms, B Morris, and Colwell Jr. An implantable telemetry device to measure intra-articular tibial forces. *Journal of Biomechanics*, 38(2):299–304, 2005.

[210] K Keller and M Engelhardt. Strength and muscle mass loss with aging process. age and strength loss. *Muscles, Ligaments and Tendons Journal*, 3(4):346, 2013.

[211] A Schmitz and D Piovesan. Development of an open-source, discrete element knee model. *IEEE Transactions on Biomedical Engineering*, 63(10):2056–2067, 2016.

[212] T Sugita and A Amis. Anatomic and biomechanical study of the lateral collateral and popliteofibular ligaments. *The American journal of sports medicine*, 29(4):466–472, 2001.

[213] F Liu, B Yue, H Gadikota, M Kozanek, W Liu, T Gill, H Rubash, and G Li. Morphology of the medial collateral ligament of the knee. *Journal of Orthopaedic Surgery and Research*, 5:1–8, 2010.

[214] A Edwards, A Bull, and A Amis. The attachments of the fiber bundles of the posterior cruciate ligament: an anatomic study. *Arthroscopy: The Journal of Arthroscopic & Related Surgery*, 23(3):284–290, 2007.

[215] H Davies, A Unwin, and P Aichroth. The posterolateral corner of the knee: anatomy, biomechanics and management of injuries. *Injury*, 35(1):68–75, 2004.

[216] L Blankevoort, J Kuiper, R Huiskes, and H Grootenboer. Articular contact in a three-dimensional model of the knee. *Journal of Biomechanics*, 24(11):1019–1031, 1991.

[217] D Butler, M Kay, and D Stouffer. Comparison of material properties in fascicle-bone units from human patellar tendon and knee ligaments. *Journal of Biomechanics*, 19(6):425–432, 1986.

[218] Y Gonthier. Contact dynamics modelling for robotic task simulation. 2007.

[219] A Hall, C Schmitke, and J McPhee. Symbolic formulation of a path-following joint for multibody dynamics. In *International Design Engineering Technical Conferences and Computers and Information in Engineering Conference*, volume 46346, page V003T01A025. American Society of Mechanical Engineers, 2014.

[220] B Beynnon, J Yu, D Huston, B Fleming, R Johnson, L Haugh, and M Pope. A sagittal plane model of the knee and cruciate ligaments with application of a sensitivity analysis. 1996.

[221] A Merican, S Sanghavi, F Iranpour, and A Amis. The structural properties of the lateral retinaculum and capsular complex of the knee. *Journal of Biomechanics*, 42(14):2323–2329, 2009.

[222] J Mountney, W Senavongse, A Amis, and NTilde;Thomas. Tensile strength of the medial patellofemoral ligament before and after repair or reconstruction. *The Journal of Bone and Joint Surgery. British volume*, 87(1):36–40, 2005.

[223] S Piazza and S Delp. Three-dimensional dynamic simulation of total knee replacement motion during a step-up task. *J. Biomech. Eng.*, 123(6):599–606, 2001.

[224] S Bersini, V Sansone, and C Frigo. A dynamic multibody model of the physiological knee to predict internal loads during movement in gravitational field. *Computer Methods in Biomechanics and Biomedical Engineering*, 19(5):571–579, 2016.

[225] M Marra, V Vanheule, R Fluit, B Koopman, J Rasmussen, N Verdonschot, and M Andersen. A subject-specific musculoskeletal modeling framework to predict in

vivo mechanics of total knee arthroplasty. *Journal of Biomechanical Engineering*, 137(2):020904, 2015.

[226] N Sheth, A Husain, and C Nelson. Surgical techniques for total knee arthroplasty: measured resection, gap balancing, and hybrid. *JAAOS-Journal of the American Academy of Orthopaedic Surgeons*, 25(7):499–508, 2017.

[227] P Choong, M Dowsey, and J Stoney. Does accurate anatomical alignment result in better function and quality of life? comparing conventional and computer-assisted total knee arthroplasty. *The Journal of Arthroplasty*, 24(4):560–569, 2009.

[228] M Verstraete, P Meere, G Salvadore, J Victor, and P Walker. Contact forces in the tibiofemoral joint from soft tissue tensions: implications to soft tissue balancing in total knee arthroplasty. *Journal of Biomechanics*, 58:195–202, 2017.

[229] S Babazadeh, J Stoney, K Lim, and P Choong. The relevance of ligament balancing in total knee arthroplasty: how important is it? a systematic review of the literature. *Orthopedic Reviews*, 1(2), 2009.

[230] R Hsu, S Himeno, M Coventry, and E Chao. Normal axial alignment of the lower extremity and load-bearing distribution at the knee. *Clinical Orthopaedics and Related Research (1976-2007)*, 255:215–227, 1990.

[231] C Rivière, F Iranpour, E Auvinet, S Howell, P-A Vendittoli, J Cobb, and S Parratte. Alignment options for total knee arthroplasty: a systematic review. *Orthopaedics & Traumatology: Surgery & Research*, 103(7):1047–1056, 2017.

[232] W Mihalko, K Saleh, K Krackow, and L Whiteside. Soft-tissue balancing during total knee arthroplasty in the varus knee. *JAAOS-Journal of the American Academy of Orthopaedic Surgeons*, 17(12):766–774, 2009.

[233] B Daines and D Dennis. Gap balancing vs. measured resection technique in total knee arthroplasty. *Clinics in Orthopedic Surgery*, 6(1):1–8, 2014.

[234] J Martin and L Whiteside. The influence of joint line position on knee stability after condylar knee arthroplasty. *Clinical Orthopaedics and Related Research®*, 259:146–156, 1990.

[235] M Molder, A Wymenga, and P Heesterbeek. Mid-flexion laxity in the asymptomatic native knee is predominantly present on the lateral side. *Knee Surgery, Sports Traumatology, Arthroscopy*, 27:3614–3625, 2019.

[236] A Nowakowski, M Majewski, M Müller-Gerbl, and V Valderrabano. Development of a force-determining tensor to measure physiologic knee ligament gaps without bone resection using a total knee arthroplasty approach. *Journal of Orthopaedic Science*, 16:56–63, 2011.

[237] C Rivière, S Lazic, O Boughton, Y Wiart, L Villet, and J Cobb. Current concepts for aligning knee implants: patient-specific or systematic? *EFORT Open Reviews*, 3(1):1, 2018.

[238] S Howell, M Hull, and M Mahfouz. Kinematic alignment in total knee arthroplasty. *Insall and Scott surgery of the knee. Philadelphia, PA: Elsevier*, pages 1255–1268, 2012.

[239] N Mehrabi, R Sharif Razavian, B Ghannadi, and J McPhee. Predictive simulation of reaching moving targets using nonlinear model predictive control. *Frontiers in Computational Neuroscience*, 10:143, 2017.

[240] B Danaei, N Karbasizadeh, and M Tale Masouleh. A general approach on collision-free workspace determination via triangle-to-triangle intersection test. *Robotics and Computer-Integrated Manufacturing*, 44:230–241, 2017.

[241] M Malo and K Vince. The unstable patella after total knee arthroplasty: etiology, prevention, and management. *JAAOS-Journal of the American Academy of Orthopaedic Surgeons*, 11(5):364–371, 2003.